Title
Thermal Transport in 2D Materials

Permalink
https://escholarship.org/uc/item/9q42022p

Author
Sievers, Charles Andrew

Publication Date
2021

Peer reviewed|Thesis/dissertation

Thermal Transport in 2D Materials

By

CHARLES A. SIEVERS
DISSERTATION

Submitted in partial satisfaction of the requirements for the degree of

DOCTOR OF PHILOSOPHY

in

Chemistry

in the

OFFICE OF GRADUATE STUDIES

of the

UNIVERSITY OF CALIFORNIA

DAVIS

Approved:

_____

Davide Donadio, Chair

_____

Lee-Ping Wang

_____

Niels Grønbech-Jensen

Committee in Charge

2021

To my grandfather Bruce Stewart. I never would have gotten this far without you. It is hard to imagine that over ten years ago you were telling me about the exciting new field of nanomaterials. I wish I could tell you all about the field now.

Contents

List of Figures

From (a) to (f), the time parameter τ in both thermostatting methods increases from 0.05 ps to 2 ps. The thermal baths are $L_{\text{th}} = 40$ nm long in all the simulations here. 33

Spectral conductance of a short graphene sheet with $L = 10$ nm at 20 K from NEMD simulations using the Langevin thermostatting method with a fixed coupling time of $\tau = 0.5$ ps but different bath lengths (from $L_{\text{th}} = 4.9$ nm to 50.2 nm), compared to the fully ballistic conductance obtained from the harmonic AGF calculations. 34

Temperature profiles in the NEMD simulations corresponding to the spectral conductances in Fig. 3.3. From (a) to (f), the time parameter τ in both thermostatting methods increases from 0.05 ps to 2 ps. The thermal baths are $L_{\text{th}} = 40$ nm long in all the simulations here. In the legends, NHC-τ stands for Nosé-Hoover chain and Lan-τ stands for Langevin. 35

The temperature profiles from Fig. 3.5, but with the thermal baths being treated as single points with zero length and the middle part of the system expanded in scale. From (a) to (f), the time parameter τ in both thermostatting methods increases from 0.05 ps to 2 ps. 36

Total thermal conductance (per unit area) as a function of the relaxation time in the thermostating methods, obtained by using Eq. (3.2) or Eq. (3.28). The reference conductance value from AGF is represented as the dashed line. 37

Temperature profile in graphene sheets with two different lengths obtained by using the Langevin or the Nosé-Hoover chain thermostat: (a) $L = 50$ and (b) 2000 nm. 38

(a) Thermal conductance and (b) thermal conductivity of graphene sheets as a function of system length from HNEMD and NEMD simulations. In the NEMD simulations, the conductance is calculated by using either Eq. (3.28) or Eq. (3.2), and the conductivity is calculated by using either Eq. (3.27) or Eq. (3.4). 39

Temperature profiles in graphene sheets with four different lengths ($L = 10, 100, 1000,$ and 10000 nm) obtained by analytically solving a gray 1D BTE. The x axis is the normalized position. The two boundaries are assumed to be at constant temperatures of 305 K and 295 K, respectively. Inset: a schematic illustration of the simulation domain and the thermalizing boundaries. 40

regions, determined after processing the experimental data (figure2) with the FEM. (c) and (d) Thermal conductivity obtained for each region of graphene (1L, 2L and 4L) and for the 1L–2L and 2L–4L junctions for both heat flow directions. (e) and (f) Thermal conductance per unit area, i.e. thickness times width (A = hW), obtained at the junction. The results show no thermal rectification effect within the experimental error bars. 56

Representation of the molecular model of a suspended 1L–2L GJ. Atoms are color-coded according to the temperature at stationary non-equilibrium conditions. The graph shows the temperature profile in the non-equilibrium MD simulation in which the bilayer is heated to 350 K and the monolayer is cooled to 250 K. The two layers are thermally decoupled, with a major temperature difference (ΔT ~34 K) between them; a much smaller temperature jump (ΔT ~5 K) is seen in the bottom layer at the junction. 58

Calculated thermal conductance per unit area of a 1L–2L GJ, either suspended or supported on SiO_2 substrate. (a) Calculated conductance versus length of the bilayer portion at 300 K and 50 K temperature (symbols). Dashed lines are guide to the eye. The stars correspond to the experimental data. (b) Calculated conductance (lines) and experimental data (star symbols) versus temperature, both for suspended and SiO_2-supported GJs. The calculations use the same dimensions as in the experiment (180 nm long bilayer). 62

Combinatorial stacking of atomically-thin layers. (A) Cross-sectional schematic of the sample, comprising Al (80 nm)/2D stack/SiO_2 (90 nm)/Si substrate, where the '2D stack' can be one of nine sequences as shown on the right: G, GG, MG, GGG, GMG, GGMG, GMGG, GMMG, and GMGMG, with n denoting the number of layers. (B) High-resolution transmission electron microscope (HRTEM) and (C) High-angle annular dark-field scanning transmission electron microscope (HAADF-STEM) images of a cross-section of GMMG. 69

Correlative thermal, optical, and spectroscopic imaging. (A) Optical micrograph of sample D1 with stacks up to GMMG. Three regions are labeled, GG, GMG and GMMG. This sample was not annealed. (B) Map of the TBR between Al and SiO_2 (R_{2D}) measured by TDTR microscopy. Inset: MoS_2 PL map showing brighter signal from GMMG compared to GMG due to weak M-M coupling (scale bar 20 m). A close correspondence is observed

Molecular dynamics simulations and the effect of interlayer spacing on thermal transport. (A) NEMD calculations (blue bars) and experimental data (red bars) for various stacks. NEMD calculations are performed after relaxing each of the structures at 300 K, using a free-energy minimization approach that accounts for finite-temperature effects on the interlayer spacing. For GMGMG, the light blue bar denotes additional resistance when the MM layers are AA vs. AB stacked. For both theory and experiment, the plotted resistance includes the top and bottom interfaces with the leads. (B) NEMD-calculated thermal resistance of GMMG (purple curve) and GMGMG (green curve) as a function of cross-plane lattice expansion relative to zero Kelvin. Filled markers correspond to stacks with free-energy minimized lattice spacings at 300 K (purple circle—GMMG, green square—GMGMG with AB stacking between M layers, green diamond—GMGMG with AA stacking between M layers). 76

a) and b) show optical images of the graphene flakes with 1L-2L and 2L-4L junctions respectively. c) and d) show SEM images of the same flakes after fabricating the metal lines at the junction. The arrows point out where the graphene junctions are located. 81

(a) Optical image of the junction. Raman maps of (b) integrated area under the 2D peak, (c) 2D/G area ratio, (d) 2D/G peak intensity ratio, (e) 2D peak position, and (f) G peak position. The dashed line indicates the junction location. 82

(a) Optical image of the junction. Raman maps of (b) integrated area under the 2D peak, (c) 2D/G area ratio, (d) 2D/G peak intensity ratio, (e) 2D peak position, and (f) G peak position. The dashed line indicates the junction location. 83

Fit of our model to the polarized light phase change data versus wavelength of incident light for the SiO2 substrates used in our devices. 84

a) Optical image of the full devices. This image shows the external pads that were used for wire bonding and the silver conductive epoxy drops that con- nects them electrically with the inner pads of the device. b) Optical image zoom in the 1L-2L and 2L-4L devices and a schematic map of the electrical connections of the four-probe electrodes for both the heater and sensor. c) Picture of chip carrier loaded in the arm of the cryostat. The

sample is glued onto the chip carrier using silver paint and a thermocouple is attached to the surface of the chip to measure the temperature at the surface. 84

Thermal measurement set-up. A DC current source is used to apply current to the heater line. The current provided by the source was also measured experimentally using a 1 kΩ resistor and a voltmeter. The voltage between the middle probes of the lines was measured using another voltmeter. The sensor line is connected in series with 1 MΩ and a lock-in voltage of 5 V (~5 A) is used to sense. The voltage from the voltage probes of the sensor line is amplified using a low noise pre-amplifier. The heater and sensor lines can be swapped to account for asymmetric heat flow across graphene junction, i.e. thermal rectification. 85

a) Optical image of the control sample on SiO2 (on Si) with four probe electrodes at each metal line. b) Scanning electron microscopy image of the metal lines. Scale bars were set at 5 m size. 86

a) Schematic drawing of the heater and sensor line on top of the Si/SiO2 control sample. The current, I, and voltage, V, probes are labeled in the image. b) and c) show the resistance, R, and dR/dT versus temperature for the heater (red symbols) and the sensor (blue symbols), respectively. d) and e) shows the temperature variation of the heater, ΔTH, and sensor, ΔTS, when sweeping the heater power for different temperatures, respectively. f) Temper- ature variations per heater power, ΔT/PH, as a function of temperature for the heater and the sensor. 86

a) and b) show the electrical resistance of the heater and sensor lines as a function of temperature for the two different measuring configurations, i.e. before and after being swapped. c) and d) show dR/dT versus temperature for the heater (red symbols) and the sensor (blue symbols) obtained from a) and b), respectively. 87

a) Schematic drawing for the first measuring configuration, where the heat flows from 1L to 2L graphene. b) and c) show the temperature var- iation of the heater, ΔTH, and sensor, ΔTS, when sweeping the heater power for different tempera- tures, respectively. d) Schematic drawing for the second measuring configuration, where the heater and sensor

top layer is thermostated in the bilayer region. Negligible thermal rectification is observed.

94

Transmission functions for different overlap lengths overlaid one another (left). Polarization decomposed transmission function of supported multilayer graphene junction (top right). Polarization decomposed transmission function of suspended multilayer graphene junction (bot- tom right).

95

Transfer function relating the TDTR ratio signal (= $-V_{in}/V_{out}$) at +250 ps to the cross-plane thermal resistance of the 2D stack at the Al/SiO_2 interface, R_{2D}. Blue points are obtained from a solution to the 3D multilayer thermal model, while the red curve is a fit to a 6th order polynomial. The multilayer stack, from top to bottom, is: Al (80 nm)/2D stack/SiO_2 (90 nm)/Si.

96

Maps of raw TDTR signals showing the (A) in-phase voltage V_{in}, (B) out-of-phase voltage V_{out}, (C) ratio = $-V_{in}/V_{out}$, and (D) DC probe reflectivity measured by the photodetector. Signals (A)-(C) are at a probe delay time of +250 ps. Because the sample is coated by an optically-opaque Al transducer layer, the DC probe reflectivity is uniform. Variations in the thermal resistance of the 2D interface between Al and SiO_2 appear largely as variations in the out-of-phase voltage (and thus the ratio). The ratio signal is converted to thermal resistance of the 2D interface using the transfer curve shown in Fig. S1.

97

Sensitivity of the TDTR ratio signal to various parameters. TBC is the thermal boundary conductance = $(thermal boundary resistance)^{-1}$. The sensitivity coefficient for a parameter α is calculated as: $S\alpha = \frac{\partial log(Ratio)}{\partial log(\alpha)}$, where Ratio = $-V_{in}/V_{out}$. Here, we examine the sensitivity to three parameters: (1) TBC at the Al/SiO_2 interface, which is equal to (R_{2D})-1, and is the quantity we are interested in measuring (black markers), (2) TBC at the SiO_2/Si interface (red markers), and (3) Al transducer thickness (blue markers). Two sets of curves are plotted for extreme values of R_{2D}: diamonds for $R_{2D} = 50\ m^2K(GW)^{-1}$, circles for $R_{2D} = 200\ m^2K(GW)^{-1}$.

98

Thermal Transport of 2-D Materials

Abstract

2 Dimensional materials, i.e. van der Waals materials, are an exciting class of materials than can be stacked one on top of another to form new and exciting metamaterials. These sheets and combinations of them have been shown to have extraordinary thermal properties such as the extremely high 3000 $\frac{W}{Km}$ in plane thermal conductivity of Graphene and signficantly low 5 $\frac{MW}{Km^2}$ thermal conductance across MoS_2 and Graphene heterostructures. Accurately calculating the thermal conductance and conductivity of these various structures/materials and understanding how to modulate these thermal properties is not a simple feat. This dissertation is meant to guide future graduate students interested in this field by showing the challenges and potentially fruitful future next steps in the field of thermal transport of 2-D materials.

In Chapter 1, the dissertation is focused on introducing the unique flavor of heat transport in 2-D materials. This involves an brief history of nanoscale heat transport and how the field emerged. This is followed by a motivation for why there has been an increased interest in 2-D thermal transport and a description of two of the most studied vdW materials. Following the description of these layers, this chapter covers some unique characteristics of heat transport on 2-D materials, such as commensurability and different junction types. Finally, the chapter ends with a discussion of different methods used to study these materials and what their strengths/weaknesses are.

In Chapter 2, the dissertation is focused on explaining the methods and surrounding background that are used within the following chapters. This involves explaining background concepts such as interatomic potentials, periodic boundary conditions, statistical ensembles, cell relaxation, and force constants. In addition to background concepts, the methods of NEMD and ESKM and discussed in detail, which are the two major computational methods used within the dissertation.

In Chapter 3, the dissertation is focused on the best practices within the NEMD method for calculating thermal conductance. Moreover, this chapter shows that with a proper choice of thermostat the nonlinear part of the temperature profile should actually not be excluded in thermal transport calculations. It also compares results from NEMD and AGF in the ballistic regime to

probe different transport regimes and show one should directly calculate the thermal conductance from the temperature difference between the heat source and sink. Finally, the chapter explains why the local thermostat in the sink and source should be Langevin instead of Nosé-Hoover.

In Chapter 4, the dissertation is focused on heat transport across graphene step junctions. First the chapter explains the relevance of graphene step junctions. The chapter then discusses experimental and computational results, which show that layers in this devices are thermally decoupled due the lower cross-plane thermal conductance between the layers. The results also show that no significant thermal asymmetry exists across graphene step junctions this size, which is contrary to previous calculations in literature. In addition, the chapter shows that bilayer island defects, common in CVD grown graphene, have little to no contribution to overall thermal transport.

In Chapter 5, the dissertation is focused on thermal transport across graphene-MoS_2 heterojunctions. The chapter starts with a motivation to study heat transfer in heterojunctions. This is followed by experimental results that discuss the varying thermal conductance for different G/MoS_2 stacking compositions. Following the experimental results is a discussion around the computational results, which lead to the conclusion that the cross-plane thermal conductance is sensitive to c-axis lattice expansions that can occur due to thermal expansion. This chapter also contains a discussion on some of the differences seen in the thermal conductance of GMGMG between experiment and theory.

In Chapter 6, the dissertation is focused on wrapping up the results contained within this dissertation.

Acknowledgments

Thank you to my family. My parents never stopped encouraging me to follow my dreams. Their advice and support have been instrumental in my accomplishments.

Thank you to my research lab. Without the support of my lab and our lunch breaks I would have never made it through the program. Special thanks to Prof. Donadio, Dr. Bononi, Dr. Barbalinardo, Dr. Dettori, Zekun, and Dr. Chen.

Thank you to my friends for keeping me sane with beers and board games. Special thanks to Jorgen for planning epic trips that were affordable on a grad school budget.

Thank you to my teachers for all their passion in their subjects and inspiring me to always learn more.

Thank you to Prof. Grønbech-Jensen for helping me to get the experience to work at Sandia. Thank you to Dr. Thompson and Dr. Wood for helping me with my work at Sandia and giving me to opportunity to become great at making scientific software.

Thank you to Brad Wolf there is no way I would be graduating if it were not for you.

Thank you Prof. Donadio, Prof. Grønbech-Jensen, and Prof. Wang for reviewing my dissertation and for all your help along the way.

CHAPTER 1

Introduction

1.1. History

Heat transport forms one of the most important fields of physics as it influences the nature of every substance in the universe. Fourier, starting the field, formulated that the current density $Q(x,t)$ in a solid is proportional to the local temperature gradient, i.e., $Q = -\mathscr{K}\nabla T$, where $\mathscr{K}$ is the thermal conductivity of the material. [1] Fourier's empirical law has been used successfully over the past 200 years to calculate the thermal conductivity of conventional bulk crystals, i.e. copper and aluminum. Understanding the thermal conductivity of materials has been a key factor in engineering electronic devices, cooking ware, home insulation, and numerous other advances since Fourier first wrote his book in 1822. However, within the last 20 years low dimensional materials have led scientists to question whether Fourier's law encompasses the entire field of heat transport. Both numerical and analytical studies suggest that Fourier's law is not valid for low dimensional systems. [2, 3] This is because when relevant material sizes reach the same order of size as the mean free path of heat carriers (from tens of nanometers to tens of microns), the thermal conductivity is no longer independent of the materials length. Recently, as modern technology has pushed to reduce the size scale of transistors and electronic circuits, the length of these devices have reached these critical sizes, thus increasing the importance of understanding and engineering thermal transport of low dimensional materials. [4]

Arguably one of the most important research areas of low dimensional materials, which has grown tremendously in popularity, is 2-D materials. This is mainly due to graphenes incredible transport properties. The field of 2-D materials has seen incredible breakthroughs in heat dissipation of nanoelectronic devices and in thermal conversion to electronic power causing it to be a key target of scientific research. Plus, an increased understanding of 2-D heat transfer will not only help in the management of electronic devices, but optical and optoelectronic devices as well.

Controlling thermal transport of 2-D materials is a major engineering challenge and needs to be tackled to design efficient nanoscale devices. In this review I will discuss some of the significant applications and challenges of engineering thermal transport in 2-D materials.

1.2. 2D Materials

Low-dimensional van der Waals materials, e.g. multilayer graphene and transition metal dichalcogenides, offer a very promising platform to develop new electronic, optoelectronic and energy storage devices. They also present intriguing opportunities to reversibly tune their phonon band structures and thermal conductivity via mechanical deformation or chemical changes. [**5**,**6**,**7**]

1.2.1. Graphene. Grapehene has dominated the discussion on 2-D Material since it was exfoliated for the first time by Novoselov et al, using Scotch Tape. [**8**]. Among its many interesting transport properties, graphene has an incredibly high thermal conductivity of $2\tilde{0}00Wm^{-1}K^{-1}$, [**9**] which is ideal for thermal dissipation problems currently being experienced by the micro/nanoelectronics community. In fact, graphene has already started fulfilling its purpose as a thermal dissipator in the electronic industry, both as a thermal interface material (TIM) and as pillared graphene composites to rival Aluminum and Copper, the current industry standard. [**10**] Further advances in heat dissipation from graphene devices and interconnects is primarily limited by their environment since out-of-plane acoustic modes are among the most significant contributors to graphene's incredible thermal conductivity and the addition of a substrate or additional layers subdues these ZA phonons, thus lowering the thermal dissipation power of a graphene sheet. [**11**,**12**] Along with significant decreases from in-plane thermal conductivity, heat transfer is limited into and out of graphene by weak vdW interactions, thus limiting graphene's dissipative power if it is being used as a heat sink. To overcome these obstacles, further understanding of phonon transport across vdW interfaces is required.

1.2.2. Transition Metal Dichalcogenides. Transitional Metal Dichalcogenides (TMDs) are a class of 2-D semiconductors of the type MX_2, where M is a transition metal element (such as Mo or W) and X is a chalcogen element (such as S, Se, or Te). Due to their electronic bandgap TMDs have potential to be used as extremely compact transistors, which has shifted some of the 2-D material attention off of Graphene. [**13**,**14**] With the addition of low dimensional materials

2

within novel transistors, the problem of thermal bottlenecks escalates from a problem solely focused on phonon transport to also incorporating electron-phonon coupling. [4, 15] This requires a fundamental understanding of which phonons electrons scatter into and the relaxation times of these now populated phonons into modes that may contribute more significantly to thermal transport. Unfortunately, TMD thermal properties have been less studied, when compared to graphene; however, they have also been attracting growing interest. [13, 14, 16, 17, 18, 19]

In addition to their tunable bandgap, TMDs have exceptionally low cross-plane thermal conductivity, whch has led them to be studied as possible thermoelectric materials. [16] Some recent advances have shown that with intercalation one can even modify the cross-plane thermal conductivity. [18] Significant research has been done to calculate cross-plane thermal conductivity for few to many layer MoS_2 homostructures with the aim to study and understand the effects that different numbers of layers have on the thermal conductivity, which is promising for obtaining higher thermoelectric efficiency in thermoelectric materials. [17]

1.2.3. Conductivity vs Conductance. Reporting some intrinsic properties, such as cross-plane thermal conductivity, can be misleading or erroneous when discussing vdW layers attached to a substrate or embedded in a medium as the interfacial thermal resistance between vdW-substrate junctions are extrinsic effects. One must either substract out these interfacial resistances to correctly calculate the thermal conductivity or report the conductance of the device as a whole. In this work, vdW layers are often sandwiched between substrates and/or metallic leads, thus obscuring the intrinisc properties of the layers, such as conductivity. As a consequence a considerable number of results are reported as conductance or as its reciprocal, resistance.

1.2.4. Nano-Phononic devices. Nanophononics is the research field targeting the investigation, control and application of vibrations in nanoscale materials. Phonons, the heat carrying corollary to electrons, can be exploited in the same manners as any quantum particle. Just as we have electronic circuitry devices, one can devise the phononic counterpart. A practical example is a Schroeder diffuser, which acts as an acoustic circuit to impede a select frequency. [20]

Over the past three decades the propagation of sound waves with frequencies in the range from kilohertz to megahertz has been efficiently controlled by phononic devices, but only recently has

there been a push to achieve gigahertz and terahertz phononic devices. [21] Since frequencies are influenced by defects or patterns on the order of their mean free path, one typically can expect to control this frequency range by engineering nanoscale devices.

Nanoscale phononic devices have attracted significant attention as possiblity to engineer complex thermal circuitry devices. [22, 23] Thermal diodes, the essential building block of thermal circuitry, have been shown mathematically in low dimensional linear lattice models to be possible. [24, 25] Since then, significant efforts have been spent identifying efficient thermal rectifiers. [26, 27, 28] Through these efforts it has been shown that a material that consisted of two leads with different substrate interactions connected by a ballistic channel would make a promising thermal diode. [27] An ideal material candidate for this setup is a 2-D material due to its ability to tune its high in-plane conductance with substrates. Recent rigorous simulations have even shown that thermal rectification using 2-D materials is possible, however, rectification must be increased by over an order of magnitude to produce a commercially viable thermal diode. [29]

1.2.5. Homojunctions. In this work, a homojunction is defined as an interface that occurs between two vdW layers of the same type, such as graphene-graphene or $MoS_2 - MoS_2$. Homojunctions form some of the most simplistic nanophononic designs. In addition to forming nanophononic devices, these types of interfaces impact many vdW materials, as bilayer islands commonly form as crystal imperfections during CVD growth of single layer vdW materials. Whether one studies these interfaces to design phononic devices or to reduce the effects of crystal imperfections, these junctions are fundamental to the field of 2-D thermal transport. Research into heat transfer between homojunctions has been extensively explored over the last 10 years, however, as new 2-D materials emerge the need to understand the junctions of these new players also emerges.

1.2.6. Heterojunctions. A heterojunction is an interface that occurs between two separate materials, one such example is graphene-MoS_2. Unlike homojunctions, heterojunction interfaces have been far less studied and understanding phonon scattering at these types of interfaces could lead to the engineering of future 2D metamaterials to alter optical phonon mode relaxation times into acoustic phonons. Since acoustic phonons are typically more efficient heat carriers than optical

phonons, tuning key phonon relaxation times would allow one to either improve heat dissipation in nanoelectronics or decrease thermal conductivity for improved thermal conversion.

To design a new class of vdW thermal metamaterials, as well as understand factors governing heat transport in 2D heterostructures, the following key questions need to be addressed: What are the primary factors governing thermal transport at vdW junctions, in particular, what are the roles of vibrational mismatch and interlayer separation? How does heat flow across a heterojunction compare to that across a homojunction? Finally, can we create 3D solids with tailored thermal conductivity by stacking 2D materials with matched or mismatched vibrational modes, for a variety of applications?

1.2.7. Commensurability. When creating new stacking patterns, different layer types will be stacked one on top of the other with each layer having its own unique in-plane lattice. In certain cases these lattices may be of the same geometry, such as the hexagonal lattices of graphene and MoS2, however, even though this is relatively convenient compared to two layers of differing geometries, the individual lattice constants must be commensurate with one another. This typically grows the size of primitive cells drastically w.r.t. the original primitive cells of the original layers. This process becomes even more cumbersome when additional layers are added on or if layers of different geometries are added together. As primitive cell sizes increase, the computational cost of most computational thermal transport methods can become impractical, which is the case for quantum calculations involving third order corrections. This presents a serious challenge as third order phonon contributions to the thermal conductivity become increasing relevant as the number of layers increases. [17]

1.2.8. Thermal Twistronics. Thermal twistronics are phononic devices, where the engineering of phononic properties arise from the twisting of individual or multiple vdW layers with respect to adjacent layers. Twisted vdW layers have attracted considerable attention since the discovery of magic angles where bilayer graphene sheets become superconducting. [30] Even before magic twist angles, thermal twistronics have been studied to engineer phononic properties. [31] More recently, it has been shown that the thermal conductivity of homogeneous twisted stacks of graphite

is found to strongly depend on the twist angle; where the underlying mechanism relies on the angle dependence of phonon–phonon couplings across the twisted interface. [**32**]

Upon changing the angle between two vdW layers these devices form unique Moiré patterns, thus changing the geometry or in-plane lattice. As discussed in 1.2.7, a change of the in-plane lattice typically results in an increase in the size of the primitive cell, which in part presents the same computational cost challenges. Typically, this results in only being able to model specific angles that produce primitive cells that are feasible to model. Additionally, one must expend additional computational resources to relax both the in-plane and out-of-plane structure to minimize the strain imposed by twists. [**33**] A lofty goal would be to devise a modeling scheme in which one could model any arbitrary angle and then scan for magical angles that produce interesting material properties. Recently, a method of unfolding the Brillouin Zone to explore various twists has been realized. [**34**] In the mean time, it is still imperative to obtain a fundamental understanding of phonon transport at various twists to further the research of magical angles as they could revolutionize the engineering of phononic devices.

1.3. Thermal Conductivity/Conductance Methods

This section covers a number of computational methods currently used to calculate thermal conductance/conductivity of insulators and semiconductors at the nanoscale being used today. These methods are 1) Boltzmann eransport equation (BTE) developed by Peierls [**35**], 2) atomistic Green's function (AGF) and its equivalents, and 3) molecular dynamics (MD).

1.3.1. Boltzmann Transport Equation. The phonon Boltzmann transport equation, combined with Fourier's law is customarily used to describe phonon transport in the diffusive regime [6]. With advances in high performance computing and development of theoretical techniques such as density functional theory [**36**, **37**], full solution of the BTE with realistic interaction potentials is possible. In addition, quantum-statistical effects are easily treated in BTE, thus encompassing the treatment of heat transport in materials below the Debye temperature. In recent years, several advances have been made to solving the BTE making it the gold standard for calculating thermal conductivity of insulators and semiconductors. [**38**, **39**, **40**, **41**, **42**, **43**, **44**]

6

Unfortunately, the quasi-particle picture of heat-carriers breaks down when trying to model structures that contain defects or interfaces on the order of or shorter than the phonon mean free path, such as a glass or a finite size system, rendering BTE no longer applicable. Recent progress has allowed the BTE to overcome some of these hurdles, such as modeling amorphous/partially disordered systems or finite size systems. [44] Despite this progress, BTE still falls short for systems that cannot be modeled by supercells, such as cross-plane conductance across a few layers of 2-D materials or in-plane conductance of a triangular graphene sheet. For heterostructures like the ones previously listed one must look past BTE and rely on molecular dynamics or atomistic greens function equivalents to calculate thermal conductance. Additionally, as one increases layer variety in 2D heterostructures primitive cells must expand in-plane to account for commensurability between unique layers, which increases the computational cost of calculating the thermal conductivity of a primitive cell. This increase in cost can cause ab initio IFC calculations to become infeasible and emperical IFC calculations to become prohibitive.

1.3.2. Atomistic Green's Function Equivalents. Following the early work by Mingo and Yang [45], the atomistic Green's function (AGF) method has become a standard tool to study ballistic phonon transport in the harmonic approximation. In this method, one can calculate the phonon transmission $\mathcal{T}(\omega)$ between two leads as a function of the phonon frequency ω. The ballistic conductance can be calculated through the Landauer expression: [46, 47]

$$(1.1) \qquad G = \frac{1}{2\pi} \int_0^{\omega_{max}} d\omega \hbar\omega \mathcal{T}(\omega) \frac{\partial f_{BE}(\omega, T)}{\partial T}$$

The Landauer equations dependence on a phonon distribution function allows one to seamlessly integrate quantum populations into this method, which lends to its success in accurately calculating ballistic phonon conductance even for materials below their Deby temperature. However, this method fails when attempting to apply it past the ballistic regime, thus rendering it inadequate for heterostructures in the quasi-ballistic to diffusive regime.

1.3.3. MD. Molecular dynamics (MD) is the most versatile and complete classical method to study heat transport at the nanoscale as it incidentally accounts for higher order phonon inter- actions. [48, 49, 50] Quantum mechanical density functional based equilibrium MD [51, 52, 53],

nonequilibrium MD [54] and approach-to-equilibrium MD [55, 56] are a few of the different MD-based methods used for heat transport studies. The methods based on MD are restricted to the classical limit, i.e., the limit of high temperatures. In standard MD, nuclear degrees of freedom are treated classically and quantum effects such as zero-point vibrations are not accounted for. [57] There have been attempts to avoid this short coming, such as quantum heat baths in NEMD calculations. Unfortunately, these calculations lead to poor agreement with experimental values due to erroneously short phonon mean free paths. [57]

1.3.4. Future Directions. Given the extensive work already done on 2-D van der Waals devices and their diverse applications it is easy to see why this field has such potential to revolutionize thermoelectric devices, thermal dissipation in nanoelectronics, and nanophononics. To realize such goals there is still a considerable amount of research that needs to be undertaken. This research includes but is not limited to: Lowering computational cost of QM-MD to viably handle thermal transport below the Debye temperature of materials. Expanding AGF methods past the harmonic approximation to account for phonon-phonon scattering events. Creating new advances like those shown in Isaev et. al. [44] to further BTE as a one-stop-shop for calculating thermal properties in all thermal transport regimes. Continue to research phonon transport at homojunctions of emerging vdW materials. Explore the mixing and twisting of vdW materials to form an exhaustive set of heterostructure and calculate their in-plane and out-of-plane thermal conductivity. With even a few of these avenues we may see exciting technological advances.

CHAPTER 2

Background

2.1. MD

Molecular dynamics (MD) is a computer simulation technique, in which classical Newton's equations of the motion of N particles interacting via a given potential are integrated by using numerical algorithms. Molecular dynamics may be used to simulate the microscopic properties of gases, solids and liquids: for ergodic systems one can show that the statistical ensemble averages are equal to the time averages. [58] Fig. 2.1 summarizes the basic steps of a molecular dynamics simulation.

To start a simulation, one needs to set up the initial positions and velocities of all particles in the system. The positions of particles may be chosen according to the experimental data. The initial velocities may be chosen e.g. according to a Gaussian distribution, and then scaled to the desired temperature : $< v_\alpha^2 > = \frac{k_B T}{m}$, here $< v_\alpha >$ is the α component of the velocity of a given particle, k_B is the Boltzmann constant, T is temperature, and m is the mass of the particles. In addition, the scaled values of velocities must be chosen in such a way as to guarantee that the total momentum of the system is conserved. The acceleration (a_i) of particle i is calculated from the total force (F_i) on the particle i by Newton's law : $F_i = m_i a_i$. The total force exerted on particle i can be obtained by the gradient of the total potential energy (U) of the system with respect to the position of the particle : $F_i = -\Delta U(r_i)$.

There are various integration algorithms used to solve the ordinary differential equations of an N particles system. The Verlet algorithm is one of the most widely used techniques. There are three forms of the Verlet algorithm: Verlet's original form, the leap-frog and the velocity Verlet algorithm. In the original form, positions at time $(t + \Delta t)$ can be predicted based on positions at time t(r(t)), accelerations a(t), and previous positions r($t - \Delta t$):

(2.1) $$r(t + \Delta t) = 2r(t) - r(t - \Delta t) + \Delta t^2 a(t)$$

9

The velocities are obtained from the formula:

$$(2.2) \qquad v(t) = \frac{r(t + \Delta t) - t(t - \Delta t)}{2\Delta t}$$

The original Verlet form is simple, reversible in time, and allows one to conserve the linear momentum and energy within a simulation. However, it does not allow one to calculate the positions and velocities at the same time. Velocities can only be computed once $r(t + \Delta t)$ is known. To tackle this deficiency, the basic Verlet scheme has been modified into the leap-frog [59] and the velocity [60] schemes. The leap-frog algorithm is defined as follows:

$$(2.3) \qquad r(t + \Delta t) = r(t) + \Delta t v(t + \frac{1}{2}\Delta t)$$

$$(2.4) \qquad v(t + \frac{1}{2}\Delta t) = v(t - \frac{1}{2}\Delta t) + \Delta t a(t)$$

The quantities stored in the memory in the course of a simulations are the current positions r(t) and accelerations a(t) together with the mid-step velocities v(t-12 t). The current velocities are computed by

$$(2.5) \qquad v(t) = \frac{1}{2}(v(t + \frac{1}{2}\Delta t) + v(t - \frac{1}{2}\Delta t))$$

As Eq. 2.5 shows, the leap-frog algorithm does not yet handle the calculation of velocities in a completely satisfactory manner, since it only improves the calculation of velocities by half step. When using the velocity Verlet algorithm, one does store positions, velocities and accelerations all at the same time, and it takes the form:

$$(2.6) \qquad r(t + \Delta t) = r(t) + \Delta t v(t) + \frac{1}{2}\Delta t^2 a(t)$$

$$(2.7) \qquad v(t + \frac{1}{2}\Delta t) = v(t) + \frac{1}{2}\Delta t a(t)$$

$$(2.8) \qquad v(t + \Delta t) = v(t + \frac{1}{2}\Delta t) + \frac{1}{2}\Delta t a(t + \Delta t)$$

The new positions at time $(t + \Delta t)$ are calculated using Eq. 2.6, and the velocities at mid-step are computed using Eq. 2.7. After the forces and accelerations at time $(t + \Delta t)$ are evaluated, the velocities at time $(t + \Delta t)$ can be obtained using Eq.2.8. In addition, kinetic energy, potential energy and other quantities of interest may be evaluated at this time. Therefore, the numerical stability, convenience, and simplicity of velocity Verlet make it perhaps the most widely used algorithm to date. It is important to note that the velocities variables $v(t + \frac{1}{2}\Delta t)$ and $v(t)$ do not precisely represent the conjugated simulation variable to position $r(t + \Delta t)$. A solution to this short coming can be overcome through clever integration algorithms of the canonical ensemble. [61] When simulating other ensembles, one must choose a sufficiently small timestep to minimize the errors induced by imprecise conjugation of simulation variables. The simulations in this thesis use the velocity Verlet integration algorithm.
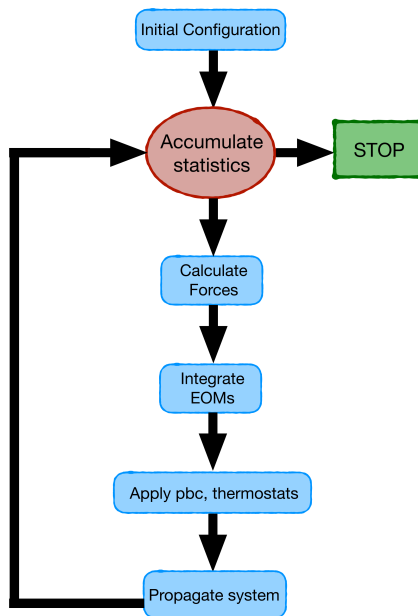
FIGURE 2.1. Schematic of the basic steps involved in MD simulations.

2.1.1. Periodic Boundary Conditions. To avoid surface effects (that in real experiments one avoids by using macroscopic samples), one uses periodic boundary conditions in MD simulations. A simulation box with a relatively small number of atoms is replicated throughout space to form an infinite lattice without any free surfaces. In the course of the simulation (See Fig. 2.2.2), as a particle moves in the original box, its periodic image in each of the neighboring boxes moves

11

in, in exactly the same way. When a particle leaves the central box, one of its images will enter through neighboring units. Since the dynamics of atoms in the original box is exactly the same as that of atoms in the replicated boxes, it is not necessary to store the trajectories of all the images in a simulation, but only the coordinates of the particles in the central box are recorded. The properties of systems are then computed based on the coordinates of atoms in the central box only. The effects of a finite simulation domain on computed quantities have to be tested by increasing the size of the central box for each of the computed properties.

2.1.2. Potentials. In order to carry out a molecular dynamics simulation, it is essential to choose or determine the empirical interatomic potential U, which in turn determines the forces be-tween particles. I will highlight three classical interatomic potentials that are used throughout this thesis: Lennard-Jones, Tersoff, and Kolgomorov-Crespi.

Lennard-Jones (LJ) is the quintessential empirical intermolecular potential; it is both simple and intuitive and is defined as:

$$(2.9) \qquad\qquad U_{ij} = 4\epsilon \left[\left(\frac{\sigma}{r_{ij}} \right)^{12} - \left(\frac{\sigma}{r_{ij}} \right)^{6} \right]$$

where σ helps defines the location of the minimum energy separation between to interacting particles and ϵ is the depth of the potential energy at the minimum. The intuitive formula is composed of a repulsive $\left(\frac{\sigma}{r_{ij}} \right)^{12}$ term and an attractive $\left(\frac{\sigma}{r_{ij}} \right)^{6}$ term. One can see that as we approach zero separation between two interacting particles the potential approaches infinity and repels one another, while as we go to an infinite separation the two particles cease to interact. In between these two extremes we find a position that minimizes the energy between these two particles, where one might expect to find these two particles sitting with respect to one another at zero Kelvin. This potential was designed for noble gases, which only interact via vdW forces and because it models generic vdW forces well it has been used extensively to model the interaction between vdW layers. When one models vdW layers one expects to see a reactive bond order potential, i.e. the Tersoff potential, for in-plane interactions.

The Tersoff potential is a significant potential that is used throughout this thesis. The Tersoff potential is a bond order potential that was originally constructed to study structural properties of silicon, [**62**] and then was later fitted to give structural properties and phonon dispersions of

amorphous carbon. [63] It was later found that the carbon based potential needed to be reparameterized to improve the phonon dispersion relationship of the potential with respect to graphite and graphene, which are of particular interest to this thesis. [64] This reparameterized potential has been employed for the heat transport calculations reported in this dissertation, and it is defined as:

$$(2.10) \qquad U_{ij} = f_C(r_{ij}) \left[f_R(r_{ij}) + b_{ij} f_A(r_{ij}) \right]$$

$$(2.11) \qquad f_C(r) = \begin{cases} 1 & : \quad r < R - D \\ \frac{1}{2} - \frac{1}{2} \sin\left(\frac{\pi}{2} \frac{r-R}{D} \right) & : \quad R - D < r < R + D \\ 0 & : \quad r > R + D \end{cases}$$

$$(2.12) \qquad f_R(r) = A \exp(-\lambda_1 r)$$

$$(2.13) \qquad f_A(r) = -B \exp(-\lambda_2 r)$$

$$(2.14) \qquad b_{ij} = (1 + \beta^n \zeta_{ij}{}^n)^{-\frac{1}{2n}}$$

$$(2.15) \qquad \zeta_{ij} = \sum_{k \neq i,j} f_C(r_{ik}) g\left[\theta_{ijk}(r_{ij}, r_{ik}) \right] \exp\left[\lambda_3{}^m (r_{ij} - r_{ik})^m \right]$$

$$(2.16) \qquad g(\theta) = \gamma_{ijk} \left(1 + \frac{c^2}{d^2} - \frac{c^2}{[d^2 + (\cos\theta - \cos\theta_0)^2]} \right)$$

where f_R is a two-body repulsive term, f_A is an attractive term, and f_C is a smooth potential cutoff function. The function b_{ij} accounts for the dependence of the potential on bonds' order. The summations in the formula are over all neighbors J and K of atom I within a cutoff distance = R + D.

The n, β, λ_2, B, λ_1, and A parameters are only used for two-body interactions. The m, γ, λ_3, c, d, and $\cos\theta_0$ parameters are only used for three-body interactions. The R and D parameters are used for both two-body and three-body interactions. The non-annotated parameters are unitless.

The value of m must be 3 or 1. The Tersoff potential has eleven parameters that are determined by fitting to a set of physical properties obtained from experiments and ab initio calculations, including cohesive energy, bulk modulus and lattice constant.

As mentioned before this potential was specifically reparameterized to reproduce in the in-plane phonon dispersions of graphene/graphite. Because the in-plane lattice thermal conductivity depends strongly on the phonon dispersions of graphene and graphite this potential has been critical to reproducing accurate thermal conductivities. [64, 65, 66] To reproduce cross-plane conductivity this potential is typically paired with a vdW type potential such as Lennard-Jones or Kolgomorov-Crespi.

The LJ potential as previously mentioned can be used to model the interactions between adjacent vdW layers. The LJ potential describes the overall cohesion between graphene layers, but it is much too smooth to describe variations in the relative alignment of adjacent layers. To account for this there is a new class of registry dependent potentials, named Kolgomorov-Crespi (KC) potentials. [67, 68] This potential was originally developed for carbon based systems, but due to its popularity it has been used to model TMDs as well. [69] This potential is defined as:

$$(2.17) \qquad U_{ij} = e^{-\lambda(r_{ij}-z_0)} \left[C + f(\rho_{ij}) + f(\rho_{ji}) \right] - A \left(\frac{r_{ij}}{z_0} \right)^{-6} + A \left(\frac{}{z_0} \right)^{-6}$$

$$(2.18) \qquad \rho_{ij}^2 = \rho_{ji}^2 = x_{ij}^2 + y_{ij}^2 \qquad (\mathbf{n}_i \equiv \hat{\mathbf{z}})$$

$$(2.19) \qquad f(\rho) = e^{-(\rho/\delta)^2} \sum_{n=0}^{2} C_{2n} \left(\rho/\delta \right)^{2n}$$

where the $A \left(\frac{r_{ij}}{z_0} \right)^{-6}$ is an attractive term, similar to that of LJ, the $e^{-\lambda(r_{ij}-z_0)}$ is an exponential atomic core repulsion, and $f(\rho)$ is the energy gain due to interlayer delocalization of π orbitals, which dominates corrugation against interlayer sliding.

This potential accounts for layer sliding and twisting, which is crucial for accurately recreating the shear phonon modes between layers. Having accurate representations of phonon dispersions is important when calculating the thermal conductivity and these modes impact the cross-plane

14

thermal conductivity within vdW materials. It has been shown that the KC potential leads to a more accurate cross-plane thermal conductivity. [32]

To sum up this portion on interatomic potentials, three potentials were used extensively in this work: LJ, Tersoff, and KC. Also, it is important to accurately model both the in-plane and out-of-plane phonon dispersions to yeild reasonable thermal conductivities.

2.1.3. Canonical ensemble. More often than not, MD simulations need to be run at a target temperature in order to thermally equilibrate systems and/or provide a steady state heat flux. Typically in these cases, that temperature control is performed by a thermostat. Currently, there are a variety of methods available to introduce a thermostat in a simulation, such as Andersen, Nosé-Hoover, and Langevin. [70, 71, 72] This thesis is primarily interested in two specific thermostats: Nosé-Hoover and Langevin.

In the Nosé-Hoover method , the equations of motion for the particles (with position r_i, momentum p_i, force F_i, and mass m_i) in the thermostatted region (with N_f degrees of freedom) are

$$(2.20) \qquad \frac{dr_i}{dt} = \frac{p_i}{m_i}; \quad \frac{dp_i}{dt} = F_i - \frac{\pi_0}{Q_0} p_i,$$

where $Q_0 = N_\mathrm{f} k_\mathrm{B} T \tau^2$ is the "mass" of the thermosat variable directly coupled to the system, with τ being a time parameter, and π_0 is the corresponding "momentum".

In the Langevin method, the equations of motion for the particles in the thermostatted region are

$$(2.21) \qquad \frac{dr_i}{dt} = \frac{p_i}{m_i}; \quad \frac{dp_i}{dt} = F_i - \frac{p_i}{\tau} + f_i,$$

$$(2.22) \qquad f_i \propto \sqrt{\frac{k_B T m}{dt\tau}}$$

F_i is the conservative force computed via the interatomic potentials. $\frac{p_i}{\tau}$ is a frictional drag or viscous damping term proportional to the particle's velocity. The proportionality constant for each atom is computed as $\frac{m}{\tau}$, where m is the mass of the particle and *tau* is the damping period. f_i is

15

a force due to solvent atoms at a temperature T randomly bumping into the particle. As derived from the fluctuation/dissipation theorem, the magnitude of this random force as shown above is proportional to $\sqrt{\frac{k_B T m}{dt\tau}}$, where k_B is the Boltzmann constant and dt is the timestep size. Random Gaussian numbers are used to randomize the direction and magnitude of this force.

It is important to note that the Nosé-Hoover thermostat is deterministic while the Langevin thermostat is not. Deterministic thermostats can introduce artifacts into thermal conductivity calculations, which will be a crucial point discussed in Chapter 3.

2.1.4. NEMD. In NEMD simulations [**73**,**74**], one usually calculates the thermal conductivity $\kappa(L)$ of a finite system with length L form the (presumably constant) temperature gradient ∇T and the heat flux Q/S determined from a steady state according to Fourier's law:

$$(2.23) \qquad \kappa(L) = \frac{Q}{A|\nabla T|}.$$

Here, Q is the thermal power across a cross-sectional area A perpendicular to the transport direction and $|\nabla T|$ is the magnitude of the temperature gradient. However, at the nanoscale transport is not necessarily diffusive and when a material leaves the diffusive regime the conventional concept of conductivity as a intrinsic property becomes invalid [**75**]. Therefore, a more appropriate quantity for describing heat transport is the thermal conductance per unit area $G(L)$, which is defined as

$$(2.24) \qquad G(L) = \frac{Q}{A\Delta T},$$

where $\Delta T > 0$ is the temperature difference between the heat source and the sink. In a system with a uniform cross section, the length-dependent conductivity and the conductance are related by the following equation:

$$(2.25) \qquad G(L) \equiv \frac{\kappa(L)}{L}.$$

There are many variants of the NEMD method, both in terms of boundary conditions in the transport direction and in methods of generating the temperature difference. Periodic boundary conditions in the transport direction have been a popular choice, perhaps due to the ease of computer implementation. However, with respect to this dissertation the simulations all contain a few

fixed layers of atoms at the two ends of the sample in the transport direction to achieve the fixed boundary conditions. Next to the two fixed layers, atoms within a noted length were coupled to a hot and a cold thermal bath, respectively. The distance between the two thermal baths defines the system length L, see Fig. 3.1 for an illustration. Excluding the fixed atoms, the whole simulation cell is first equilibrated to the target temperature using a Langevin thermostat, after which it is switched off and local Langevin thermostats are switched on in the leads to realize the hot and cold thermal baths. The local thermostats are applied till a steady state heat flux is achieved. This heat flux, $\frac{Q}{A}$, along with the average temperature difference between the leads, ΔT, is then used to find the thermal conductance using 2.24
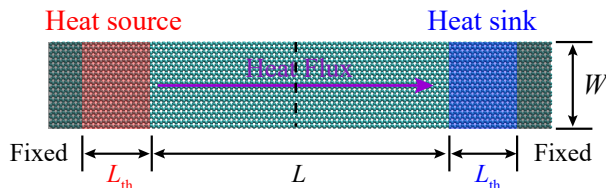
FIGURE 2.2. Schematic illustration of the NEMD simulation setup. As shown the edges contain fixed atoms, then one sees the heat source and sink, and in the middle the device portion. A heat flux is induced, flowing from the heat source to the heat sink across some length L.

2.2. Lattice Dynamics

Atoms in a material undergo regular vibrational motion around their equilibrium positions, a phenomenon that is of fundamental importance for the overall behavior of the material. In crystalline solids in particular these vibrations are periodic in nature and can be described using quasi-particles named phonons that represent collective excitations of the crystal lattice. Commonly descriptions of the vibrational dynamics of a crystal start with a Taylor expansion of the potential energy of the system in terms of the ionic displacements u_i away from a set of static equilibrium positions R_i.

$$(2.26) \qquad U = U_0 + \Phi_i^{\alpha} u_i^{\alpha} + \frac{1}{2}\Phi_{ij}^{\alpha\beta} u_i^{\alpha} u_j^{\beta} \frac{1}{6}\Phi_{ijk}^{\alpha\beta\gamma} u_i^{\alpha} u_j^{\beta} u_k^{\gamma} + \dots$$

Here, the Einstein summation convention applies for all repeated indices. The letters i, j, and k denote atom labels while Greek letters denote the Cartesian axes: x, y, and z. U_0 is the constant

17

energy, which is typically chosen to be 0 out of convenience. The term $\Phi_i^\alpha u_i^\alpha$ vanishes since the expansion is carried around the static equilibrium positions, for which the forces vanish by definition. The expansion coefficients Φ are the so-called force constants.

2.2.1. Force Constants. The force constants relate the displacements u_i not only to the potential energy U of the system but also the atomic forces F_i^α according to

(2.27) $$F_i^\alpha = -\Phi_{ij}^{\alpha\beta} u_j^\beta - \frac{1}{2} \Phi_{ijk}^{\alpha\beta\gamma} u_j^\beta u_k^\gamma - ...$$

The force constants encode essential information about the vibrational properties of a system and form the building blocks of lattice dynamics in terms of phonons.

With respect to this dissertation the force constants are obtained using finite differences. For example in the case of the second order force constant matrix can be approximated as:

(2.28) $$\Phi_{ij}^{\alpha\beta} \approx \frac{F_j^\beta(r_i^\alpha - \delta) - F_j^\beta(r_i^\alpha + \delta)}{2\delta}.$$

where δ denotes a finite displacement of atom i along the Cartesian direction $/alpha$. While this approach can be readily extended to higher order differences, the number of calculations needed quickly increases even if the crystal symmetry and intrinsic symmetries of the force constant tensors are taken into account.

The dynamical matrix is the mass-weighted second order force constant matrix of a system of atoms:

(2.29) $$D_{ij}^{\alpha\beta} = \frac{1}{\sqrt{m_i m_j}} \frac{\partial^2 U}{\partial u_i^\alpha \partial u_j^\beta}$$

Phonon frequencies, ω_μ, are calculated from the square root of the eigenvalues, ω_μ^2, of the dynamical matrix as shown in 2.30.

(2.30) $$D_{ij}^{\alpha\beta} \epsilon_\mu^{j\beta} = \omega_\mu^2 \epsilon_\mu^{i\alpha}$$

Most dynamical matrices within this thesis are calculated using the dynamical matrix command from LAMMPS.

2.2.2. Cell Relaxation. As shown finite displacements from lattice sites can be an important building block to form FCMs. One typically expects the system to have all it's particles at their lattice sites to perform such a calculation. In order to create a system where the atoms are at their lattice sites, one must minimize the energy of the structure to relax particles into their most likely location at 0K. In addition to minimizing the total energy w.r.t. particle positions, it is equally as important to do the same for the lattice constants, also known as cell relaxation.

Some systems, such as multilayer vdW systems, the locations of atoms and/or the systems lattice constants at 0K are not accurate approximations for the same system at room temperature. In the case of vdW materials, thermal expansions as temperatures rise push adjacent layers further apart from one another, thus changing the equilibrium positions of atoms w.r.t. to one another. A particular way in which one can ascertain the new equilibrium atomic positions and/or the lattice constants is to average over snapshots taken from the isobaric-isothermal ensemble. Two specific ways in which this is currently done is through sampling the isobaric-isothermal ensemble via molecular dynamics or by generating frames and averaging over them as shown in Errea et. al. [**76**] This step has been shown to be crucial in accurately calculating the cross-plane thermal conductivity in heterojunctions. [**77**]

2.2.3. Elastic Scattering Kernel Method. Calculating thermal conductance of devices which have defects on the order phonon mean free path or interfaces is extremely challenging if not infeasable for methods such as BTE, and impractical for MD based methods, if modeling devices well below the Debye temperature. To overcome these challenges one can used GFE based methods to investigate elastic phonon scattering from impurities, defects, disorder or interfaces. One such method that is frequently employed in this thesis is a scattering matrix based approach called elastic scattering kernel method (ESKM). [**78**]

In this method we consider a phonon wave packet, represented by a weight-normalized displacement field u, traveling through an open system made of semi-infinite reservoirs connected by an arbitrary structure (defect). Our goal is to determine the thermal energy exchanged between the reservoirs through the defect in stationary nonequilibrium conditions (i.e., when the reservoirs are kept at different temperatures). In the harmonic approximation, the equation of motion for the displacement field $u(t)$ is $\ddot{u}(t) = Du(t)$, where D is the force constant matrix. The real-valued state

u can be decomposed in terms of the complex valued eigenstates $v(\omega)$ of D. Given the state $u(\tau_0)$ and its eigen-decomposition coefficients $g_{\tau_0}(\omega)$, the time propagation of u is

$$(2.31) \qquad u(t) = \int [g_{\tau_0}(\omega)v(\omega)e^{-i\omega(t-\tau_0)} + cc.]d\omega$$

Let P be the projector associated with the degrees of freedom of an arbitrary part P of the system. To get the energy exchanged between P and the rest of the system, one can balance the time derivatives of the work from P to the whole system and vice versa, thus obtaining

$$(2.32) \qquad \dot{E}_P(t) = \langle \dot{u}(t)|[P,D]|u(t)\rangle$$

The energy of P in stationary conditions $(E_P(\infty))$ is found by integrating 2.32 to the infinite time limit. Substituting u with its eigen decomposition in 2.31 in the integral leads to

$$(2.33) \qquad E_P(\infty) = -2\pi i \int \hbar\omega |g_{\tau_0}(\omega)|^2 \langle v(\omega)|[P,D]|v(\omega)\rangle d\omega$$

All information concerning the initial state lies in the weights $g_{\tau_0}(\omega)$, which can be taken as the statistical distribution of the states $|v\rangle$ when simulating a system at finite temperature. In the stationary nonequilibrium case, those weights refer to the rate of phonons emitted from the reservoirs [i.e., one-dimensional (1D) phonon gas obeying Bose-Einstein statistics]:

$$(2.34) \qquad |g_{\tau_0}(\omega)|^2 = \frac{1}{2\pi}\frac{1}{e^{\frac{\hbar\omega}{k_b T}} - 1} = \frac{1}{2\pi}f(\omega, T)$$

where $f(\omega, T)$ is the Bose-Einstein distribution function at the reservoir temperature T. In order to evaluate 2.33, the eigensolutions $|v(\omega)\rangle$ of the open system have to be expressed in terms of a convenient basis made of a single phonon mode $|\psi_{i\in A}^{in}(\omega)\rangle$ coming from a reservoir A into the defect, and the set of phonon modes $\psi_j^{out}(\omega)$ coming out of the defect toward the reservoirs:

$$(2.35) \qquad |v_i(\omega)\rangle = |\psi_i^{in}(\omega)\rangle + \sum_j S_{ji}(\omega)|\psi_j^{out}(\omega)\rangle + |v_i^{def}(\omega)\rangle$$

where both defect displacements and reservoir surface states at the interfaces are included in $|v_i^{def}(\omega)\rangle$. The scattering tensor $S(\omega)$ maps the incoming phonons $|\psi_i^{in}(\omega)\rangle$ onto the outgoing phonons $|\psi_j^{out}(\omega)\rangle$. As the energy carried by any incoming or outgoing phonon with frequency ω is

quantized as $\hbar\omega$, 2.33 provides the following normalization and orthogonality conditions:

$$\langle\psi^{in}_{i\in A}(\omega)|[P_A, D]|\psi^{in}_{j\in A}(\omega)\rangle = \frac{-i\hbar}{2\pi}\delta_{ij}$$

(2.36)
$$\langle\psi^{out}_{i\in A}(\omega)|[P_A, D]|\psi^{out}_{j\in A}(\omega)\rangle = \frac{i\hbar}{2\pi}\delta_{ij}$$

$$\langle\psi^{in}_{i\in A}(\omega)|[P_A, D]|\psi^{out}_{j\in A}(\omega)\rangle = 0$$

where P_A denotes the projector on reservoir A. Combining the stationary nonequilibrium weights of 2.34 with 2.33, and observing the conditions of 2.36, one obtains the stationary energy transfer between reservoirs A and B:

(2.37)
$$\Phi_{A\rightarrow B} = \int \frac{\hbar\omega}{2\pi}\sum_{i\in A}\sum_{j\in B}|S_{ij}(\omega)|^2[f(\omega, T_A) - f(\omega, T_B)]d\omega$$

Once $S(\omega)$ is obtained by computing the eigenstates $|v(\omega)\rangle$, the energy flux between two reservoirs A, B is determined using the transmission coefficient $\mathcal{T}_{AB}(\omega) = \sum_{i\in A}\sum_{j\in B}|S_{ij}(\omega)|^2$. The corresponding thermal conductance is given by the Landauer formula as the limit of 2.37 when $T_A \rightarrow T_B$:

(2.38)
$$\sigma_{AB}(T) = \int \frac{\hbar\omega}{2\pi}\mathcal{T}_{AB}(\omega)\dot{f}(\omega, T)d\omega$$

Using 2.38 one can calculate the ballistic thermal conductance of devices which have defects on the order of the phonon mean free path. This is incredibly useful for vdW interfaces that are well below their debye temperature. [65]

2.3. Summary

Within this dissertation two major computational methods of calculating thermal conductance were employed, NEMD and ESKM. NEMD is an MD based method, which integrates Newtons equations of motion and approaches the problem from a real space perspective. ESKM is an AGF equivalent that solves the problem in reciprocal space. Both methods, in the context of this dissertation, rely on empirical interatomic potentials and their accuracy. The strengths of NEMD includes handling anharmonicty effortlessly, where a major weakness of ESKM is that it does not. ESKM, however, handles phonon populations and elastic scattering well below the

Debye temperature, whereas NEMD is limited to classical (Boltzmann) populations. Both of these methods are useful for materials with interfaces and/or materials that have defects on the order of the mean free path of major heat carriers, which is why they are predominant methods for calculating the thermal conductance across vdW layers that are not within a supercell.

CHAPTER 3

Influence of Thermostatting on Non-Equilibrium Molecular Dynamics Simulations

3.1. Introduction

Molecular dynamics (MD) is the most versatile and complete classical method to study heat transport at the nanoscale, which is vital for many technological applications [**48**, **49**, **50**] such as thermoelectric energy conversion and thermal management of electronic devices. As the interatomic interactions used in MD simulations have become increasingly accurate by using quantum mechanical density functional based equilibrium MD [**51**, **52**, **53**], nonequilibrium MD [**54**] and approach-to-equilibrium MD [**55**, **56**], it is crucial to develop a deeper understanding of the MD methods used for heat transport studies. In this work, we focus on one of the most popular MD methods for heat transport: the nonequilibrium MD (NEMD) method.

In NEMD simulations [**73**, **74**], one usually calculates the thermal conductivity $\kappa(L)$ of a finite system with length L form the (presumably constant) temperature gradient ∇T and the heat flux Q/S determined from a steady state according to Fourier's law:

$$(3.1) \qquad \kappa(L) = \frac{Q}{S|\nabla T|}.$$

Here, Q is the thermal power across a cross-sectional area S perpendicular to the transport direction and $|\nabla T|$ is the magnitude of the temperature gradient. However, at the nanoscale transport is not *diffusive* and the conventional concept of conductivity as a materials property becomes invalid [**75**]. For example, thermal transport at the nanoscale, especially in materials with high thermal conductivity such as graphene [**9**, **66**, **79**], is almost *ballistic* with a length-dependent $\kappa(L)$

---

[0]The work described in this Chapter is reproduced in partial or full form from the following publication:

- Z. Li, et. al. J. Chem. Phys. 2019, 151, 234105. [**29**].

increasing with increasing L. In this situation, a more appropriate quantity for describing heat transport is the thermal conductance per unit area $G(L)$, which is defined as

$$(3.2) \qquad G(L) = \frac{Q}{S\Delta T},$$

where $\Delta T > 0$ is the temperature difference between the heat source and the sink. This quantity is constant in the ballistic regime and only weakly dependent on the system length in the nanoscale transport regime. In a system with a uniform cross section, the length-dependent conductivity and the conductance are related by the following equation:

$$(3.3) \qquad G(L) \equiv \frac{\kappa(L)}{L}.$$

A question then arises as to whether the conductivity and conductance calculated using Eqs. (3.1) and (3.2) are consistent with each other. Clearly, if the temperature gradient is replaced by $\Delta T/L$, κ and G as calculated from Eqs. (3.1) and (3.2) imply Eq. (3.3). However, in most previous works using NEMD simulations, the temperature gradient was *not* calculated as $\Delta T/L$, but was instead determined as the slope of the so-called linear region of the temperature profile, ignoring the nonlinear parts of the temperature profile near the thermal baths. This practice assumes that transport is diffusive, i.e. in accordance with Fourier's law that predicts a linear temperature profile at steady state conditions. However, recent studies suggest that such nonlinearities have a physical origin, related to transport in finite size systems [80,81]. If the nonlinear parts need to be excluded, then $|\nabla T| \neq \Delta T/L$, leading to an inconsistency among Eqs. (3.1)-(3.3).

In this work we take graphene, a material with an exceptionally high lattice thermal conductivity and long phonon mean free paths [9, 79], as an example to explore the interpretation of NEMD results both in the ballistic and in the ballistic-to-diffusive transport regimes. We chose graphene and graphene nanostructures because they are particularly difficult to treat by MD due to poor ergodicity in the simulations. In the ballistic limit, we compare NEMD (with spectral decomposition [82, 83, 84]) against the standard atomistic Green's function (AGF) method [45, 85, 86]. We show that in order to reach an agreement with the AGF method, one needs to use Eq. (3.2) to calculate the conductance and regard ΔT as the temperature difference between the hot and cold thermostats, not excluding any local nonlinear regions of the temperature profile. If one first

calculates a conductivity using Eq. (3.1) from the linear region of the temperature profile and then converts it to the conductance using Eq. (3.3), one obtains a ballistic conductance much larger than the correct one.

On the other hand, although the NEMD method has been shown to be fully equivalent to the equilibrium MD (EMD) and the homogeneous nonequilibrium MD (HNEMD) methods in the diffusive limit [84, 87, 88, 89, 90, 91], the influence of the simulation details in the NEMD method on the results in the ballistic-to-diffusive crossover regime have not been addressed. Here, we clarify the interpretation of the NEMD results by comparing them against those from the HNEMD method (also with spectral decomposition) [88]. Again, we show that one should not calculate the thermal conductivity using Eq. (3.1) from a purely linear region of the temperature profile. Instead, the correct way is to calculate the conductance from Eq. (3.2) with ΔT being the temperature difference between the heat source and sink and then convert it to the conductivity using Eq. (3.3). That is, one should calculate the conductivity as

$$(3.4) \qquad \kappa(L) = \frac{Q}{S(\Delta T/L)}.$$

Finally, we address thermal rectification in asymmetric graphene nanostructures, showing that the choice of thermostatting method and related parameters is of crucial importance, not only to calculate G in the ballistic regime, but also to estimate correctly the thermal rectification efficiency of these systems.

This paper is organized as follows. In Sec. 3.2, we review the various numerical phonon thermal transport methods used in this work, including the AGF method based on harmonic force constants (Sec. 3.2.1), the NEMD method (Sec. 3.2.2), the HNEMD method (Sec. 3.2.3), and the spectral decomposition method (Sec. 3.2.4). After briefly presenting the AGF results in Sec. 3.3.1, we compare the NEMD results against the AGF results in Sec. 3.3.2. Then, we examine the temperature profiles in the NEMD simulations in Sec. 3.3.3. In Sec. 3.3.4, we present the NEMD results for the ballistic-to-diffusive transport regimes and compare them with the HNEMD results. Connection between the NEMD method and the Boltzmann transport equation method is discussed in Sec. 3.3.5. Finally in Sec. 3.3.6 we show the application of NEMD to thermal rectification in

asymmetric graphene devices. In Sec. 3.4, we give a summary and the main conclusions of this work.

3.2. Methods

3.2.1. Atomistic Green's function method. Following the early work by Mingo and Yang [**45**], the AGF method has become a standard tool to study ballistic phonon transport in the harmonic approximation. In this method, one can calculate the phonon transmission $\mathcal{T}(\omega)$ between two leads as a function of the phonon frequency ω. The ballistic conductance can be calculated through the Landauer expression as [**46**, **47**]:

$$(3.5) \qquad G = \int_0^\infty \frac{d\omega}{2\pi} G(\omega),$$

where the spectral conductance $G(\omega)$ is

$$(3.6) \qquad G(\omega) = G_c(\omega) = \frac{k_B}{S} \mathcal{T}(\omega)$$

using classical (Boltzmann) statistics, and

$$(3.7) \qquad G(\omega) = G_q(\omega) = \frac{k_B}{S} \frac{x^2 e^x}{(e^x - 1)^2} \mathcal{T}(\omega)$$

using quantum (Bose-Einstein) statistics. Here, $x = \hbar\omega/k_B T$, where $\hbar$ is Planck's constant, k_B is Boltzmann's constant, and T is the system temperature. That is, in the harmonic approximation, the ratio between the quantum conductance and the classical conductance is the ratio between the quantum modal heat capacity $k_B x^2 e^x/(e^x - 1)^2$ and the classical modal heat capacity k_B.

As in the case of electron transport [**75**], there are many equivalent representations of the phonon transmission [**85**]. Here, we adopt Caroli's formula [**92**]:

$$(3.8) \qquad \mathcal{T}(\omega) = \text{Tr}[\mathcal{G}(\omega)\Gamma_L(\omega)\mathcal{G}^\dagger(\omega)\Gamma_R(\omega)],$$

where

$$(3.9) \qquad \mathcal{G}(\omega) = \frac{1}{\omega^2 - D - \Sigma_L(\omega) - \Sigma_R(\omega)}$$

26

is the retarded Green's function for the system, $\mathcal{G}^{\dagger}(\omega)$ is the advanced Green's function, D is the dynamical matrix of the system, and $\Sigma_{\mathrm{L/R}}(\omega)$ is the self energy matrix of the left (right) lead. The coupling matrices $\Gamma_{\mathrm{L}}(\omega)$ and $\Gamma_{\mathrm{R}}(\omega)$ are the imaginary part of the self energy matrices:

$$(3.10) \qquad \Gamma_{\mathrm{L/R}}(\omega) = i \left[\Sigma_{\mathrm{L/R}}(\omega) - \Sigma_{\mathrm{L/R}}^{\dagger}(\omega) \right].$$

The dynamical matrix is the mass-weighted Hessian matrix of the empirical potential as used in our MD simulations:

$$(3.11) \qquad D_{\mu\nu} = \frac{1}{\sqrt{m_\mu m_\nu}} \frac{\partial^2 U}{\partial u_\mu \partial u_\nu},$$

where U is the total potential energy of the system and u_μ is a component of the displacement vector of an atom in the system with a mass of m_μ. The self energy matrices can be obtained from the dynamical matrices for the semi-infinite leads by using an iterative method [93]. In numerical calculations, each atom contributes three degrees of freedom. The elements of the dynamical matrix can also be expressed as

$$(3.12) \qquad D_{ij}^{ab} = \frac{1}{\sqrt{m_i m_j}} \frac{\partial^2 U}{\partial u_i^a \partial u_j^b},$$

where i and j run over the atom indices, while a and b run over the three directions $(a, b = x, y, z)$. From the relationship between force and potential, $F_i^a = -\partial U / \partial u_i^a$, we can write the above equation as

$$(3.13) \qquad D_{ij}^{ab} = -\frac{1}{\sqrt{m_i m_j}} \frac{\partial F_i^a}{\partial u_j^b}.$$

This can be evaluated using a finite displacement δ:

$$(3.14) \qquad D_{ij}^{ab} \approx \frac{1}{\sqrt{m_i m_j}} \frac{F_i^a(r_j^b - \delta) - F_i^a(r_j^b + \delta)}{2\delta}.$$

Here $F_i^a(r_j^b \pm \delta)$ is the total force on atom i in the a direction caused by displacing the position of atom j in the b direction by an amount of $\pm\delta$ (keeping all the other atoms at their relaxed positions). Here we use $\delta = 0.005$ Å.

3.2.2. NEMD method. There are many variants of the NEMD method, both in terms of boundary conditions in the transport direction and methods of generating the temperature difference. Periodic boundary conditions in the transport direction have been a popular choice, perhaps due to the ease of computer implementation. However, this choice cannot be directly compared to the AGF calculation setup, and is usually different from experimental situations, although it can give equivalent results as obtained using fixed boundary conditions as long as the sample length L is carefully defined [89]. We thus consider fixed boundary conditions in the transport direction. Regarding the methods of generating temperature difference, there are many algorithms, including the constant heat current method [94, 95], the momentum swapping method [96, 97], and methods based on thermostats. In both the constant heat current method and the momentum swapping method, the temperature difference cannot be precisely controlled. We therefore use thermostatting methods to generate the temperature difference.

In our NEMD simulations, we fixed a few layers of atoms at the two ends of the sample in the transport direction to achieve the fixed boundary conditions. Next to the two fixed layers, atoms within a length of L_{th} were coupled to a hot and a cold thermal bath, respectively. The distance between the two thermal baths defines the system length L, see Fig. 3.1 for an illustration. The whole simulation cell was first equilibrated at the target temperature using the Berendsen thermostat [98] for 1 ns, after which we switched off the global thermostat and switched on the local thermostats to realize the hot and cold thermal baths. The local thermostats were applied for 11 ns, while steady state can be well achieved within the first 1 ns in all our simulated systems. We used the data within the last 10 ns to determine the temperature profile and the nonequilibrium heat current. Each NEMD simulation has been repeated three times and the statistical errors are very small and are thus omitted in the relevant figures.

To realize the local thermostats, we consider both the Nosé-Hoover chain [99, 100, 101] and the Langevin methods [3, 72]. In the Nosé-Hoover chain method , the equations of motion for the particles (with position $\boldsymbol{r}_i$, momentum $\boldsymbol{p}_i$, force $\boldsymbol{F}_i$, and mass m_i) in the thermostatted region (with N_{f} degrees of freedom) are

$$(3.15) \qquad \frac{d\boldsymbol{r}_i}{dt} = \frac{\boldsymbol{p}_i}{m_i}; \quad \frac{d\boldsymbol{p}_i}{dt} = \boldsymbol{F}_i - \frac{\pi_0}{Q_0}\boldsymbol{p}_i,$$
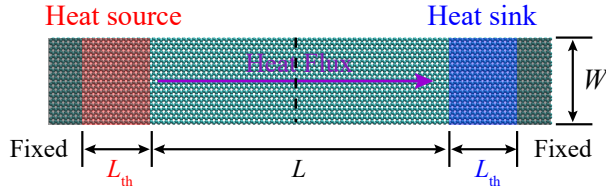
FIGURE 3.1. Schematic illustration of the NEMD simulation setup. We consider a single-layer suspended graphene sheet with width W and length L. A heat source region of length L_{th} is coupled to a thermostat with a temperature of $T + \Delta T/2$ and a heat sink region of the same length is coupled to a thermostat with a temperature of $T - \Delta T/2$. To prevent the atoms in the source and sink regions from sublimating and to keep the in-plane stress at zero, a few extra layers of atoms are fixed (forces and velocities are reset to zero during the time integration). Heat flux can be measured as the heat transfer rate dE/dt in the local thermal baths divided by the cross-sectional area $S = Wh$, where $h = 0.335$ nm is the convectional thickness of graphene. In this study, the width is fixed to $W = 10$ nm and periodic boundary conditions are applied in the direction of W.

where $Q_0 = N_{\text{f}} k_{\text{B}} T \tau^2$ is the "mass" of the thermosat variable directly coupled to the system, with τ being a time parameter, and π_0 is the corresponding "momentum". In the Langevin method, the equations of motion for the particles in the thermostatted region are

$$(3.16) \qquad \frac{d\boldsymbol{r}_i}{dt} = \frac{\boldsymbol{p}_i}{m_i}; \quad \frac{d\boldsymbol{p}_i}{dt} = \boldsymbol{F}_i - \frac{\boldsymbol{p}_i}{\tau} + \boldsymbol{f}_i,$$

where τ is a time parameter and $\boldsymbol{f}_i$ is a random force with a variation determined by the fluctuation-dissipation relation to recover the canonical ensemble distribution.

There are many implementations of these thermostats and here we use a velocity-Verlet integrator [102, 103]. In both thermostatting methods, there is a time parameter τ that dictates the coupling between the thermostat and the system. In the Nosé-Hoover chain method, the thermostat mass is proportional to τ^2 and a larger τ would, in principle, decouple adiabatically the degrees of freedom of the thermostat from those of the system. However, when τ is too large the large inertia of the thermostat degrees of freedom produces unphysical fluctuations in the kinetic energy of the system [104]. In the Langevin method, τ is the inverse of the coefficient of friction and a larger τ also gives a weaker temperature control. The major difference between them is that in the Nosé-Hoover chain method, the temperature in the thermal bath region is adjusted globally and

deterministically by re-scaling the velocities of the atoms with a common factor, while in Langevin dynamics, the velocities of the atoms are adjusted locally and stochastically.

3.2.3. HNEMD method. Although the focus of this work is the NEMD method, we also use some results from the HNEMD method for comparison. This method is physically equivalent to the Green-Kubo method but is computationally much faster [88]. In this method, an external force of the form [88]

$$(3.17) \qquad \boldsymbol{F}_i^{\text{ext}} = E_i \boldsymbol{F}_{\text{e}} + \sum_{j \neq i} \left(\frac{\partial U_j}{\partial \boldsymbol{r}_{ji}} \otimes \boldsymbol{r}_{ij} \right) \cdot \boldsymbol{F}_{\text{e}},$$

is added to each atom i, driving the system out of equilibrium. Here, E_i and U_i are the total and potential energies of atom i, respectively, $\boldsymbol{r}_{ij} \equiv \boldsymbol{r}_j - \boldsymbol{r}_i$, and $\boldsymbol{r}_i$ is the position of particle i. The parameter $\boldsymbol{F}_{\text{e}}$ is of the dimension of inverse length and should be small enough to keep the system within the linear response regime. A global thermostat should be applied to control the temperature of the system. The driving force will induce a nonequilibrium heat current $\langle \boldsymbol{J} \rangle_{\text{ne}}$ linearly proportional to $\boldsymbol{F}_{\text{e}}$. For a given transport direction, this linear relation provides a way to compute the thermal conductivity in this direction:

$$(3.18) \qquad \kappa(t) = \frac{\langle J(t) \rangle_{\text{ne}}}{TVF_{\text{e}}},$$

where T is the system temperature, V is the system volume, $J = |\boldsymbol{J}|$, and $F_{\text{e}} = |\boldsymbol{F}_{\text{e}}|$. For a many-body potential, the heat current $\boldsymbol{J}$ is given by [105]

$$(3.19) \qquad \boldsymbol{J} = \sum_i \boldsymbol{v}_i E_i + \sum_i \sum_{j \neq i} \boldsymbol{r}_{ij} \left(\frac{\partial U_j}{\partial \boldsymbol{r}_{ji}} \cdot \boldsymbol{v}_i \right),$$

where $\boldsymbol{v}_i$ is the velocity of atom i. Because there is no boundary scattering in this method, the calculated thermal conductivity can be considered as that for an infinitely long system, as long as a sufficiently large periodic simulation cell is used. For graphene, a rectangular cell of dimension $25 \times 25 \text{ nm}^2$ is large enough to eliminate the finite-size effects [88].

3.2.4. Spectral decomposition method . In both the NEMD and the HNEMD methods, a nonzero nonequilibrim heat current exists and can be spectrally decomposed. Considering an imaginary interface separating two groups of atoms A and B as schematically shown in Fig. 3.1,

this nonequilibrim heat current can be expressed as [84]

$$Q = -\sum_{i \in A} \sum_{j \in B} \left\langle \left(\frac{\partial U_i}{\partial \boldsymbol{r}_{ij}} \cdot \boldsymbol{v}_j - \frac{\partial U_j}{\partial \boldsymbol{r}_{ji}} \cdot \boldsymbol{v}_i \right) \right\rangle . \tag{3.20}$$

For a spatially homogeneous system, $Q/S = J/V$, where J is the magnitude of the heat current given in Eq. (3.19).

In the spectral decomposition method developed by Sääskilahti *et al.* [82, 83], one first defines the force-velocity correlation function, which can be expressed as

$$K(t) = -\sum_{i \in A} \sum_{j \in B} \left\langle \left(\frac{\partial U_i}{\partial \boldsymbol{r}_{ij}}(0) \cdot \boldsymbol{v}_j(t) - \frac{\partial U_j}{\partial \boldsymbol{r}_{ji}}(0) \cdot \boldsymbol{v}_i(t) \right) \right\rangle \tag{3.21}$$

for a general many-body potential [84]. This correlation function reduces to the nonequilibrium heat current in Eq. (3.20) at zero correlation time. The spectrally decomposed heat current $\tilde{K}(\omega)$ can be obtained from a Fourier transform of the force-velocity correlation function

$$\tilde{K}(\omega) = \int_{-\infty}^{\infty} dt e^{i\omega t} K(t). \tag{3.22}$$

The inverse Fourier transform is

$$K(t) = \int_{-\infty}^{\infty} \frac{d\omega}{2\pi} e^{-i\omega t} \tilde{K}(\omega). \tag{3.23}$$

Because

$$Q = K(t = 0) = \int_0^{\infty} \frac{d\omega}{2\pi} \left[2\tilde{K}(\omega) \right], \tag{3.24}$$

we obtain the following spectral decomposition of the *thermal conductance* in NEMD simulations:

$$G(\omega) = \frac{2\tilde{K}(\omega)}{S\Delta T} \quad \text{with} \quad G = \int_0^{\infty} \frac{d\omega}{2\pi} G(\omega). \tag{3.25}$$

Similarly, the *thermal conductivity* from HNEMD simulations can be spectrally decomposed as:

$$\kappa(\omega) = \frac{2\tilde{K}(\omega)}{STF_{\rm e}} \quad \text{with} \quad \kappa = \int_0^{\infty} \frac{d\omega}{2\pi} \kappa(\omega). \tag{3.26}$$

3.2.5. Details on the numerical calculations. The NEMD, HNEMD, and spectral decomposition methods have been implemented in the highly efficient Graphics Processing Units

31

Molecular Dynamics (GPUMD) package [106, 107, 108], which is the code we used for most of the MD simulations. The simulations of thermal rectification in asymmetric graphene devices were performed using the Large-scale Atomic/Molecular Massively Parallel Simulator (LAMMPS) package [109]. We used the Tersoff potential [110] optimized for graphene systems [64]. For multilayer graphene the van der Waals interactions among different layers were modeled with the Lennard-Jones potential with $\varepsilon = 3.296$ eV and $\sigma = 3.55$ Å [111]. A time step of 0.5 fs, which ensures good energy conservation, was used in all the MD simulations. The AGF calculations were performed by using a Matlab code, which is also publicly available [112]. More details on simulations of thermal rectification are presented in Sec. 3.3.6.
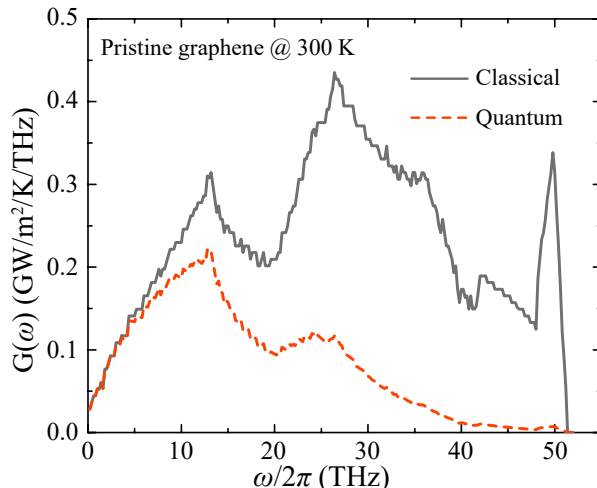
FIGURE 3.2. Spectral ballistic thermal conductance as a function of phonon frequency obtained from the harmonic AGF calculations. The quantum thermal conductance is obtained from the classical one by multiplying a factor (related to spectral heat capacity) that is unity in the low-frequency limit and zero in the high-frequency limit.

3.3. Results and Discussion

3.3.1. Ballistic thermal conductance from AGF calculations. We first calculate the ballistic conductance of the graphene sheet (with the same width as in the NEMD simulations) using the AGF method. The ballistic spectral phonon conductance, obtained by using either classical or quantum statistics, is shown in Fig 3.2. Because anharmonicity is totally absent in this method, the classical conductance (which is essentially the transmission) exhibits many quantized

plateaus. By integrating the spectral conductance with respect to the frequency, we can get the total thermal conductance, which is about 12.2 and 4.2 GWm^{-2}K^{-1} at room temperature in the cases of classical and quantum statistics, respectively. The quantum thermal conductance obtained here agrees with that reported by Serov *et al.* [**113**] where the same empirical potential was used.
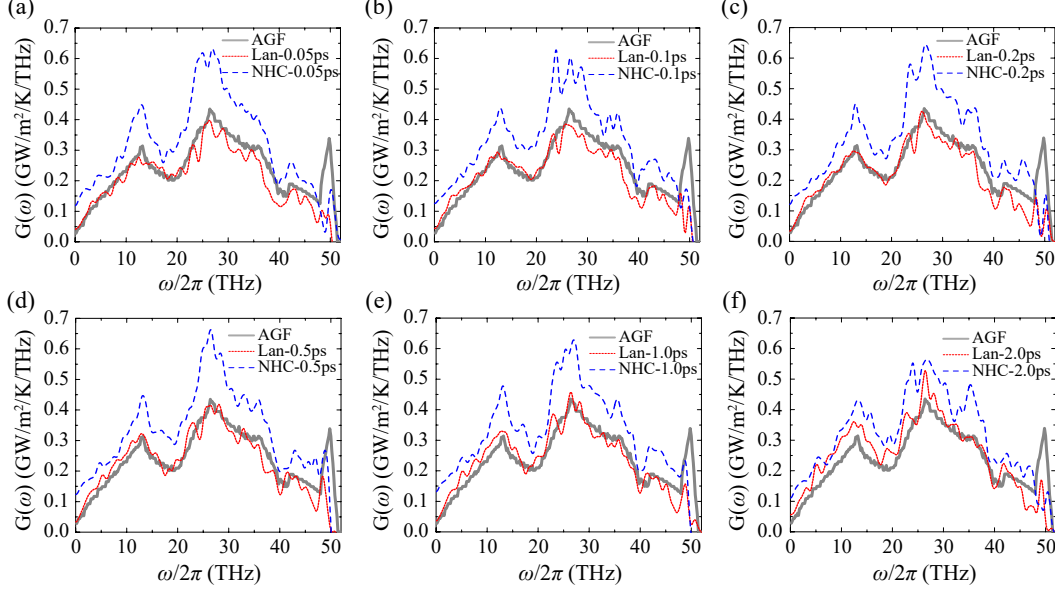
FIGURE 3.3. Spectral conductance of a short graphene sheet with $L = 10$ nm at 300 K from NEMD simulations using the Nosé-Hoover chain (thin dashed lines; labeled by NHC-τ) and the Langevin (thin solid lines; labeled by Lan-τ) thermostatting methods, compared to the fully ballistic conductance (thick solid lines) obtained from the harmonic AGF calculations. From (a) to (f), the time parameter τ in both thermostatting methods increases from 0.05 ps to 2 ps. The thermal baths are $L_{\text{th}} = 40$ nm long in all the simulations here.

3.3.2. Comparison between NEMD and AGF in the ballistic regime. To obtain the ballistic conductance using the NEMD method, we set the system length as $L = 10$ nm and the simulation temperature as $T = 300$ K. The temperatures of the hot and cold thermal baths were set to $T \pm \Delta T/2$ with $\Delta T = 10$ K. For such a short sample, anharmonicity caused by phonon-phonon scattering can be largely ignored (except for the optical phonons with the highest frequencies) and the phonon transport can be essentially regarded as ballistic. Here, we calculate the temperature difference from the actual average temperatures in the thermal baths. In the next subsection, we will examine the temperature profile and its implications in the interpretation of the results.
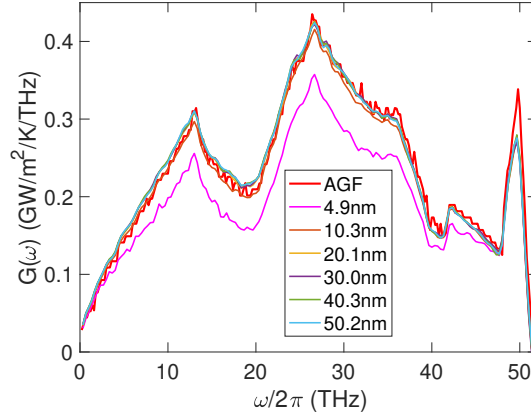
FIGURE 3.4. Spectral conductance of a short graphene sheet with $L = 10$ nm at 20 K from NEMD simulations using the Langevin thermostatting method with a fixed coupling time of $\tau = 0.5$ ps but different bath lengths (from $L_{\text{th}} = 4.9$ nm to 50.2 nm), compared to the fully ballistic conductance obtained from the harmonic AGF calculations.

Figure 3.3 compares the spectral conductance obtained from the NEMD simulations (with spectral decomposition) using both the Nosé-Hoover chain and the Langevin thermostatting methods, against that from the AGF method. For the results from Fig. 3.3(a) to 3.3(f), the parameter τ in both thermostatting methods is increased from 0.05 ps to 2 ps. Because the MD simulations are classical, we need to compare with the classical ballistic thermal conductance from the AGF method.

The spectral conductance obtained by using the Nosé-Hoover chain thermostatting method is significantly larger than the reference AGF value, while that obtained by using the Langevin thermostatting method agrees with the AGF reference value well for intermediate τ values (0.1 ps to 1 ps). Chen *et al.* [**114**] also recommended using intermediate τ values in NEMD simulations of heat conduction. This is reasonable, as too small a τ results in too strong a perturbation on the system, and too large a τ results in too weak a control of the temperatures in the thermal baths.

We note that we have used a relatively long heat bath of $L_{\text{th}} = 40$ nm in the above calculations. It has been pointed out [**82**,**83**] that L_{th} in the Langevin thermostatting method should exceed the bath-induced phonon mean free path, $v_g\tau$, to ensure full thermalization, where v_g is the average phonon group velocity of the material. In graphene, v_g is of the order of 20 km s^{-1} [**84**], and choosing a coupling time of $\tau = 0.5$ ps gives $L_{\text{th}} = 10$ nm. This is confirmed in Fig. 3.4, which

34

shows that the ballistic conductance is underestimated when $L_{\text{th}} = 4.9$ nm, while when $L_{\text{th}} \geq 10.3$ nm, the conductance is essentially independent of the bath length and matches the reference AGF value. The bath length of $L_{\text{th}} = 40$ nm used in this work is large enough for all the τ values we considered.
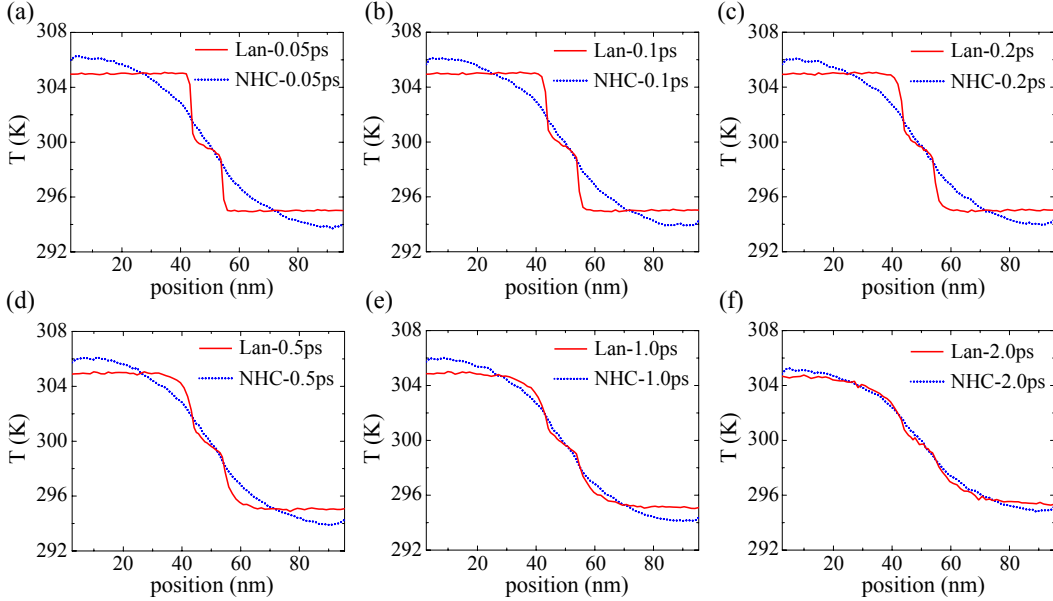
FIGURE 3.5. Temperature profiles in the NEMD simulations corresponding to the spectral conductances in Fig. 3.3. From (a) to (f), the time parameter τ in both thermostatting methods increases from 0.05 ps to 2 ps. The thermal baths are $L_{\text{th}} = 40$ nm long in all the simulations here. In the legends, NHC-τ stands for Nosé-Hoover chain and Lan-τ stands for Langevin.

3.3.3. Temperature profile. To better understand the results above, we plot the detailed temperature profiles in the thermal baths as well as in the middle of the system with different coupling constants τ in Fig. 3.5. Obviously, the Langevin thermostat gives much better temperature control than the Nosé-Hoover chain thermostat. When $\tau \leq 0.5$ ps, the temperatures in the thermal baths under the action of the Langevin thermostat are close to the target values. In contrast, the Nosé-Hoover chain thermostat cannot maintain a constant temperature in the thermal baths for any value of τ. The temperatures close to the fixed boundaries overshoot the target source temperature or undershoot the target sink temperature. The reason is that Nosé-Hoover is a "global" thermostat, i.e. it rescales the velocities of all the particles by the same amount at every MD step and it can
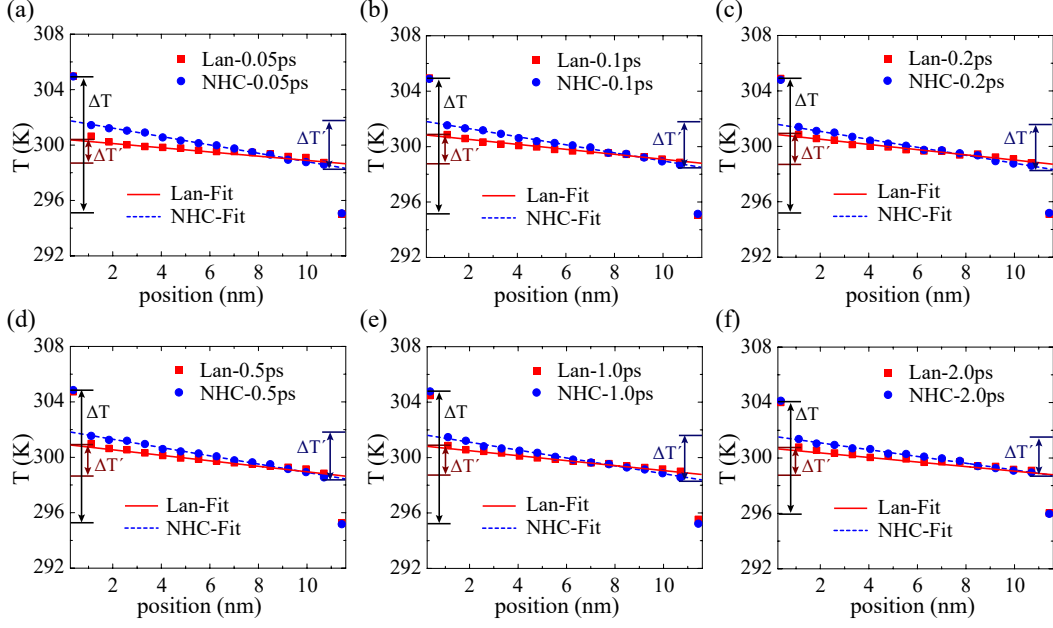
FIGURE 3.6. The temperature profiles from Fig. 3.5, but with the thermal baths being treated as single points with zero length and the middle part of the system expanded in scale. From (a) to (f), the time parameter τ in both thermostatting methods increases from 0.05 ps to 2 ps.

guarantee only that the average kinetic temperature of the thermostatted region is the target one. In contrast Langevin is "local" and it ensures that the whole thermostatted region is at the same temperature, as long as a strong coupling (small τ) is enforced. The use of Nosé-Hoover or any other global thermostat in NEMD results in an effective temperature difference that is larger than that calculated from the average temperatures in the thermal baths and an overestimated thermal conductance as shown in Fig. 3.3.

Let us now focus on the temperature profile in the middle of the system (the $L = 10$ nm part). To this end, we represent the thermal baths as single points with the average temperatures within them; see Fig. 3.6. We can see that there are abrupt temperature jumps between the thermal baths and the system in the middle. Previously, it has been frequently argued that one should apply Fourier's law to the linear region of the temperature profile only. This motivates to fit the middle part of the temperature profile using a linear function and extract a temperature gradient $|\nabla T'| = \Delta T'/L$, where $\Delta T'$ (c.f. Fig. 3.6) is the temperature difference as determined by the interception between the fitted line for the middle part of the temperature profile and the vertical

36

lines at the source and sink. The (effective) thermal conductivity for the system with length L is then calculated as

$$(3.27) \qquad k'(L) = \frac{Q}{S(\Delta T'/L)}.$$

According to the relationship between the conductivity and conductance given in Eq. (3.3), this amounts to using the temperature difference $\Delta T'$ to calculate the thermal conductance:

$$(3.28) \qquad G'(L) = \frac{Q}{S\Delta T'}.$$
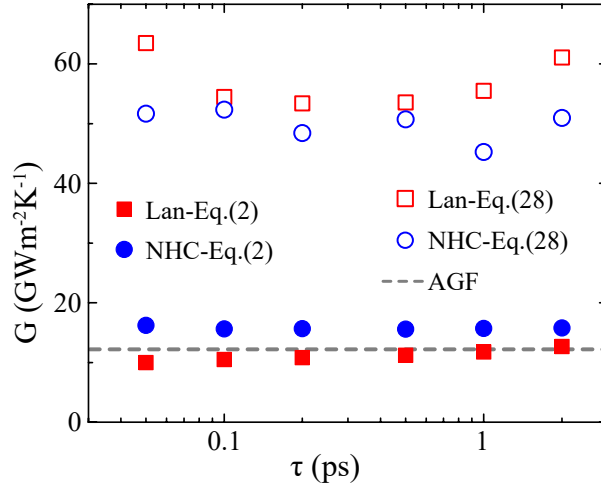
FIGURE 3.7. Total thermal conductance (per unit area) as a function of the relaxation time in the thermostating methods, obtained by using Eq. (3.2) or Eq. (3.28). The reference conductance value from AGF is represented as the dashed line.

Figure 3.7 shows the total thermal conductance (integrated over the frequency) values obtained by using Eqs. (3.2) and (3.28) and different thermostatting methods. When Eq. (3.2) is used, the thermal conductance obtained with both thermostatting methods are relatively close to the AGF value, while the underestimation using the Langevin thermostat is due to the phonon-phonon scattering for the highest-frequency phonons, and the overestimation using the NHC thermostat is due to the nonuniform temperature in the source and sink regions. In contrast, using Eq. (3.28), the obtained thermal conductance is several times higher than the AGF value, for both thermostatting methods. We thus reach an important conclusion in this study: *Eqs. (3.27) and (3.28) may give incorrect (overestimated) results and should not be used in the (quasi)-ballistic*

regime. The correct way is to calculate the thermal conductance using Eqs. (3.2), taking ΔT as the temperature difference between the averaged temperatures in the source and sink. Correspondingly, the (effective) thermal conductivity should be calculated using Eq. (3.4), as we will discuss in Sec. 3.3.4.

3.3.4. Comparison between NEMD and HNEMD in the ballistic-to-diffusive regime

. We now move from the ballistic regime to the ballistic-to-diffusive regime. To this end, we consider systems with different lengths: $L = 25$, 50, 100, 200, 500, 1000, and 2000 nm. Other simulation parameters are fixed: $W = 10$ nm, $\tau = 0.2$ ps, $L_{\text{th}} = 40$ nm.
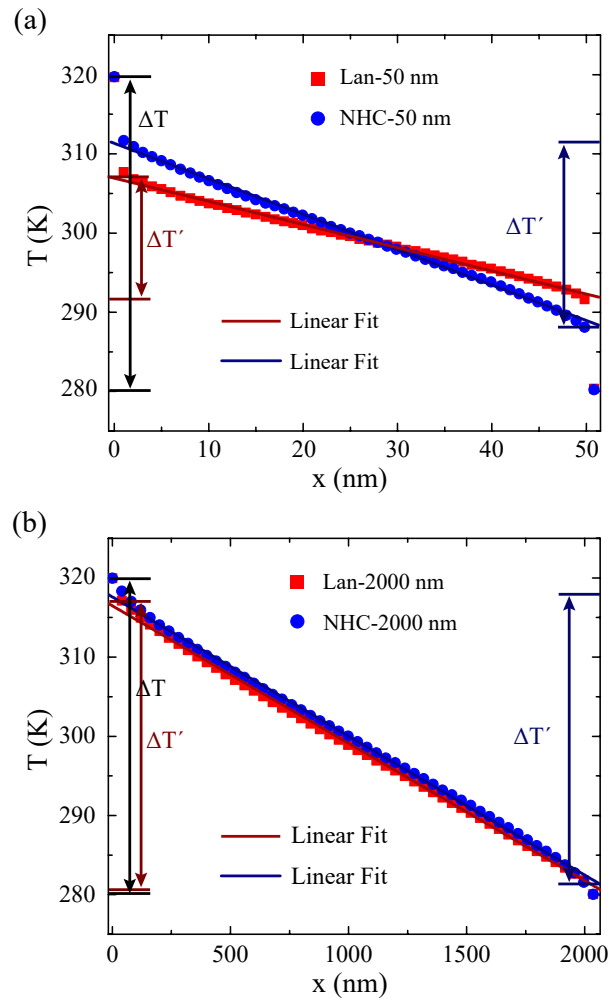
FIGURE 3.8. Temperature profile in graphene sheets with two different lengths obtained by using the Langevin or the Nosé-Hoover chain thermostat: (a) $L = 50$ and (b) 2000 nm.

38
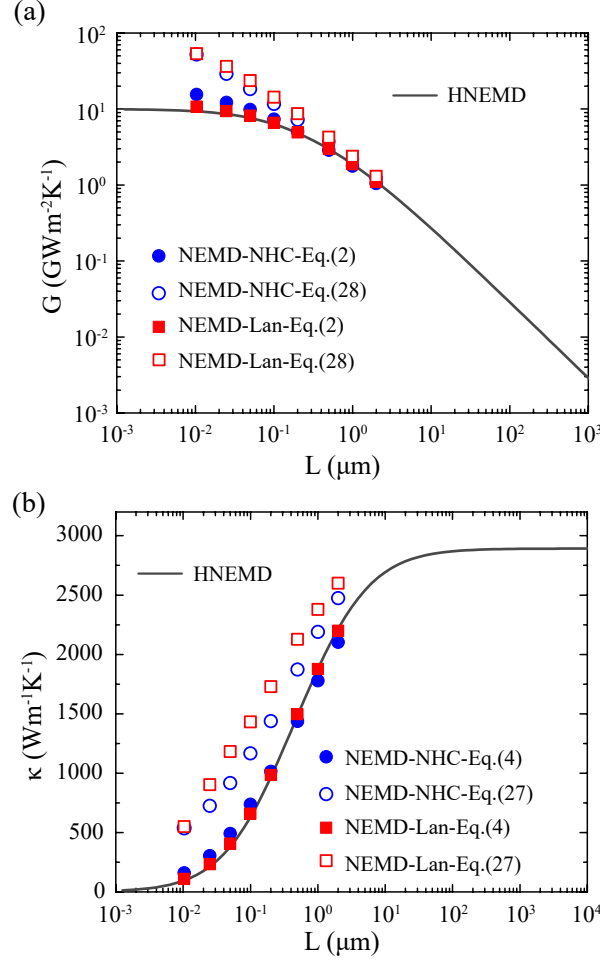
FIGURE 3.9. (a) Thermal conductance and (b) thermal conductivity of graphene sheets as a function of system length from HNEMD and NEMD simulations. In the NEMD simulations, the conductance is calculated by using either Eq. (3.28) or Eq. (3.2), and the conductivity is calculated by using either Eq. (3.27) or Eq. (3.4).

Figure 3.8 shows the temperature profiles for two different system lengths obtained by using the Langevin or the Nosé-Hoover chain thermostat. The difference between the two definitions of temperature difference, ΔT and $\Delta T'$, decreases with increasing L, which is still significant when $L = 50$ nm, but becomes much smaller when $L = 2000$ nm. Due to this difference, the conductance as calculated from Eq. (3.2) and that from Eq. (3.28) are different, as can be seen from Fig. 3.9(a). From the comparison between the NEMD and AGF results in Sec. 3.3.3, we know that Eq. (3.28) is wrong in the ballistic regime. To show that the corresponding expression for thermal conductivity
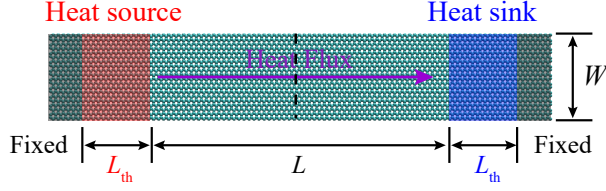
FIGURE 3.10. Temperature profiles in graphene sheets with four different lengths ($L = 10$, 100, 1000, and 10000 nm) obtained by analytically solving a gray 1D BTE. The x axis is the normalized position. The two boundaries are assumed to be at constant temperatures of 305 K and 295 K, respectively. Inset: a schematic illustration of the simulation domain and the thermalizing boundaries.

Eq. (3.27) is also wrong away from the ballistic regime, we convert the conductance in Fig. 3.9(a) into the conductivity as shown in Fig. 3.9(b) using Eq. (3.3).

There is a very efficient way to calculate the length-dependent thermal conductivity in the ballistic-to-diffusive regime based on the HNEMD-based spectral decomposition method developed recently [88]. In this method, one can calculate the spectral thermal conductivity $\kappa(\omega)$ using Eq. (3.26). Then one can obtain the spectral phonon mean free path $\lambda(\omega) = \kappa(\omega)/G(\omega)$, from which one can calculate the length-dependent thermal conductivity as [88]:

$$(3.29) \qquad \kappa(L) = \int_0^\infty \frac{d\omega}{2\pi} \frac{\kappa(\omega)}{1 + \lambda(\omega)/L}.$$

The length-dependent thermal conductivity calculated using this method as well as the corresponding thermal conductance [using Eq. (3.3)] are shown as the solid lines in Fig. 3.9. One can see that the HNEMD results agree well with the NEMD values obtained by using Eqs. (3.2) and (3.4). The Langevin thermostat gives better agreement with the HNEMD results, but the difference between the results from the two thermostatting methods are quite small. The NEMD results obtained by using Eqs. (3.28) and (3.27), on the other hand, deviate from the HNEMD results significantly. The relative errors caused by using Eqs. (3.28) and (3.27) decrease with increasing system length L. If one focuses on the diffusive regime with relatively long systems, using Eq. (3.27) will not result in large errors. This is why previous works [84, 87] using Eq. (3.27) can get agreement between NEMD and other methods in the diffusive regime, using either a linear [115] or a nonlinear [116] extrapolation relation between $1/\kappa(L)$ and $1/L$. However, when L is relatively short (compared to

the average phonon mean free path), using Eq. (3.27) in NEMD simulations will result in large errors.

3.3.5. Relation to the Boltzmann transport equation . The temperature drop between the thermal baths and the middle system is not an artifact of NEMD simulations, as it has also been observed in Boltzmann transport equation (BTE) calculations [80]. To give a simple demonstration of such an effect, we analytically solved the gray 1D BTE for graphene, assuming an average phonon mean free path of 800 nm [79, 117]. To be consistent with the NEMD (with the Langevin thermostat) and AGF simulations, the left and right boundaries are assumed to be at constant temperatures of 305 K and 295 K, respectively.

The temperature profiles for different domain lengths L are shown in Fig. 3.10. Note that in BTE the constant temperature (or thermalizing) boundary condition is implemented in the way that all the outgoing phonons leave the boundary unaffected, while all the incoming phonons have an intensity corresponding to equilibrium distribution at the given temperature [118], as schematically shown in the inset of Fig. 3.10. Such an implementation is equivalent to having two boundaries in contact with infinitely large external thermal baths, and therefore is consistent with the Langevin thermostat as implemented in our NEMD simulations and also the AGF calculations. The temperature discontinuity is straightforward in the BTE picture. For example, in the ballistic limit, since phonons are not thermalized in the middle region, the phonons traveling from left to right have the same energy as the left boundary (305 K), while the phonons traveling from right to left have the same energy as the right boundary (295 K). Under such a non-equilibrium condition, the "effective" temperature in the simulation domain is the average temperature of the two boundaries. Therefore, there is a temperature discontinuity at the boundary. As the system length increases, the phonons within the domain experience stronger phonon-phonon scatterings, so that the discontinuity gradually decreases and eventually diminishes. This is similar to what has been demonstrated in Fig. 3.8. Note that for BTE simulation, it is well known that the conductance in this case should be calculated using the temperature difference between the boundaries [119] instead of that in the middle region. Therefore, it further confirms that the conductance and conductivity should be calculated using Eq. (3.2) and Eq. (3.4), instead of Eq. (3.28) and Eq. (3.27).

Note that here we have only considered a simplified gray BTE model to demonstrate that the temperature profiles in BTE calculations are qualitatively similar to those in NEMD simulations. Gu *et al.* [120] have recently performed BTE calculations with a full iterative scheme, considering both three- and four-phonon scattering processes as well as boundary scatterings in graphene sheets. In such calculations, one can directly obtain length dependent thermal conductivity. They found that good agreement between NEMD and BTE regarding the length-dependence of thermal conductivity can only be obtained if Eq. (3.4) is used to compute the thermal conductivity in NEMD simulations.

3.3.6. Thermal rectification in asymmetric graphene-based systems. The discovery of thermal rectification in low-dimensional non-linear lattice models [24,25] fostered significant efforts to identify efficient thermal diodes [26,27,28], which would lay the cornerstone of nanophononic circuitry [23,49]. In this context NEMD has been extensively used to probe thermal rectification in asymmetric graphene-based nanodevices, including branched nanoribbons, triangular patches and multilayer junctions [121,122,123,124,125]. Using the definition of thermal conductance in Eq. (3.2), the rectification factor is defined in terms of the difference between high and low thermal conductances G_H and G_L obtained by swapping the temperature bias of the thermal diode:

$$(3.30) \qquad \eta = \frac{G_H - G_L}{G_L} \times 100\%.$$

$G_{H/L}$ may be replaced by the heat currents $J_{H/L}$, provided that the temperature difference between the thermal reservoirs remains the same when the temperature bias is inverted. The above mentioned simulation works predict extremely high η, up to 350%, for carbon-based devices, but experimental measurements show much smaller thermal rectification, if any at all [65,124,126].

Here we perform NEMD simulations of thermal rectification in both large trapezoid (LT) and small trapezoid (ST) monolayer graphene patches, where the large trapezoid compares to the smallest trapezoid studied in Ref. [124], which was reported to have large rectification, and in multilayer graphene junctions: bilayer to monolayer (BTM), trilayer to monolayer (TTM) and quadlayer to monolayer (QTM), where the multilayers are of the same geometry as those in [123]. All the layers were thermalized in order to compare with the previous numerical studies [123]. In all our thermal rectification simulations, we fixed two layers of atoms at the two ends of the sample
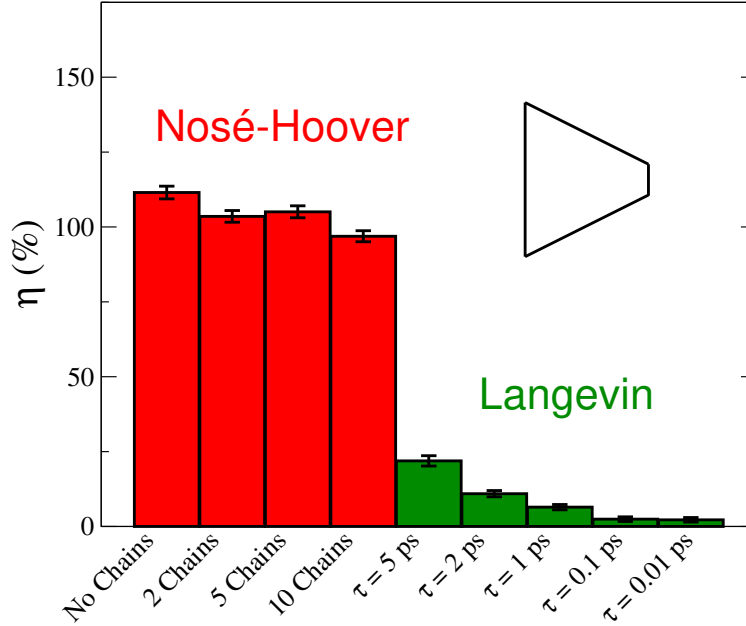
FIGURE 3.11. Comparison of the thermal rectification of the large trapezoid (LT) monolayer graphene obtained using either the Nosé-Hoover thermostat with different number of chains ($\tau = 0.1$ ps) or Langevin thermostat with different relaxation times.

in the transport direction to achieve the fixed boundary conditions. Next to the two fixed layers, atoms within a length of L_{th} (1.7 nm for LT, 0.5 nm for ST, and 0.8 nm for other systems) were coupled to a hot and a cold thermal bath, respectively. We obtain the rectification factor of these nanodevices by computing the heat current in two separate NEMD simulations for each system, in which the hot and cold reservoirs are swapped, so to probe the high-conductance and the low-conductance conditions. We compare the rectification factor obtained using either Nosé-Hoover, Nosé-Hoover chain, or Langevin dynamics to set the temperatures at 350 and 250 K for the hot and cold thermal reservoirs. After equilibration at 300 K, NEMD simulations are run for 4 ns (8 million time steps), and the thermal conductance is computed from the last 2 ns of these runs.

We first test the effect of using different types of thermostats on the rectification factor of the LT graphene patch with 21.6 nm and 2 nm bases and height of 17 nm. This system is made of 8049 atoms and former NEMD simulations using the Nosé-Hoover thermostat predicted a rectification factor $\sim 95\%$ [124]. Our simulations with the standard Nosé-Hoover thermostat with $\tau = 0.1$ ps are in accord with these former results, predicting $\eta = 111(\pm 2)\%$. Adding more degrees of

freedom to the thermostat, using Nosé-Hoover chains does not significantly change the estimate for η, which remains $\geq 100\%$ (Fig. 3.11). However, when Langevin dynamics is employed to fix the temperature of the thermal baths and produce a stationary flux, η is considerably reduced which matches the results of a previous study [**114**]. Furthermore, η depends on the relaxation time used in Eq. (3.16). The smaller the τ, i.e. the stronger the coupling, the lower the rectification factor and its uncertainty. For $\tau \leq 0.1$ ps η can be considered statistically zero. As we have shown in the previous sections the NEMD Langevin dynamics provides more accurate results than Nosé-Hoover chain, and thus we can argue that the LT graphene patch considered here should not exhibit any significant thermal rectification.
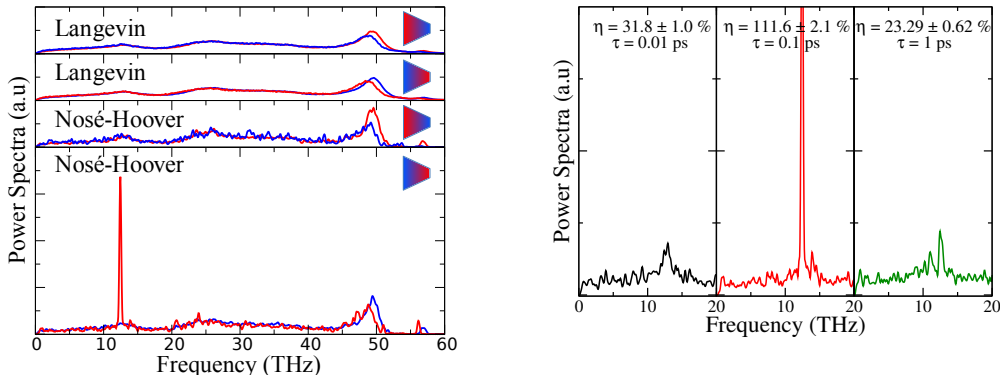
FIGURE 3.12. (a) Power spectra of the thermal baths of the large trapezoid (LT) monolayer graphene system with different heat current biases using a Langevin thermostat with $\tau = 0.1$ ps and a Nosé-Hoover thermostat with $\tau = 0.1$ ps. The small insets show the geometry of the system with cold (blue) and hot (red) baths. (b) Power spectrum of the thermal bath as a function of the Nosé-Hoover thermostat coupling constant τ.

To unravel the origin of the large discrepancy between the two simulation methods, we calculated the power spectrum of the thermal baths in the NEMD simulations of trapezoid graphene at direct and reverse bias conditions (Fig. 3.12a). When the hot bath is on the large base of the trapezoid the hot and cold power spectra overlap, except for the high frequency peak, which does not contribute significantly to heat transport. This condition corresponds to high conductance and the two thermostats give similar results. With reverse bias, however, the hot bath exhibits an extremely intense peak at 12 THz when the Nosé-Hoover thermostat is employed, indicating that vibrational modes at this frequency are artificially overpopulated. The energy accumulated in these

specific modes cannot transfer through the device, leading to low conductance. Such overpopulation of a specific mode is an artifact of the Nosé-Hoover chain thermostat, occurring in non-ergodic system with a small number of degrees of freedom [**127**]. This effect leads to a unbalance between the power pumped by the thermostat into the hot bath and that removed from the cold bath, which should be equal at stationary conditions. With Nosé-Hoover chain these conditions are not achieved over the typical run time of several ns. When Langevin dynamics is used, the coupling parameter τ determines how rapidly stationary conditions with constant flux are attained, with shorter τ providing faster thermalization. We have verified that changing the coupling parameter of the Nosé-Hoover thermostat may alleviate the observed mode overpopulation in the thermal bath, but without completely removing it (Fig. 3.12b). For any coupling time τ tested, between 0.01 ps and 1 ps, thermostatting the heat baths with Nosé-Hoover significantly overestimates the rectification efficiency. Furthermore, we observe that the frequency of the mode that gets overpopulated does not depend on τ, thus indicating that it depends on the chemical and geometrical parameters of the heat bath.
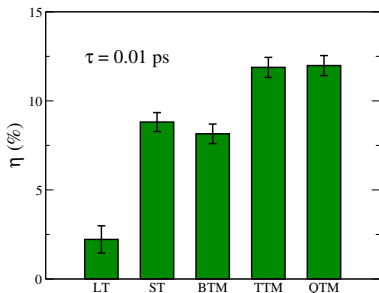
FIGURE 3.13. Rectification factor of large trapezoidal graphene monolayer (LT), small trapezoidal graphene monolayer (ST), and of multilayer graphene junctions, bilayer to monolayer (BTM), trilayer to monolayer (TTM), and quadlayer to monolayer (QTM).

These results suggest that Nosé-Hoover is unsuitable to study thermal rectification, unless one carefully addresses the very long thermalization time. Hence we use Langevin dynamics with $\tau = 0.01$ ps to calculate the rectification factor of the other junctions considered. Results in Fig. 3.13 show that for either trapezoidal or multilayer graphene junctions $\eta < 15\%$, in contrast with the high rectification efficiencies predicted in NEMD simulations carried out using Nosé-Hoover. Whereas

multilayer graphene junctions may attain measurable rectification, all these systems are unsuitable for practical applications as thermal diodes.

3.4. Conclusions

In summary, we have carefully and systematically revisited some critical issues in the frequently used NEMD methods for thermal transport calculations. By comparing with the AGF method in the ballistic regime and the HNEMD method in the ballistic-to-diffusive regime, we found that the nonlinear part of the temperature profile in NEMD simulations should not be excluded in the calculations of the thermal conductivity and conductance. We also found that the Langevin thermostatting method controls the local temperatures better and is more reliable than the Nosé-Hoover (chain) thermostatting method for NEMD simulations. This is particularly important for studying asymmetric nanostructures, for which the Nosé-Hoover thermostat can produce artifacts leading to unphysical thermal rectification. Based on our results, we recommend an intermediate value ($\tau = 0.1 - 1$ ps) for the time parameter in the Langevin thermostat for thermal conductivity calculations and a small value ($\tau \leq 0.1$ ps) for thermal rectification studies, where one usually considers large temperature differences.

Although we have only studied heat conduction in solids, we note that the Langevin approach performs better than the Nosé-Hoover thermostat to carry out NEMD simulations of molecular fluids as well [128]. The differences of using the Nosé-Hoover thermostat and other "global" thermostatting methods, as opposed to "local" thermostats, like Langevin, for NEMD simulations of heat conduction are further studied in Ref. [129].

3.5. Summary of Contribution

I ran NEMD on structurally asymmetric graphene devices. Found that NH thermostats for the local heat bath and sink thermostats can produce artificially high thermal rectification. The artificially high thermal rectification comes from the tendency for deterministic thermostats to excite specific thermal modes. If these specific thermal modes do not relax into efficient heat carriers then they become overpopulated creating an artificially high temperature while the lack of thermal relaxation causes an artificially low thermal flux conductance. When the temperature is artificially high and the flux is artificially low when the current is biased in one direction and there

are no artifacts when the current is reversed, this causes an artificially high thermal rectification. I have shown this by elucidating an overpopulated mode from NH that is non existent for Langevin. Langevin thermostats do not have this problem since they are stochastic and thus lack the capacity to resonate with a specific thermal mode.

Thermal Transport Across Graphene Step Junctions

4.1. Introduction

The emergence of two-dimensional (2D) materials has brought new opportunities to explore fundamental physical properties and to exploit these materials for new applications. [130] As the first isolated 2D material [15, 131, 132] and due to its extraordinary transport properties, [133] graphene has been extensively studied especially for electronic applications. However, the properties of graphene can be altered due to crystal imperfections which appear, for example, during graphene growth by chemical vapor deposition (CVD). One such type are grain boundaries (GBs), [134] i.e. line defects where two graphene grains (of the same thickness) are stitched together. Other defects are graphene junctions (GJs), i.e. the steps between regions with different number of graphene layers, such as monolayer-to-bilayer (1L–2L) junctions.

The properties of GBs are relatively well understood, having been measured electrically, [135] thermally, [136] and mechanically. [137] For example, GBs reduce the overall electrical [135] and thermal conductivity [113, 138] of graphene due to electron and phonon scattering, respectively. However, GJs have only recently attracted more interest with few experimental studies of their properties in electronics, [139] optoelectronics, [140] and as p-n junctions. [141] A theoretical study assigned thermal rectification properties to GJs, [123] however this has not been examined experimentally. Other simulations also showed that heat transfer at GJs is non-trivial, because in the multilayer region different layers may have different temperatures. [142] Knowledge of heat flow across GJs is important not just fundamentally, but also for practical applications in terms of how they modify the overall thermal conductivity of graphene (as GBs do [113, 143]), or where GJs could act as phonon filters. As an example, electronic devices based on graphene and other

---

[0]The work described in this Chapter is reproduced in partial or full form from the following publication:

- M. M. Rojo, et. al. 2D Mater. 2019, 6, 011005. [65].

2D materials often contain GJs, but little is known about how their thermal resistance affects the overall device performance. [**4**, **144**]

Here, we investigate for the first time the temperature dependent heat flow across GJs supported on SiO$_2$ substrates. Our experimental results combined with molecular and lattice dynamics (MD and LD) simulations indicate thermal decoupling between layers caused by a large thermal boundary resistance (TBR). Thus, we establish a microscopic understanding of thermal conduction across GJs and clarify their role in large-area thermal management applications of graphene.

4.2. Methods

4.2.1. Experimental measurements and data analysis. Highly crystalline graphite (carbon > 99.75%) was mechanically exfoliated with $Scotch^{TM}$ tape onto SiO$_2$ (~295 nm) on Si substrate chips of ~1 × 1 cm^2 size. An optical microscope was first used to find large GJ samples where we could perform thermal measurements (supplementary section 1).

Electron-beam (e-beam) lithography (with a first layer of PMMA 495 and a second layer of PMMA 950 spin-coated on the samples at 4000 rpm for 40 s, and baked at 180 °C for 10 min) was used to pattern the heater and sensor on each side of the GJ. Heater and sensor lines are ~200nm wide and ~5 m long. After development, an e-beam evaporator was used to deposit 40 nm of SiO$_2$ followed by 3 nm Ti and 35 nm Pd, forming the heater and sensor lines, electrically isolated from the graphene underneath (supplementary section 1). The separation (L) between heater and sensor lines for 1L–2L and 2L–4L junction samples were L1L–2L = 374 nm and L2L–4L = 395 nm, respectively (figures 1(b) and (d)).

Raman spectroscopy was carried out using a Horiba LabRam instrument with a 532nm laser and 100 × objective with N.A. = 0.9, after all fabrication and other measurements were completed. The GJ region was scanned with 150 nm step size and 160 W laser power. The laser spot diameter obtained by the knife-edge method was<400nm. We analyzed the spectra of several representative locations on both sides of the GJs by removing the baseline and fitting the 2D (also known as G) peak with different Lorentzians (figures 1(c) and (e)). These Raman maps determined the quality of the graphene and number of layers on each side of the GJ (also see supplementary section 2).

49

The samples were wire-bonded into chip carriers and the thermal measurements were carried out in a cryostat at 1.3×10^6 mbar, at temperatures from 50 K to 300 K (supplementary sections 4–7). SEM was used after thermal measurements to examine the location of the heater and sensor on each side of the GJ, as well as to measure the separation and dimensions of the lines (supplementary section 1).

The experimental data were analyzed using finite element modeling (FEM) with COMSOL® Multiphysics (supplementary section 10), to determine the thermal conductance of the GJ and of the various layers and interfaces. These simulations were based on previous measurements on similar samples carried out by a subset of the authors. [145, 146] The uncertainty calculations are also explained in supplementary section 10.

4.2.2. Non-equilibrium molecular dynamics (NEMD). All MD simulations were carried using the LAMMPS package. [109] We used the optimized Tersoff force-field for the in-plane interactions, [64] and a Lennard–Jones (LJ) potential with $= 3.295\,67$ meV and $= 3.55$ Å for the interlayer interactions, according to the OPLS-AA parameterization. [111] Equations of motion were integrated with a time step of 1 fs. The simulated structure had a periodic width of 5 nm and interlayer spacing of 0.335 nm, containing 14736 C atoms in a 25nm long top layer (4896 atoms) and a 50 nm bottom layer (9840 atoms) in the transport direction. Boundary conditions were fixed in the transport direction and periodic in both perpendicular directions. We first equilibrated the system in the canonical ensemble at 300K using the stochastic velocity rescaling algorithm for 0.1 ns (supplementary section 8). [147]

To enable a stationary heat current, the 10% C atoms at the left end of the top layer and 10% atoms at the end of the bottom layer were thermostatted to the target temperatures of 350 and 250 K, respectively, using Langevin thermostats with a 0.05ps relaxation time. We have tested different coupling constants and verified that a weaker coupling, e.g. 1 ps, is insufficient for the thermal baths to reach the target temperatures. [114] The first two rows of C atoms in the top and bottom sheets and the last two rows of C atoms in the bottom sheet were constrained at fixed positions, and the system was allowed to run for a total of 40 ns. The temperature profile was grouped into 100 bins along the transport direction, sampled every 10th step, the total average was computed every 1000 steps and the temperature was calculated from the kinetic energy. The power

supplied or subtracted by the hot or cold Langevin thermal baths is averaged over time at stationary conditions to give the steady-state heat flux. The temperature profiles of the converged steady-state are averaged and plotted, and the difference in bath temperature gives the total temperature differential (supplementary section 8).

4.2.3. LD calculations. We compute thermal boundary conductance in the quantum regime for GJs models using LD and the ESKM. [**78**, **148**] We consider both suspended and supported junctions. The interatomic potentials used for LD calculations were the same as in the NEMD simulations for the suspended device. The interatomic interactions of the quartz substrate in the supported device are modeled with the potential by van Beest et al. [**149**] The interactions between the graphene layers and the substrate are modeled with a LJ potential with interaction cut-offs set to 8 Å. All models had a periodic width of 4.984 nm and varying lengths. The overlap lengths for the suspended GJs were 14, 17, 37, 62, 92, and 186 nm. The overlap lengths for the supported GJs were 5.1, 22.4, 39.7, 56.9, 91.4 and 181.3 nm (supplementary section 9).

4.3. Experimental results

Figure 4.1(a) illustrates the schematic of the device structure we used to measure the thermal conductance across GJs. Graphene used in this study (see Methods) is mechanically exfoliated onto a SiO_2/ Si substrate (supplementary section 1 (stacks.iop.org/TDM/6/011005/mmedia)) and step junctions were identified by optical microscopy, atomic force microscopy (AFM), Raman spectroscopy (see Methods) and were finally confirmed by scanning electron microscopy (SEM) after all measurements were completed. During thermal measurements two parallel metal lines were used as the heater and thermometer, interchangeably. [**145**, **150**] A thin layer of SiO_2 (~40 nm, electron-beam evaporated, see Methods) underneath the metal lines provided electrical isolation from the graphene. Figures 1(b) and (d) show SEM images of the two devices measured, which correspond to 1L–2L and 2L–4L (bilayer to four-layer) GJs, respectively. Figures 1(c) and (e) show Raman spectra obtained on each side of the GJ, determining the number of graphene layers. The Raman spectra do not show discernible D peaks even after patterning the metal lines, confirming relatively defect-free, crystalline graphene regions (supplementary section 2).

51

We performed heat flow measurements from 50K to 300K on these GJ samples and on similar control samples without graphene. We also measured heat flow across the GJs in both directions by swapping the heater and sensor, to test for possible asymmetry in the heat flow as a consequence of phonon scattering at the junction, which would lead to thermal rectification for large temperature differentials. [123] The measurements are performed as follows. Current is forced into a metal line, which acts as a heater, while both metal lines are used to sense temperature, setting up a temperature gradient across the GJ. The metal lines are thermoresistive elements, which allow us to convert measured changes of electrical resistance into variation of the temperature of the sensor, T_S, and heater, T_H, as a function of the heater power PH (supplementary section 4). We calibrated both metal lines for each sample by monitoring the resistance over a slightly wider temperature range, from 40 K to 310 K, to determine the temperature coefficient of resistance (TCR) and quantify temperature variations (supplementary sections 6 and 7). Once the temperature difference between the metal lines is known as a function of heater power, the thermal conductance across the junction is obtained by processing the experimental data using a three dimensional (3D) finite element model (FEM) [145, 146] (see Methods). In this simulation, the graphene channel region between heater and sensor is treated with an effective thickness h = 0.34n nm, where n = 2 in both devices because most of the two channels are covered by 2L graphene (see arrows in figures 1(b) and (d)). In other words, the FEM fits the graphene channel with an effective thermal conductivity, k, between heater and sensor. The effective channel thermal conductance is G = kh(W/L), where W and L are the graphene channel width and length.

The FEM shown in figure 4.1(f) accurately replicates the experimental setup taking into account: (i) all geometric dimensions of the metal lines, determined using SEM images (supplementary section 1); (ii) the thickness of the SiO_2 under the graphene from ellipsometry (supplementary section 3) and its temperature-dependent thermal conductivity from measurements of the control sample (supplementary section 5); (iii) the Si thermal conductivity for Si wafers with the same doping density [151] (supplementary section 3). The FEM also includes the effect of TBR at Si–SiO_2 interfaces [145] from the control sample, graphene–SiO_2 [152] and SiO_2-metal [153] interfaces, based on previous measurements of similar samples. [145] Figure 4.1(f) shows the simulated temperature distribution with current applied through the heater for the 1L–2L junction device.

The thermal conductivity k of the graphene channel is varied in the simulation until T_S and T_H versus P_H modeling results match well with the experimental data.

We also measured a control sample without graphene in the channel to validate our method and to obtain the thermal properties of the parallel heat flow path through the contacts,the supporting SiO_2,the SiO_2–Si interface and the Si substrate (supplementary section 5). These thermal properties obtained after processing the experimental data with the FEM show good agreement with well-known data from literature [145, 154, 155] over the full temperature range. Consequently, these data were used as inputs for the FEM simulation of the GJ structures.

Figure 4.2 shows the experimental heater temperature rise (in red) and sensor temperature rise (in blue) normalized by the heater power, $\Delta T/P_H$, as a function of temperature obtained for the two junctions studied, 1L–2L and 2L–4L. The heat flow was studied in both directions across the GJ to account for possible thermal rectification effects. The uncertainty of $\Delta T/P_H$ is ~0.5%–1%, which agrees well with our previous experiments that used similar metal lines. [145]

Figures 3(a) and (b) show the schematic of the 1L– 2L and 2L–4L GJ samples. The rectangular colored sections on top illustrate the thermal conductivities, i.e. 1L (k_1), 2L (k_2) and 4L (k_4) for non-junction regions, while 1L–2L (k_{12}) and 2L–4L (k_{24}) represent the GJ channel region.

These are used by the FEM to process the raw experimental data from figure 4.2, yielding the effective thermal conductivities shown in figures 3(c)– (f). While the effective thermal conductivity of the GJ channel (k_{12} and k_{24}) is determined from the temperature gradient between heater and sensor, the thermal conductivity of 1L, 2L and 4L is mainly determined from temperature variations only at the heater surroundings. Although not the main topic of this study, these supported 2L and 4L graphene thermal conductivity estimates are among the first of their kind (others being discussed below).

Figures 3(c) and (d) display the extracted thermal conductivity of the 1L, 2L and 4L graphene regions, as well as the effective thermal conductivity of the 1L–2L and 2L–4L junctions, in both directions of heat flow. The 1L, 2L and 4L thermal conductivities show similar values over the entire range of temperature.

Their room temperature values are ~500 $Wm^{-1}K^{-1}$ for 1L, ~400 $Wm^{-1}K^{-1}$ for 2L, and ~450 $Wm^{-1}K^{-1}$ for 4L graphene, respectively. These are consistent with earlier measurements by Seol

53
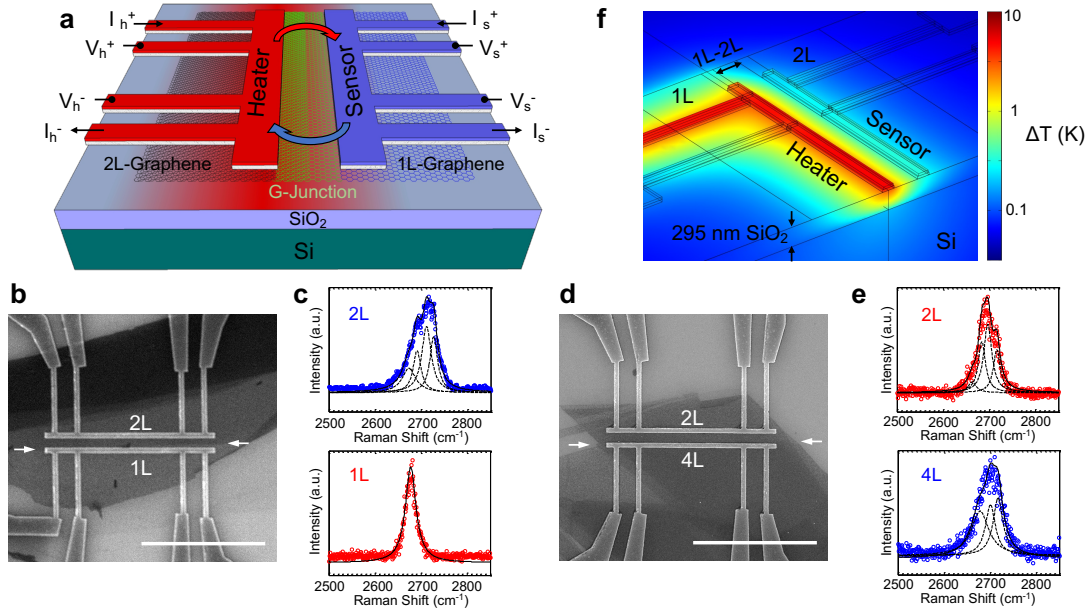
FIGURE 4.1. (a) Device layout for thermal conductance measurements across 1L–2L GJ. Two metal lines with ~400 nm separation were formed with the GJ between them. A thin SiO$_2$ layer under the metal lines provides electrical isolation and thermal contact with the graphene beneath. One of the lines is used as heater while the other one as sensor. The heater and sensor can be reversed to measure the heat flow in both directions. (b), (d) and (c), (e) show scanning electron microscopy (SEM) images and Raman spectra of the 1L–2L and 2L–4L GJs, respectively. GJs are indicated by arrows and all scale bars are 5 m. The dashed lines represent Lorentzian fits to the 2D (also known as G) peak of the Raman spectra. (f) Three-dimensional (3D) simulation of the experimental structure, showing temperature distribution with current applied through the heater.

et al, [156] Sadeghi et al, [157] and by Jang et al [150] who found the thermal conductivity of SiO$_2$-supported 1L, 2L and 4L graphene were ~580, ~600 and ~480 $Wm^{-1}K^{-1}$ at room temperature, respectively. To obtain the various thermal conductivities from the FEM fitting, we used the same TBR between graphene and SiO$_2$ for all layers, following Chen et al, [152] but there may be small differences in the TBR that could be behind this small variation. However, our results are in good
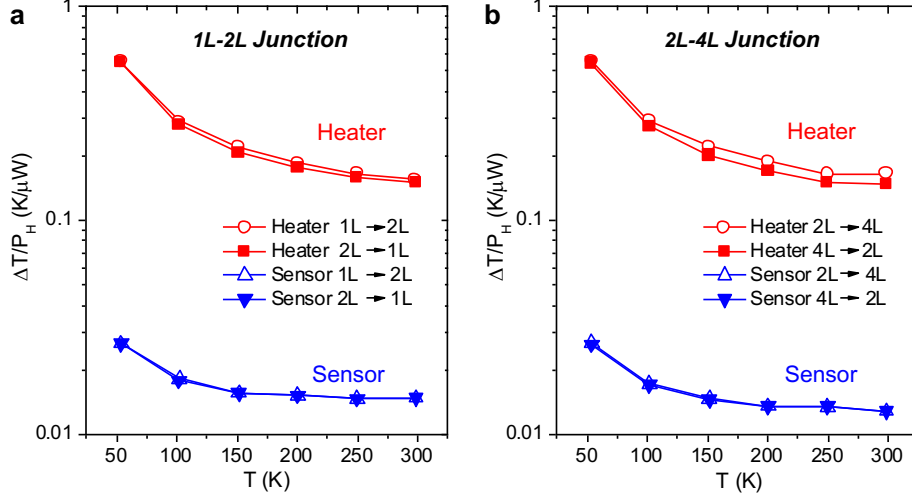
FIGURE 4.2. Experimental measurements of temperature rise in the heater and sensor divided by heater power, $\Delta\text{T}/P_H$, as a function of temperature for (a) the 1L–2L and (b) 2L–4L GJ. Heat flow was measured in both directions, from 1L $\to$ 2L versus 2L $\to$ 1L, and from 2L $\to$ 4L versus 4L $\to$ 2L, without observing thermal rectification. The uncertainty of these data is smaller than the symbol size.

agreement with values reported by Sadeghi et al, [**157**] which show that the thermal conductivity of SiO$_2$-supported graphene few-layers remains very similar.

In comparison, figures 3(c) and (d) show that the effective thermal conductivity in the GJ regions, i.e. k_{12} and k_{24}, is lower than in the graphene layers, i.e. k_1, k_2 and k_4. This difference becomes more evident as the temperature reduces from 300 K to 50 K. Figures 3(e) and (f) show the effective thermal conductance of the GJ regions, calculated by dividing the thermal conductivity with the metal line separation (see Methods). The thermal conductance for 1L–2L varies from $4.8\pm1.1\times10^7$ $Wm^{-2}K^{-1}$ to $9.1\pm1.2\times10^8$ $Wm^{-2}K^{-1}$ at 50 K and 300 K respectively, while for 2L–4L it varies from $6.1 \pm 1.3 \times 10^7$ $Wm^{-2}K^{-1}$ to $7.7 \pm 1.2 \times 10^8$ $Wm^{-2}K^{-1}$ at 50K and
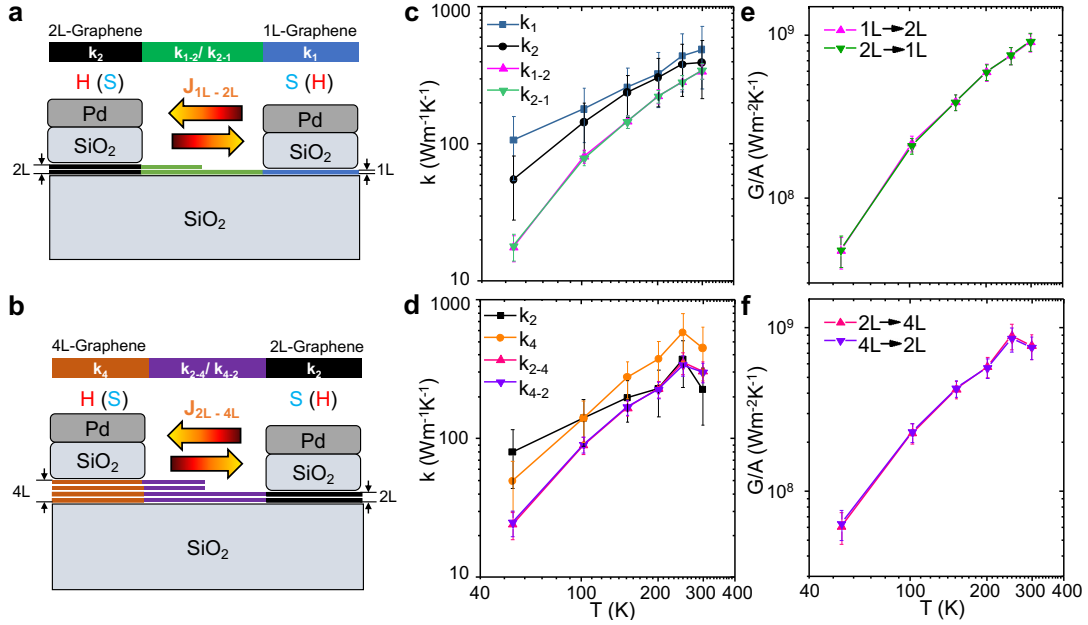
FIGURE 4.3. (a) and (b) Schematic cross-sections of 1L–2L and 2L–4L GJ experiments, respectively. The graphene layers and junctions are colored corresponding to different thermal conductivity regions, determined after processing the experimental data (figure2) with the FEM. (c) and (d) Thermal conductivity obtained for each region of graphene (1L, 2L and 4L) and for the 1L–2L and 2L–4L junctions for both heat flow directions. (e) and (f) Thermal conductance per unit area, i.e. thickness times width (A = hW), obtained at the junction. The results show no thermal rectification effect within the experimental error bars.

300K respectively. Bae et al [145] explained that as we shorten the length of a graphene channel, quasi-ballistic phonon transport effects reduce its thermal conductivity, because the longest phonon mean free paths become limited by the length of the channel. In other words, the graphene thermal conductivity is length-dependent in this sub-micron regime. The thermal conductivity of our GJ samples is consistent with values reported by Bae et al [145] for length-dependent graphene without junctions. Additionally, that the thermal conductance of the 1L–2L and 2L–4L channels is almost

identical for both heat flow directions, i.e. $k_{12} \approx k_{21}$ and $k_{24} \approx k_{42}$, indicates no measurable asymmetry in the heat flow or thermal rectification effects on supported graphene at the junction.

4.4. Molecular and Lattice dynamic simulations and discussion

To explain the measured thermal conductance of the GJs in both heat flow directions we consider two possible scenarios. The first scenario consists of thermal decoupling between the top and bottom layers of graphene, which could be attributed to the presence of a large TBR between layers. The thermal decoupling between layers would cause the heat to flow only through one layer, i.e. the bottom one, which would result in similar conductance values as the work of Bae et al. [145] Moreover, the large TBR between layers would make phonon scattering at the junction negligible, which would support the idea of a non-asymmetry or thermal rectification effect. The second possible scenario would be a perfect coupling between the top and bottom graphene layers, i.e. very small TBR between layers, which would explain the similarity of the GJs thermal conductance with those shown by Bae et al. [145]

However, under these circumstances, we would expect the junction to scatter phonons more efficiently, which might induce some thermal asymmetry across the junction.

To quantitatively understand the phonon physics at the GJ, we performed atomistic molecular dynamics (MD) simulations and LD calculations (see Methods). First, we evaluate a suspended 1L–2L junction by non-equilibrium molecular dynamics (NEMD) simulations as shown in figure 4.4. [95] The length of the MD models is up to 200 nm, which, although about half the size of the experimental device, still captures its essential physical properties. To produce a stationary heat current (J), the ends of the device are kept at 350 and 250K (see Methods), respectively, by two Langevin thermostats. If the system displayed thermal rectification its thermal conductance, computed as G = J/ΔT, would differ if the heat current went from 1L $\rightarrow$ 2L or from 2L $\rightarrow$ 1L. Setting up the NEMD simulations we have two options to treat the bilayer side of the GJ: we can either apply the thermostat to both layers, as in, [142] or treat only the top layer as a thermal bath. In the first case we find that the thermal conductance is near that of a single graphene layer, too large compared to the experiments (supplementary section 8). Thus, we focus our analysis on the second case. In fact, NEMD simulations show the thermal conductance of the device is the
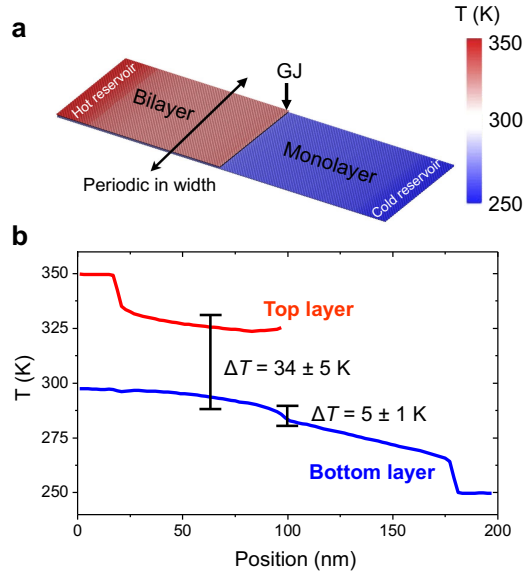
FIGURE 4.4. Representation of the molecular model of a suspended 1L–2L GJ. Atoms are color-coded according to the temperature at stationary non-equilibrium conditions. The graph shows the temperature profile in the non-equilibrium MD simulation in which the bilayer is heated to 350 K and the monolayer is cooled to 250 K. The two layers are thermally decoupled, with a major temperature difference (ΔT ~34 K) between them; a much smaller temperature jump (ΔT ~5 K) is seen in the bottom layer at the junction.

same, within the statistical uncertainty, regardless of the direction of the heat current. Hence, our simulations also confirm that this system does not display thermal rectification.

An analysis of the temperature profile at stationary conditions (figure 4.4) shows that the top and bottom layers of the junction are thermally decoupled, and the main source of TBR is not the step at the junction, but rather the weak coupling between the two stacked graphene layers. Such weak coupling causes a larger temperature difference (ΔT ~34 K) between the top and bottom layer of the device, whereas the temperature discontinuity at the step of the junction is only ~5 K. Hence the main resistive process occurs at the interface between the overlapping layers, which

is symmetric, thus explaining why no thermal asymmetry or rectification occurs. Even with a very large temperature difference at the two ends of the device ($\Delta T \sim 450$ K), thermal rectification remains negligible (supplementary section 8).

Our experiments and simulations appear at odds with the NEMD results of Zhong et al. [123] In this work, the system is set up such that there is no thermal decoupling between layers in the thermal reservoir, and this effect is not probed in the non-thermostated junction. Hence these former simulations suggest an asymmetric phonon scattering at the junction that depends on the heat flow direction (thermal rectification effect). By comparing our simulations with theirs, we conclude that an apparent thermal rectification could be observed by sampling the system at non-stationary conditions, stemming from poor equilibration of the thermal baths. This is especially a problem for poorly ergodic systems such as graphene and carbon nanotubes. [114]

While NEMD sheds light on the microscopic details of heat transport at the GJ, it does not allow a quantitative estimate of the conductance that can be compared to experiments. In fact, due to the classical nature of MD simulations, quantum effects are not taken into account. Considering that the Debye temperature of graphene exceeds 2000K and experiments are carried out at room temperature and below, quantum effects are expected to play a major role in determining the conductance. Thus, we also calculated the thermal conductance of the 1L–2L junction, treated as an open system, using the elastic scattering kernel method (ESKM). [78] ESKM is an LD approach equivalent to Green's functions, [47] implemented in a scalable code that allows us to compute coherent phonon transport in systems of up to 106 atoms. [148] Thus, we could calculate the thermal conductance of suspended and SiO_2-supported GJs with the same overlap length as in the experiments. LD calculations give the phonon transmission function $\mathcal{T}()$ for an open system with semi-infinite thermal reservoirs, resolved by mode frequency and polarization. The thermal conductance is then computed by the Landauer formula, [46] integrating $\mathcal{T}()$ overall frequencies:

$$(4.1) \qquad G = \frac{1}{2\pi} \int_0^{\omega_{max}} d\omega \hbar \omega \mathcal{T}(\omega) \frac{\partial f_{BE}(\omega, T)}{\partial T}$$

where T is the temperature and f_{BE} is the Bose–Einstein distribution function, accounting for the quantum population of phonons. In this approach we neglect anharmonic phonon-phonon scattering. This assumption is justified a posteriori by comparing the conductance of a suspended

59

device with overlap length of 25 nm, computed by NEMD, $G = 1.16 \pm 0.09 \times 10^9 \ Wm^{-2}K^{-1}$, with that obtained by LD using a classical phonon distribution function, $G = 0.92 \times 10^9 \ Wm^{-2}K^{-1}$. A ~20% difference between LD and NEMD calculations of G is acceptable, as it may stem not only from neglecting anharmonic scattering in LD, but also from the finite T in NEMD.

Figure 4.5 displays the thermal conductance of the 1L–2L GJ calculated by LD as a function of the length of the bilayer part (a) and of the temperature (b), compared to experimental data. To assess the effect of the substrate in the experimental device, we consider models of GJ both suspended and supported on a SiO_2 substrate. The geometry of the suspended model is the same as the one used in NEMD (figure 4.4). G is independent of the length of the monolayer part of the device, as in this approach it conducts heat ballistically. G is normalized by the width of the GJ and by a nominal thickness of the bilayer part of 0.67 nm, which is the same convention used in processing the experimental data. The agreement between modeling and experiments is excellent at low temperature in figure 4.5. In the experimental device at higher temperature, heat transfer is still mainly dictated by the TBR between the two graphene layers, but the thermal bath also affects the bottom layer in the bilayer part of the device, thus making the conductance larger than that predicted by the model. The thermal conductance of the device increases with the interlayer overlapping surface area, which is determined by the length of the bilayer part (figure 4.5(a)). However, G does not grow linearly with the overlap surface and tends to saturate with the overlapping length. The conductance limit of this device is indeed dictated by the ballistic limit of a single graphene sheet. [158]

The interaction with the SiO_2 substrate reduces the overall conductance of the device by about 30% at room temperature. In order to achieve quantitative agreement between theory and experiments, it is important to consider the conductance reduction in the model for supported structures. The temperature dependence of the GJ thermal conductance can be almost entirely ascribed to the quantum population of the phonon modes. In fact, figure 4.5(b) shows that theory and experiments display an excellent agreement at low temperature, while systematic deviations appear at T > 200 K, allowing us to pinpoint the effect of anharmonic scattering, which is not taken into account in the calculations. Resolving the transmission function by mode polarization shows that only out-of-plane modes contribute to heat transport across the inter- layer junction, consistent with

60

another recent study (supplementary section 9). [**159**] We also observe that the interaction with the substrate causes an offset of the out-of-plane modes of the bottom graphene layer with respect to those of the top layer, thus hampering the transmission function even further and reducing the conductance of the device.

4.5. Conclusions

In conclusion, we have experimentally measured, for the first time, the temperature-dependent heat flow across GJs, i.e. 1L–2L and 2L–4L GJs, supported on SiO_2 substrates. MD and LD simulations were used to analyze the GJ thermal transport. The simulations show that the top and bottom layers of the junction are only weakly thermally coupled, and the main source of TBR is not the step at the junction, but rather the weak coupling between the two layers in bilayer graphene. The interaction with the substrate was observed to have a significant effect to achieve good agreement between the theory and experiments. In fact, the values obtained for the experimental and theoretical thermal conductance of supported GJs showed excellent agreement at low temperature (T < 200 K), whose dependence can be almost entirely ascribed to the quantum population of the phonon modes. The deviations observed above 200 K, allowed us to quantify the effect of anharmonic scattering. Additionally, the thermal decoupling observed between layers suppresses the possibility of thermal rectification in GJs. Our findings shed new light on thermal transport across GJs, revealing thermal decoupling between layers that is behind the large TBR observed. These results also imply that the presence of GJs in large-area (e.g. CVD-grown) graphene should not affect the overall thermal conductivity of the material, unlike GB defects. Thus, the thermal properties of CVD-grown graphene are not expected to be affected by the presence of small bilayer islands, because most heat will be carried in the bottom layer.

4.6. Summary of Contribution

I ran NEMD simulations to calculate the temperature profile across step junctions, which elucidated that the thermal resistance comes from weak interlayer coupling. In addition to NEMD simulations, I also ran ESKM calculations to determine a more quantitative thermal conductance across the step junction at varying overlap lengths and temperatures. The NEMD calculations led to the conclusion that step junctions lack thermal rectification due to thermal decoupling between

layers, which was a different conclusion from previous NEMD results. Modelling of both supported and suspended devices quantitatively showed the effect that SiO_2 has on GJs. Finally the mode polarization resolved transmission function I calculated showed that out-of-plane modes are the major heat carriers in these devices.
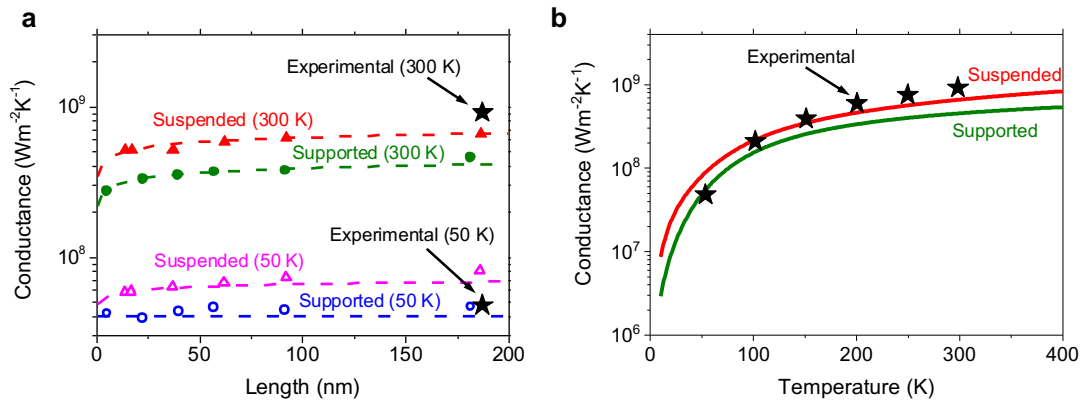
FIGURE 4.5. Calculated thermal conductance per unit area of a 1L–2L GJ, either suspended or supported on SiO_2 substrate. (a) Calculated conductance versus length of the bilayer portion at 300 K and 50 K temperature (symbols). Dashed lines are guide to the eye. The stars correspond to the experimental data. (b) Calculated conductance (lines) and experimental data (star symbols) versus temperature, both for suspended and SiO_2-supported GJs. The calculations use the same dimensions as in the experiment (180 nm long bilayer).

Thermal Transport Across Graphene-MoS2 Superlattices

5.1. Introduction

Controlling thermal transport at the nanoscale is a major engineering challenge with applications in nanoelectronics, photonics, and energy conversion. Traditional approaches of controlling heat flow have relied on top-down methods, where the thermal conductivity of a material is tuned either through the incorporation of defects [18, 160] or via a reduction in dimensionality. [161] While these approaches have resulted in the discovery of new regimes of thermal transport, as well as novel applications, they offer limited flexibility in terms of the range of thermal properties that can be accessed. In contrast, two-dimensional (2D) materials offer the unique ability to engineer thermal transport in a bottom-up manner. Layer-by-layer (LBL) assembly enables the creation of synthetic heterostructures with artificially tailored optical and electronic properties. [162] Because the distribution of atomic masses and bond strengths can be varied on the length scale of individual atoms, it has also been suggested that phonon spectra and thermal transport can be engineered in extreme ways. [163, 164] This tunability arises from variations in atomic composition on the scale of phonon wavelengths (few nanometers), as well as large coherence lengths of heat-carrying phonons traveling across van der Waals (vdW) interfaces. [17]

The ability to choose different 2D layers and stack them in a deterministic fashion opens a large range of possible metamaterial architectures with tailored thermal transport and thermoelectric conversion properties. [165] At the same time, understanding the factors limiting thermal transport at vdW heterointerfaces is crucial for several applications in photonics and nanoelectronics. Energy dissipation creates heat, and interfaces are often the primary bottleneck for cooling a device. [166,

---

[0]The work described in this Chapter is reproduced in partial or full form from the following publication:

- A. Sood et. al. ACS Nano. 2021, 0 [77].

167] Using techniques like Raman spectroscopy, time-domain thermoreflectance (TDTR), and time-resolved x-ray diffraction, previous studies have characterized the thermal boundary resistance (TBR) of various vdW interfaces between 2D materials and substrates, as well as between different 2D layers. [**153**, **168**, **169**, **170**, **171**, **172**, **173**, **174**] It has generally been found that these interfaces are more resistive than those between isotropic, three-dimensional (3D) materials. [**174**]

Despite these efforts, much remains to be understood about the fundamental mechanisms governing heat transport in vdW superlattices, and a systematic understanding is presently lacking. To design a new class of vdW thermal metamaterials, as well as understand factors limiting heat dissipation in 2D heterostructure devices, the following key questions need to be addressed: What are the primary factors governing thermal transport at vdW junctions, in particular, what are the roles of vibrational mismatch and interlayer separation? How does heat flow across a heterojunction compare to that across a homojunction? Finally, can we create 3D solids with tailored thermal conductivity by stacking 2D materials with matched or mismatched vibrational modes, for a variety of applications?

To shed light on these questions, here we design an array of LBL-assembled vdW solids made of two dissimilar 2D materials: monolayer graphene (G) and monolayer MoS_2 (M). Through combinatorial stacking of these monolayers, we construct nine sequences, G, GG, MG, GGG, GMG, GGMG, GMGG, GMMG, GMGMG (see Fig. 1), and measure their cross-plane thermal resistance, R_{2D}. This is done using a high-throughput experimental approach employing spatially-correlated TDTR microscopy [**18**, **175**] and optical/spectroscopic imaging. Combining experimental results with non-equilibrium molecular dynamics (NEMD), we investigate the effect of layer number (G vs. GG vs. GGG and M vs. MM) and vibrational mismatch (GM vs. GG and MM) on thermal transport. NEMD simulations with finite-temperature thermal expansion effects accurately predict the thermal resistances of the G, GG, GGG, GMG and GMMG sequences to within 20% of experimental values. The prediction for the thickest sequence (GMGMG) is ~30% lower than measured, but it becomes consistent if a larger-than-equilibrium interlayer separation arising from stacking disorder is considered. Taken together, our results establish design rules governing heat transport

in vdW metamaterials. By exploiting these rules, we create a 9-atom thick 'artificial solid' consisting of a graphene/MoS_2 superlattice with an effective cross-plane thermal conductivity lower than air, making it one of the best-known thermal insulators among fully-dense materials.

5.2. Methods

5.2.1. CVD growth of graphene and MoS_2: Continuous monolayer graphene samples were prepared via a Cu- mediated low-pressure CVD process. Cu foil (99.9 % purity, 33 m thick, JX Nippon Mining Metals) was placed in a 2-inch quartz tube after cleaning with acetic acid. After annealing the Cu foil under hydrogen atmosphere at 1040°C, graphene was synthesized by flowing methane and hydrogen gas at 1040°C for 40 minutes. Discontinuous monolayer MoS_2 samples consisting of triangular-shaped crystals were prepared via an atmospheric-pressure CVD process on a SiO_2/Si substrate. The SiO_2/Si substrate was first decorated with 20 l of a perylene-3,4,9,10 tetracarboxylic acid tetrapotassium (PTAS) solution. It was placed in the center of a 2-inch quartz tube facing ~0.6 mg of MoO3, while sulfur was located upstream. MoS_2 was synthesized by the interaction between the sulfur carried by 2 sccm of argon inflow and the vaporized MoO3 on the substrate. To obtain discontinuous monolayers, the growth temperature and time were carefully tailored and adjusted in the range of 700-800°C and 10-20 minutes, respectively, and the position of sulfur was optimized. The samples were prepared without controlling the interlayer twist angles.

5.2.2. Polymer-assisted transfer process: Multilayer stacks comprising graphene (G) and MoS_2 (M) monolayers were prepared via multiple polymer-assisted layer-by-layer transfer processes. An as-grown graphene film on Cu foil was spin-coated with Poly(methyl methacrylate) (PMMA, 950K A4) and Polystyrene (PS, 2.8 g/mol). The Cu foil was etched away by placing the sample in a Cu etchant (CE-100, Transene) for 1 hour. The resulting PS/PMMA/G stack was rinsed thoroughly in a deionized water bath. The stack was pinched out of the bath and placed onto an as grown MoS_2 sample on a SiO_2/Si substrate. Note that the G/M interface was dry i.e. it did not see polymer. While maintaining adhesion between graphene and MoS_2, a droplet of water was used to delaminate MoS_2 from the SiO_2/Si substrate, [176] resulting in a PS/PMMA/G/M stacked sample. Higher order stacks were prepared by iterating this procedure as required. For example, to assemble the GMGMG stack, the next step involved transferring this stack onto another as grown

65

graphene sample on Cu foil and repeating the above steps. Note again that the transfer process did not introduce polymer between the 2D layers. The final step involved transferring this stack (e.g. PS/PMMA/G/M/G/M/G) onto a SiO$_2$ (90 nm) on Si substrate. The PS/PMMA layers were removed by soaking the sample in toluene.

5.2.3. Time-domain thermoreflectance: TDTR is an optical pump-probe technique, which is used to measure thermal conductivity of thin films and TBR of interfaces. Details of this method and our setup are described elsewhere. [**17**, **18**, **175**] Briefly, our setup is based on a 1064 nm, 82 MHz oscillator that produces ~9 ps pulses. Pump pulses are frequency-doubled to 532 nm by second harmonic generation, and amplitude modulated at a frequency of fmod = 10 MHz using an electro-optic modulator. An optically opaque 80 nm thick Al transducer layer absorbs the pulses and converts them to heat. As the heat pulses diffuse through the film of interest, in our case the stack of 2D layers, the temperature decay of the transducer is monitored by measuring the reflected probe intensity as a function of delay time between the pump and probe (0 to 3.7 ns). The measured data consists of the in-phase and out-of-phase voltage components of the probe intensity demodulated at fmod using a lock-in amplifier, V_{in} and V_{out}, respectively. In a typical measurement, the time- series of voltage ratio data (= -V_{in}/V_{out}) is fit to the solution of a 3D heat diffusion model to extract R_{2D}.

5.2.4. TDTR mapping: In the present experiments, we adapted the TDTR technique to create maps of R_{2D} by fixing the pump-probe delay time at +250 ps and raster scanning the sample. At each position on the sample, R_{2D} was extracted by comparing the voltage ratio (= -V_{in}/V_{out}) with a fixed-delay correlation curve obtained from the thermal model (Fig. S1). Spatial variations in the interfacial resistance due to different layer stacking appear predominantly as variations in V_{out} (Fig. S2). The thickness and thermophysical properties of Al and SiO$_2$ layers, and Si substrate were either measured or taken from literature. In the current experiments, we used a root-mean-square laser spot size of ≈5.1 m, and pump and probe incident powers of approximately 12 and 3 mW, respectively. The estimated steady state temperature rise is ~2 K. The FWHM spatial resolution of this technique is ≈2.2 m (Fig. S5). We and others have previously used this technique to

66

measure spatially-inhomogeneous thermal conductivity in polycrystalline diamond, [175] lithium-intercalated MoS_2, [18] and other materials. [171, 177, 178, 179]

5.2.5. Molecular dynamics simulations: Interatomic interactions are modeled with empirical potentials tested to reproduce the vibrational properties of graphite, MoS_2, and aluminum: specifically the reparametrized Kolmogorov-Crespi (KC) [68] was used for the interlayer graphene-graphene interactions, Lennard-Jones (LJ) [180] for the interlayer graphene-MoS_2 interactions, optimized Tersoff [64] for the in-plane graphene interactions, reactive empirical bond-order (REBO)-type Mo-S potential [181] for all $MoS_2 - MoS_2$ interactions, Morse potential [182] for the Al-graphene interactions, and embedded atom model (EAM) [183] for the Al-Al interactions.

The models were built replicating the commensurate 4:5 MoS_2-graphene hexagonal unit cell, which is made of 4x4 MoS_2 unit cells and 5x5 graphene unit cells. [184] The resulting GMG cells were then made commensurate with aluminum by creating a 13:3 Al-GMG unit cell using an aluminum fcc cell with a lattice parameter of 0.286 nm. (111) Al slabs were placed on both sides of the GMG heterojunctions. We adopt periodic boundary conditions in the plane perpendicular to transport and fixed boundary conditions in the transport direction. The latter were implemented by constraining the coordinates of the outermost layer of Al atoms. We took special care to optimize the interlayer separation in the device by minimizing the free energy with the quasi-harmonic approximation [76, 185, 186] (QHA) instead of classical MD in the constant pressure canonical ensemble, as the TBR is critically sensitive to cross-plane expansion as shown by **??**B. We minimize the free energy with the QHA because it yields a 0→300 K graphite thermal expansion of 1.12%, which is in better agreement with the measured thermal expansion [187] of 1.54% than MD simulations with the Nosé-Hoover barostat, which yields an expansion of 0.53%. The better agreement between QHA thermal expansion and experiment over MD likely results from the inclusion of quantum statistics in the QHA, which help to correctly include the populations of soft flexural modes. The QHA free energy was minimized with respect to c-axis expansion and was computed by F(V,T) = $E_{0K}(V)$ + $F_{vib}(V,T)$ where E_{0K} is the total energy of the system at 0 K at a given volume, and F_vib represents the vibrational contribution to the free energy:

$$\sum_{\nu} \frac{\hbar\omega_{\nu}}{2} + \frac{ln(1 - e^{-\beta\hbar\omega_{\nu}})}{\beta}$$

67

where ω_ν^2 are the dynamical matrix eigenvalues yielded from all the atoms in the system except for the outer three layers of Al slabs on both sides of the device, and $\beta = (k_B T)^{-1}$. The dynamical matrices used for calculating the vibrational free energy were computed with LAMMPS [**109**] using the finite difference method with an atomic displacement of 10-7 nm. Once the interlayer separation was minimized according to the free energy, we calculated the thermal resistance of the devices by NEMD, following the protocol established in Ref. [**?**]. An outer layer of Al was fixed while the middle three layers of Al (out of nine layers) on each side were thermostatted to 350 K and 250 K with a Langevin integrator with a 1 ps relaxation rate. The equations of motion were integrated with a 1 fs timestep. NEMD simulations were run, using LAMMPS, [**109**] for 4.5 ns to ensure that a steady state heat flux was reached. Simulation configurations and temperature profiles computed in these simulations are shown in Fig. **??** and Fig. **??**.

5.3. Experimental Results

MoS_2 and graphene monolayers were grown by chemical vapor deposition (CVD) (see Methods for details). [**188**,**189**] Heterostructures were assembled by transferring these layers using a polymer-based process onto SiO_2 (90 nm) on Si substrates (see Methods). These substrates were pre-patterned with ~50 nm thick Ti/Au alignment markers. Three samples were prepared in all, as follows. Samples D1 and D2 each have up to 4 layers, containing regions with G, GG, MG, GMG and GMMG stacking. Both samples were prepared from the same transfer process and were cleaved from a single chip within ~1 cm of each other. Sample D3 contains up to 5 layers, with regions of GG, GGG, GMG, GGMG, GMGG, and GMGMG stacking. Both D2 and D3 were annealed at 350°C for 3 hours under vacuum (pressure ≈ 7 Torr) to investigate the effect of interlayer coupling on thermal transport, whereas D1 was not annealed.

5.1A shows a schematic of the various stacking sequences grouped by the number of layers n. These are: (n = 1) G; (n = 2) GG, MG; (n = 3) GGG, GMG; (n = 4) GGMG, GMGG, GMMG; and (n = 5) GMGMG. A cross sectional high-resolution transmission electron microscopy (HRTEM) image of the GMMG stack from the annealed sample D2 is shown in 5.1B. Four layers are distinguishable, with a total stack thickness of ≈ 1.7 nm between the top and bottom graphene.

[5.1](#)C shows a high-angle annular dark-field scanning transmission electron microscopy (HAADF-STEM) image, where atomic number contrast enables visualization of the two MoS_2 layers. From this image, we measure the M-M distance to be $0.6 - 0.7$ nm, which is compatible with the 0.616 nm c-axis lattice parameter [5] in bulk 2H-MoS_2, indicating good interface quality in our LBL-assembled samples.
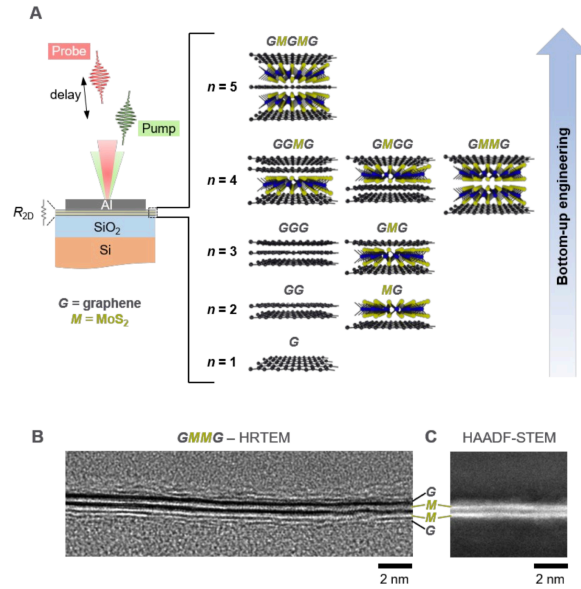
FIGURE 5.1. Combinatorial stacking of atomically-thin layers. (A) Cross-sectional schematic of the sample, comprising Al (80 nm)/2D stack/SiO_2 (90 nm)/Si substrate, where the '2D stack' can be one of nine sequences as shown on the right: G, GG, MG, GGG, GMG, GGMG, GMGG, GMMG, and GMGMG, with n denoting the number of layers. (B) High-resolution transmission electron microscope (HRTEM) and (C) High-angle annular dark-field scanning transmission electron microscope (HAADF-STEM) images of a cross-section of GMMG.

To measure the thermal resistance across the stacks, R_{2D}, we used TDTR microscopy (see Methods, Fig. S1-S3). The samples were capped with an 80 nm thick Al film using electron-beam (e-beam) evaporation to serve as a transducer (Fig. S4). The edges of the pre-patterned Ti/Au markers remained visible under an integrated dark-field microscope even after Al deposition, enabling coarse alignment of the sample under the TDTR laser. [17] Finer alignment was achieved by scanning the sample and constructing thermal resistance maps with a pixel size of 0.5 or 1 m. The full-width at half-maximum (FWHM) spatial resolution of this technique is $\approx$2.2 m (Fig. S5).

By comparing the TDTR images with optical micrographs taken before Al capping, a one-to-one mapping was made between the stack configuration and measured R_{2D}. As mentioned before, a unique feature of our experiments is the ability to measure multiple stack configurations within the same sample. This is enabled by the finite size (about tens of m) of the triangular MoS_2 monolayers and by tears (missing regions) in the graphene monolayers. Because we probe different regions within a few microns of one another, we can mitigate concerns about spatial variations in the quality of the top (between Al and the top 2D layer) and bottom interfaces (between the bottom 2D layer and SiO$_2$ substrate) which could otherwise affect the measured R_{2D}. For 8 of the 9 stacks, the top-most and bottom- most layers are G, which enables direct comparisons of the 'intrinsic' stack resistances.

??A shows an optical image of a region of sample D1. Three stack sequences are distinguishable based on their optical contrast: GG, GMG and GMMG. MoS_2 photoluminescence (PL) emission measurements made on the same region and are shown in the inset of **??**B; the maps plot the intensity integrated over the energy range 1.82 to 1.9 eV. The PL intensity of the MM region is brighter than monolayer M regions, suggesting weak interlayer electronic coupling. As has been shown previously, monolayer MoS_2 is a direct band gap semiconductor with bright PL emission, whereas bilayer MoS_2 (even with an arbitrary twist angle) is indirect band gap with significantly lower PL intensity. [**13**, **190**] In the as- prepared sample D1, the MoS_2 layers are weakly coupled and they behave as individual monolayers whose intensity is approximately doubled in the bilayer region.

??B displays a TDTR microscopy image of the same region where we plot spatial distribution of R_{2D}. Details of the mapping technique are provided in the Methods section. A clear correspondence is seen between the optical, PL, and TDTR images. This visual correlation enables a direct extraction of R_{2D} for the different stacking configurations without any image processing. The GMMG region is the most thermally resistive, followed by GMG and GG. The sample also has regions of G and MG stacking, which are not shown in this map. Note that the TDTR measurements were made after the sample was coated with an optically-opaque 80 nm thick layer of Al; therefore, these results demonstrate the sub-surface imaging capability enabled by TDTR microscopy. Single-spot TDTR time scans (over the full range of delays) for each stack configuration are provided in **??**C.
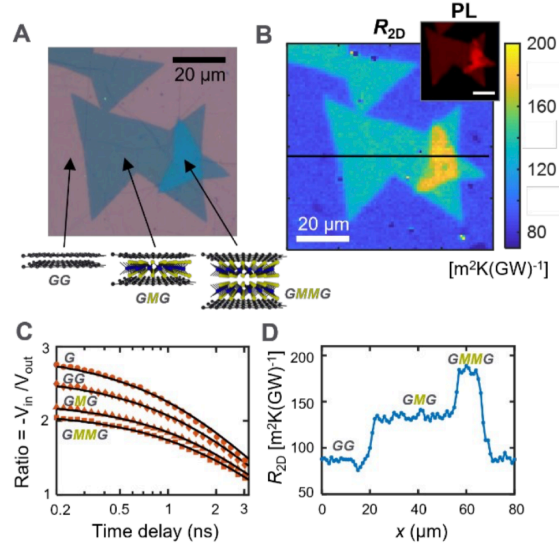
FIGURE 5.2. Correlative thermal, optical, and spectroscopic imaging. (A) Optical micrograph of sample D1 with stacks up to GMMG. Three regions are labeled, GG, GMG and GMMG. This sample was not annealed. (B) Map of the TBR between Al and SiO_2 (R_{2D}) measured by TDTR microscopy. Inset: MoS_2 PL map showing brighter signal from GMMG compared to GMG due to weak M-M coupling (scale bar 20 m). A close correspondence is observed between the TDTR, optical, and PL micrographs. (C) TDTR time delay scans showing decay rates decreasing in the order G > GG > GMG > GMMG, corresponding to R_{2D} increasing with layer number. (D) Line scan of R_{2D} along the solid black line in (B).

The decay rate of the ratio (= $-V_{in}/V_{out}$) signal encodes information about the interface thermal resistance: a faster (slower) rate indicates a lower (higher) R_{2D}. The interfaces show uniformity over large areas, as illustrated by the thermal resistance profile in **??**D, which is plotted along the line marked in **??**B.

In LBL-assembled vdW stacks, it has been suggested that the interface quality can be improved significantly and made 'intrinsic' by high-temperature annealing. [**191**, **192**] To probe its effect on interlayer thermal transport, we measure R_{2D} on the annealed sample D2. Fig. 3A shows an optical image of a D2 region where five different regions are identified besides bare SiO_2: G, GG, MG, GMG, and GMMG. As discussed above, PL intensity provides a useful means to probe the strength of interlayer electronic coupling. We perform PL mapping of the same sample region (indicated by dash-dotted lines in **??**A) before and after the anneal. As demonstrated in **??**B, after annealing, there is a crossover in the MoS_2 PL intensity with GMMG showing quenched emission compared

to GMG, consistent with stronger M-M electronic coupling. We confirm that this quenching is not due to enhanced G-M electronic coupling, as the PL intensity of GMG does not change significantly on annealing. This is also seen clearly in the PL point spectra in Fig. S6.
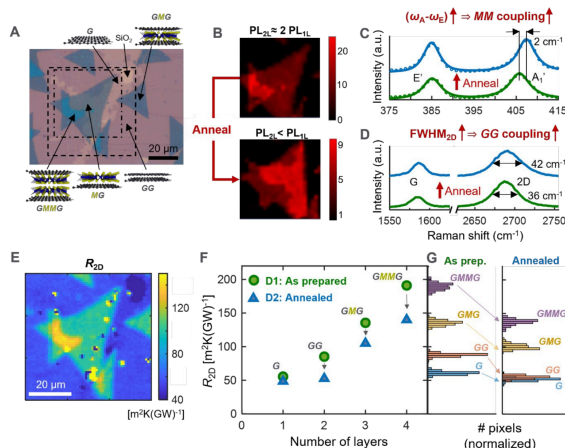

FIGURE 5.3. Vacuum annealing tunes interlayer coupling and thermal transport. (A) Optical micrograph of annealed sample D2 showing stacking sequences G, GG, MG, GMG and GMMG. (B) MoS_2 PL maps of the region marked by the dash-dotted lines in (A) before and after annealing at 350°C for 3 hours under vacuum. A crossover is observed after annealing, with the PL of GMMG becoming quenched relative to GMG, indicating stronger M-M coupling. Note that the sample is rotated by ~20° in the bottom panel; also, the image is slightly distorted, possibly due to stage drift. (C) MoS_2 Raman spectra of GMMG before (green) and after (blue) the anneal. A larger frequency difference between the A1' and E' modes suggests enhanced M-M vibrational coupling upon annealing. (D) Graphene Raman spectra of GG before (green) and after (blue) the anneal. An increase in the width of the 2D peak, and a decrease in the intensity ratio of 2D and G peaks indicates strengthened G-G coupling. (E) TDTR map of R_{2D} for the region marked by the dashed lines in (A). (F) R_{2D} of stacks G, GG, GMG, and GMMG in samples D1 (as prepared, i.e. not annealed) and D2 (annealed), extracted from single-spot time scans. Error bars are omitted for clarity (see Table S1 for uncertainty analysis). (G) Histograms of R_{2D} for various stacking sequences based on regions of interest shown in Fig. S7 and Fig. S8.

We employ Raman spectroscopy to probe the effect of annealing on interlayer vibrational and electronic coupling. Fig. 3C shows that, on annealing, the A_1 peak of MoS_2 in the GMMG region blueshifts, while the E' peak shows little change. This increased separation by $\approx 2\ cm^{-1}$ between the A_1 and E' phonon frequencies indicates stronger M-M vibrational coupling in the annealed sample.26 Fig. 3D plots the Raman spectra of graphene in the GG region before and after

annealing. We observe an increase in the FWHM of the 2D peak, by $\approx$6 cm^{-1}. This is consistent with improved G-G electronic coupling, and a modification of the electronic band structure in bilayer graphene. [**193**] The reduced intensity ratio of 2D and G peaks, from ~2.5 to ~1.8 further supports the notion of enhanced G-G interaction upon annealing.

The sample's thermal resistance map after annealing is shown in Fig. 3E, from which we extract R_{GMMG}, R_{GMG}, R_{GG} and R_G. In Fig. 3F we plot the thermal resistances of the different stack sequences from samples D1 and D2 before and after annealing; these data are extracted by fitting single-spot TDTR time scans over the full delay range. To demonstrate the spatial uniformity of the interfaces, we plot histograms of R_{2D} by defining regions of interest (ROI) in the TDTR maps, as shown in Fig. 3G (locations of ROI polygons are given in Fig. S7 and Fig. S8). We find good agreement between the thermal resistance extracted from the full-delay-time single-spot scans and the fixed-delay-time 2D maps. Spatial variations are relatively small and do not affect our main conclusions. In the unannealed sample D1, we find that R_{2D} scales approximately linearly with the number of layers (n), such that $R_{GMMG} > R_{GMG} > R_{GG} > R_G$. In comparison, in the annealed sample D2, R_G is similar to D1, but R_{GG} is reduced strongly by ~40%, such that $R_G \approx R_{GG}$ after the anneal. R_{GMG} and R_{GMMG} also decrease, by ~23% and ~27%, respectively. Taken together with the PL and Raman measurements, these results reveal a strong correlation between the strength of interlayer coupling and thermal resistance of the vdW junctions. Furthermore, the fact that R_{GG} and R_G are similar after annealing, and each is smaller than R_{GMG}, suggests that the intrinsic conductance of a G-G homojunction is significantly larger than that of a G-M heterojunction. Note that our ability to draw these conclusions is based on our confidence that the Al-G and G-SiO_2 interface resistances do not vary significantly between different regions on a sample since they are within ~100 m of one another, and also do not change substantially upon annealing as R_G is similar before and after the anneal. While we also measure the thermal resistance of MG ($\approx$100 $m^2 KGW^{-1}$), we do not draw any major conclusions from it since its top layer is MoS_2, whose thermal resistance with Al could be different from that of graphene.

To probe these effects in higher order stacks we examine sample D3, which is annealed. **??**A,B present optical microscopy and TDTR thermal resistance maps of a region of the sample that has four stacking sequences: GGG, GMGG, GGMG, and GMGMG. A different region containing GG

73

and GMG sequences is shown in Fig. S9. Single-spot delay scans (**??**C) show that the temperature decay rates for stacks GG and GGG are very similar, as well as for stacks GMG, GMGG, and GGMG. Consistent with this, an ROI-analysis of TDTR maps (**??**E) illustrates that the R_{2D} distributions of GG and GGG overlap, as do those of GMG, GMGG, and GGMG. A summary of measurements made on this sample is presented in **??**D. The interfacial thermal resistances follow the trend: $R_{GMGMG} > R_{GMGG} \approx R_{GGMG} \approx R_{GMG} > R_{GGG} \approx R_{GG}$.
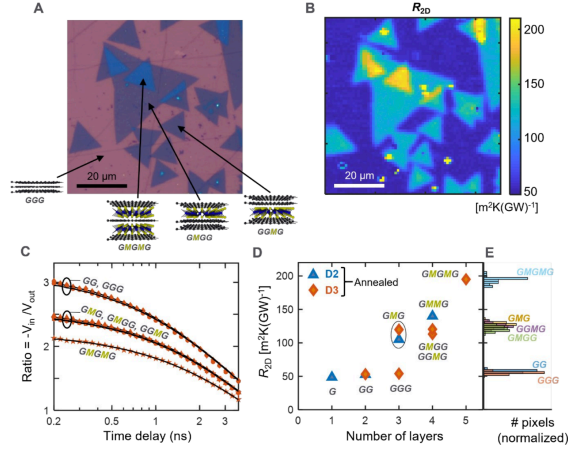

FIGURE 5.4. Towards ultralow thermal conductivity in higher order heterostructures. (A) Optical micrograph of sample D3 showing stacking sequences GGG, GMGG, GGMG and GMGMG. (B) TDTR map of R_{2D}; note that this sample is annealed. (C) Single-spot TDTR time scans. (D) R_{2D} of all sequences combining data from samples D2 and D3, as extracted from single-spot measurements. Error bars are omitted for clarity (see Table S1). (E) Histograms of R_{2D} for the different stacks in sample D3, based on regions of interest defined in Fig. S9. (C)-(E) show that the thermal resistances of GGMG and GMGG stacks are nearly identical, implying no thermal rectification. The highest order GMGMG stack has a thermal resistance that is equivalent to nearly 200 nm of SiO_2 even though it is $100\times$ thinner.

We make three key observations from the data. First, the strongly coupled (i.e. annealed) G, GG and GGG interfaces have nearly equal thermal resistance, indicating that phonon transport across these interfaces is quasi-ballistic. This is shown in D3 by $R_{GGG} \approx R+GG$, and in D2 by $R_{GG} \approx R_G$, and is furthermore consistent with the observation that $R_{GMGG} \approx R_{GGMG} \approx R_{GMG}$ (**??**C-E). We estimate the effective thermal resistance (ρ) of a single G-G junction, ρ_{GG}, using (R_{GGG} - R_{GG})D3 and (R_{GG} - R_G)D2, which gives $\rho_{GG} < 4 \ m^2KGW^{-1}$. This is consistent with prior

calculations of the cross-plane ballistic thermal resistance of graphite at room temperature, [194] which gave $\approx 3 \ m^2 KGW^{-1}$. Similarly, we also extract the effective thermal resistance of an M-M junction, ρ_{MM} using $(R_{GMMG} - R_{GMG})$ where R_{GMG} is averaged between D2 and D3; this gives $\rho_{MM} \approx 26 \ m^2 KGW^{-1}$. Our measurements of Al/nG/SiO$_2$ (n = 1, 2, 3) are in good agreement with previous data for the thermal resistance of exfoliated few-layer graphene in Au/Ti/nG/SiO$_2$ and Au/Ti/nG/Si heterostructures, [153, 179] where no strong layer dependence was observed. This similarity between our LBL- assembled CVD-grown layers and prior results on pristine interfaces in exfoliated crystals suggests a good G-G interface quality in our annealed samples. Further, given that our polycrystalline samples are not prepared with well-defined interlayer twist, this also indicates that turbostratic disorder may not have a strong impact on G-G thermal coupling.

Second, we find that the order of stacking does not affect the total thermal resistance, as shown by $R_{GMGG} \approx R_{GGMG}$. This implies no measurable thermal rectification in such vdW junctions. This is consistent with prior MD simulations of graphene/MoS_2 [195] and other 2D heterojunctions. [196] However, we do not exclude the possibility of rectification under significantly larger thermal gradients, when non-linearities in the vibrational spectra of G and M lattices may become important. [197] In the present experiments, the vertical temperature gradient is on the order of 1 K $nm^{-}1$.

Third, the heterojunction G-M is more resistive than the homojunctions G-G and M-M. We estimate the effective G-M resistance using $\rho_{GM} = (R_{GMGMG} - R_G)/4 \approx 37 \ m^2 KGW^{-1}$. Comparing this with the thermal resistances of homojunctions, we summarize the trend as: $\rho_{GM} > \rho_{MM} \gg \rho_{GG}$ This trend is consistent with previous MD simulations [195] which had calculated $\rho_{GM} \approx 3\rho_{MM}$ and $\rho_{GM} \approx 15 \ \rho_{GG}$ Notably, a single G-M heterojunction consisting of a graphene and MoS_2 monolayer placed only ~0.5 nm apart has a thermal resistance comparable to ~50 nm of SiO_2. Equivalently, the GMGMG stack with a total thickness of ~2 nm has an effective cross-plane thermal conductivity (= thickness/resistance) $< 0.02 \ Wm^{-1}K^{-1}$. This represents one of the lowest thermal conductivities among dense solids, [169, 198] lower than that of dry air at 1 atm and 300 K, ~0.026 $Wm^{-1}K^{-1}$. [199]

5.4. Molecular Dynamics Discussion

To gain further insights into the mechanisms governing heat transport in vdW stacks, we performed NEMD simulations. The following stacks were simulated to compare with the experiments: G, GG, GGG, GMG, GMMG, and GMGMG. Each stack was enclosed within nine-atom thick Al leads. To account for thermal expansion at finite temperature, the structures were relaxed at 300 K using a free-energy minimization (FEM) approach in the quasi-harmonic approximation (QHA). [**76**, **185**, **186**] As we will show later, thermal expansion is crucial to accurately capture the thermal resistances of the vdW junctions, owing to the strong sensitivity of the TBR to the interlayer spacing. Details of the simulation approach are provided under 5.2.

??A shows the calculated thermal resistances of the various stacks (blue bars) plotted alongside the experimental data (red bars). In the calculations, the plotted results include the resistances of the top and bottom Al-G and G-Al interfaces, whereas in the experiments, they include the Al-G and G-SiO$_2$ interfaces. In general, good agreement is seen between the trends in the experiments and simulations, with a deviation of $<20\%$ for all stacks except GMGMG.
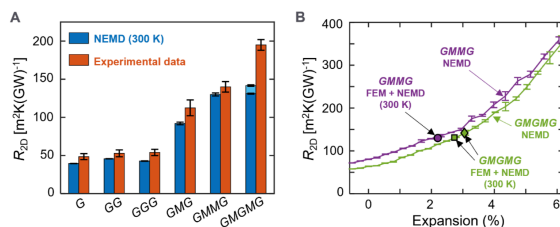

FIGURE 5.5. Molecular dynamics simulations and the effect of interlayer spacing on thermal transport. (A) NEMD calculations (blue bars) and experimental data (red bars) for various stacks. NEMD calculations are performed after relaxing each of the structures at 300 K, using a free-energy minimization approach that accounts for finite-temperature effects on the interlayer spacing. For GMGMG, the light blue bar denotes additional resistance when the MM layers are AA vs. AB stacked. For both theory and experiment, the plotted resistance includes the top and bottom interfaces with the leads. (B) NEMD-calculated thermal resistance of GMMG (purple curve) and GMGMG (green curve) as a function of cross-plane lattice expansion relative to zero Kelvin. Filled markers correspond to stacks with free-energy minimized lattice spacings at 300 K (purple circle—GMMG, green square—GMGMG with AB stacking between M layers, green diamond—GMGMG with AA stacking between M layers).

Notably, the simulations show that the resistances of the pure graphene junctions are independent of the number of layers, which is consistent with the measurements. This agreement is noteworthy considering that in the simulations adjacent G layers are AB stacked, whereas in the experiments the layers are arbitrarily twisted. This suggests that thermal transport across few-layer G-G junctions is quasi-ballistic and is not strongly sensitive to the interlayer atomic registry. This is also consistent with prior experiments on exfoliated AB-stacked few-layer graphene films where no layer-number dependence was observed in the cross-plane thermal resistance. [153] Next, the simulations predict the trend $R_{GMGMG} > R_{GMMG} > R_{GMG}$, which is consistent with the measurements. For GMGMG, two stacks are simulated, with AB and AA stacking of the M layers; the latter has a resistance that is ~8% larger than the former. The discrepancy between theory and experiments is the largest for GMGMG, at around 30%.

To understand possible reasons behind this, we consider the effect of interlayer spacing on thermal transport. To do this, we calculate the cross-plane thermal resistance of GMMG and GMGMG using NEMD, while varying the distance between two fixed layers of Al atoms within the top and bottom leads. In ??B, we plot R_{2D} versus the percentage cross-plane lattice expansion calculated relative to its value at T = 0 K (purple and green curves). We see a strong, non-linear increase in resistance with interlayer spacing: for instance, an expansion of only 4% leads to an increase of ~400% in the thermal resistance of GMGMG. This is qualitatively consistent with prior NEMD simulations [200] and ab initio lattice dynamics calculations [201] of the effect of cross-plane tensile strain on the c-axis thermal conductivity of pure MoS_2. In ??B, we also plot points corresponding to the expansion and R_{2D} values at 300 K using the FEM approach, which are in good agreement with the 0 K expansion curves. Based on these calculations, we suggest that the average interlayer spacing in the GMGMG sample is ~1% larger than the equilibrium spacing at 300 K, which causes NEMD to underpredict the measured resistance by ~30%.

5.5. Conclusions

We draw two conclusions from the analysis in 5.4. First, as the number of layers in the experimental vdW stack increases, the average interlayer separation exceeds the equilibrium value, possibly owing to trapped contaminants. Second, the strong sensitivity of the thermal resistance

to c-axis lattice expansion indicates that extreme care must be taken to ensure cleanliness of heterostructures, to be able to make fundamental measurements of interlayer phonon transport.

In conclusion, using a combinatorial experimental approach we have systematically characterized cross-plane thermal transport in LBL-assembled van der Waals stacks made of graphene and MoS_2. Using correlative time-domain thermoreflectance and photoluminescence spectroscopy, in conjunction with molecular dynamics simulations, we have examined the effects of vibrational mismatch, junction asymmetry, and interlayer coupling strength on heat transport across vdW interfaces. Our results provide a framework for understanding (tunable) heat flow in a broad range of vdW metamaterials and enable the creation of an artificial dense solid with an effective thermal conductivity lower than that of air. Lastly, the insights presented here will allow for improved engineering of heat flow at vdW heterojunctions in 2D electronics, which is crucial for achieving ultimate performance limits in emerging computing and photonic devices.

5.6. Summary of Contribution

I performed numerous NEMD calculations of G-M heterostructures to calculate the cross-plane thermal conductance across these devices. In doing so I elucidated that the thermal conductance has a strong dependence on the interlayer spacing and showed that up to GMMG there is an excellent agreement between theory and experiment. To achieve comparable thermal conductance I had to develop a workflow to generate G-M devices with higher accuracy interlayer spacing at non zero temperatures. With higher accuracy calculations and evidence that interlayer spacing plays a predominant role in thermal conductance, we were able to posit ideas to help explain the discrepancy found between theory and experiment for the GMGMG device. These insights and the conclusions drawn from them were crucial to the impact of the paper.

CHAPTER 6

Conclusions

2 Dimensional materials, i.e. van der Waals materials, are an exciting class of materials than can be stacked one on top of another to form new and exciting metamaterials. These low dimensional materials are often challenging to study since they span the quasi-ballistic transport regime, which reduces the number of methods one has to calculate their thermal conductance. Understanding how heat is transferred both in-plane and out-of-plane is imperative for future development in both the fields of nanophononics and nanoelectronics. Below are conclusions from this dissertation.

6.1. Computational methods

NEMD and ESKM are two useful computational methods for calculating thermal conductance. ESKM is an AGF equivalent that solves the problem in reciprocal space. NEMD is an MD based method, which integrates Newtons equations of motion and approaches the problem from a real space perspective. The strengths of NEMD includes handling anharmonicty effortlessly, where a major weakness of ESKM is that it does not. ESKM, however, handles quantum (Bose-Einstein) phonon populations and elastic scattering well below the Debye temperature, whereas NEMD is limited to classical (Boltzmann) populations. Both methods are used in this dissertation due to their advantage in studying vdW materials.

6.2. Chapter 3

The Langevin thermostat is recommended for use as the local thermostat for the heat source and sink in NEMD simulations, over Nosé-Hoover, as it is less likely to produce artifacts and controls the local temperature better. Nosé-Hoover thermostat artifacts are shown to appear in asymmetric nanostructures and these thermostats can negatively influence conclusions drawn from NEMD simulations.

6.3. Chapter 4

Temperature-dependent heat flow across graphene step junctions has been studied for both supported and unsupported systems. MD and LD simulations were used to analyze the GJ thermal transport. The simulations show that the top and bottom layers of the junction are only weakly thermally coupled, and the main source of TBR is not the step at the junction, but rather the weak coupling between the two layers in bilayer graphene. The experimental device setup shows as temperature increases that there is an increase in anharmonic effects due to the divergence from theory, which is based on ballistic transport. Additionally, the thermal decoupling observed between layers suppressed the possibility of thermal rectification in GJs. The thermal decoupling between layers also helps to explain the large thermal boundary resistance observed. These results also imply that the presence of GJs in large-area (e.g. CVD-grown) graphene should not affect the overall thermal conductivity of the material, unlike GB defects. Thus, the thermal properties of CVD-grown graphene are not expected to be affected by the presence of small bilayer islands, because most heat will be carried in the bottom layer.

6.4. Chapter 5

A major conclusions from 5 is that as the number of layers in the experimental vdW stack increases, the average interlayer separation exceeds the equilibrium value, possibly owing to trapped contaminants. A second major conclusion is that the strong sensitivity of the thermal resistance to c-axis lattice expansion indicates that extreme care must be taken to ensure cleanliness of heterostructures, to be able to make fundamental measurements of interlayer phonon transport. These conclusions are important guides for improving the engineering of heat flow at vdW heterojunctions in 2D nanoelectronics, which is crucial for achieving ultimate performance limits in emerging computing and photonic devices.
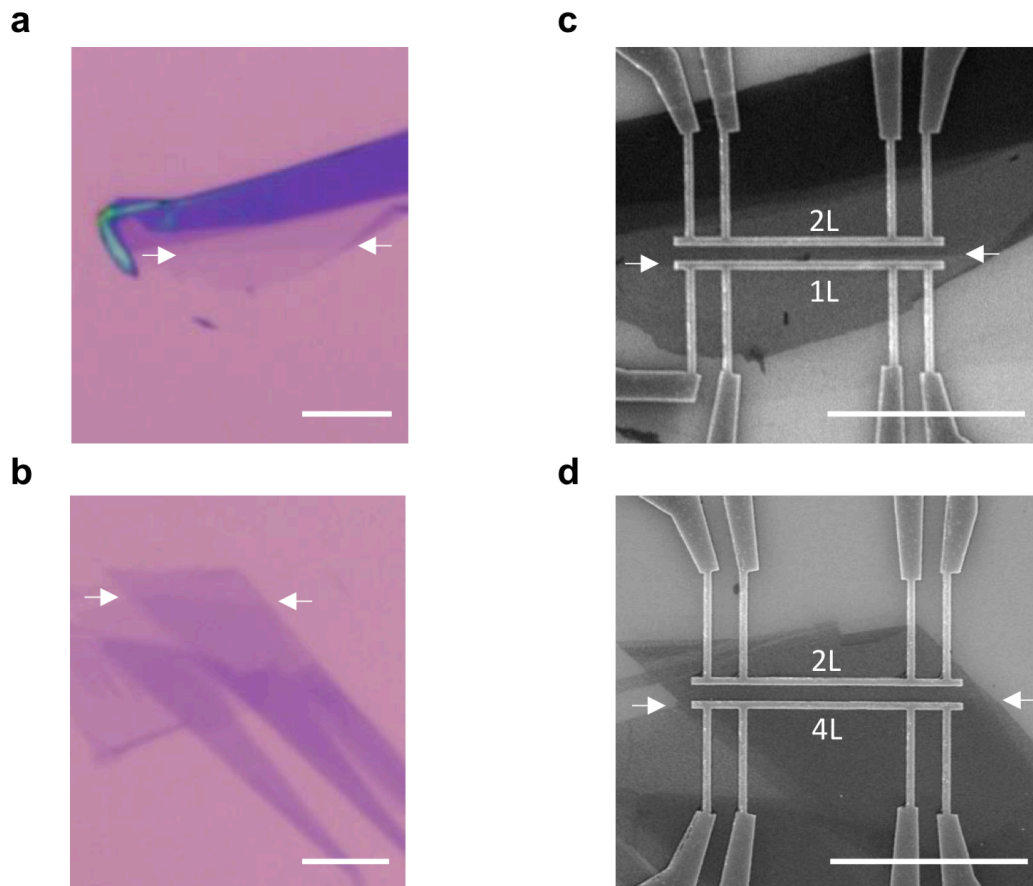
SJ Supplemental Figures

FIGURE A.1. a) and b) show optical images of the graphene flakes with 1L-2L and 2L-4L junctions respectively. c) and d) show SEM images of the same flakes after fabricating the metal lines at the junction. The arrows point out where the graphene junctions are located.

FIGURE A.2. (a) Optical image of the junction. Raman maps of (b) integrated area under the 2D peak, (c) 2D/G area ratio, (d) 2D/G peak intensity ratio, (e) 2D peak position, and (f) G peak position. The dashed line indicates the junction location.
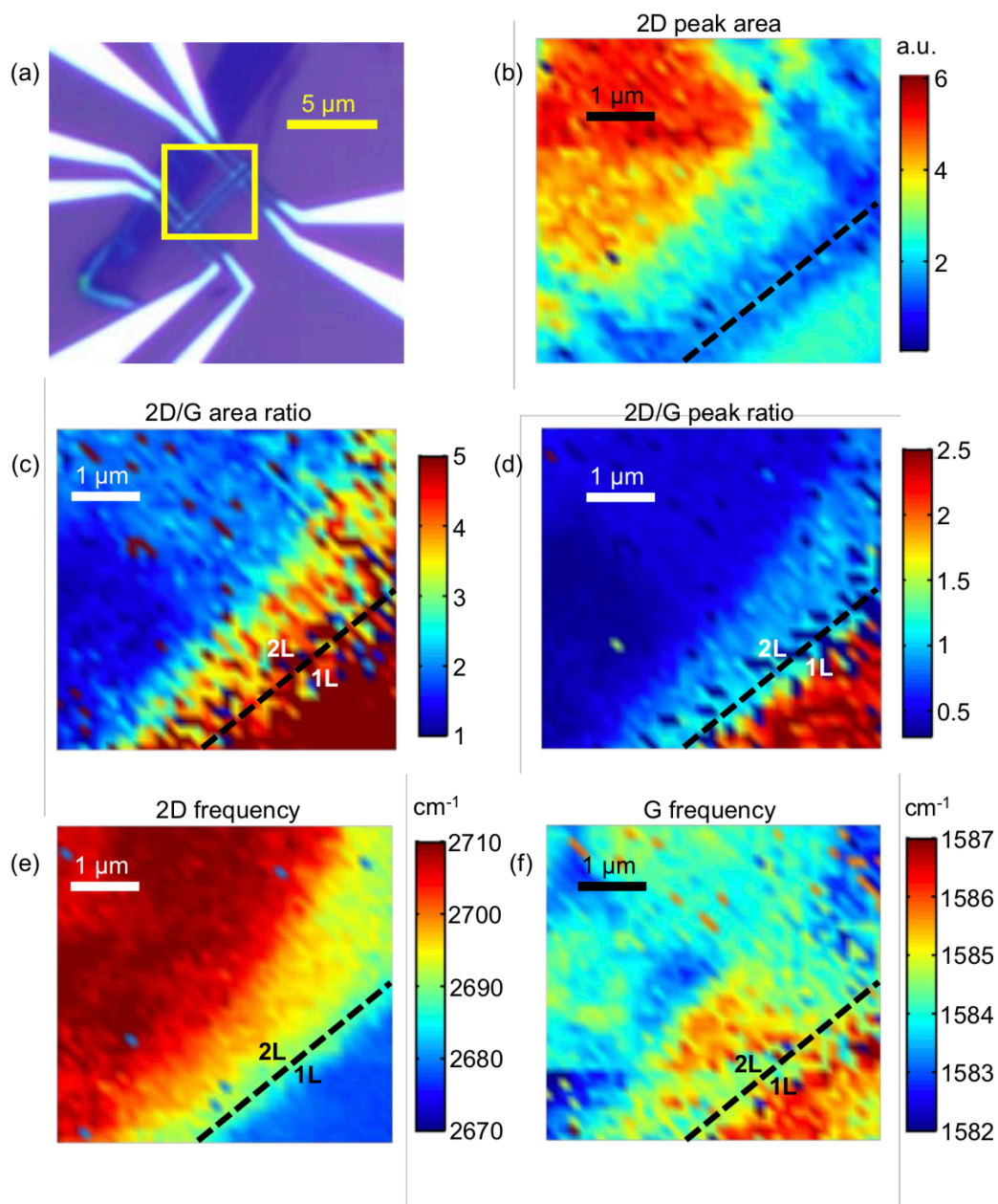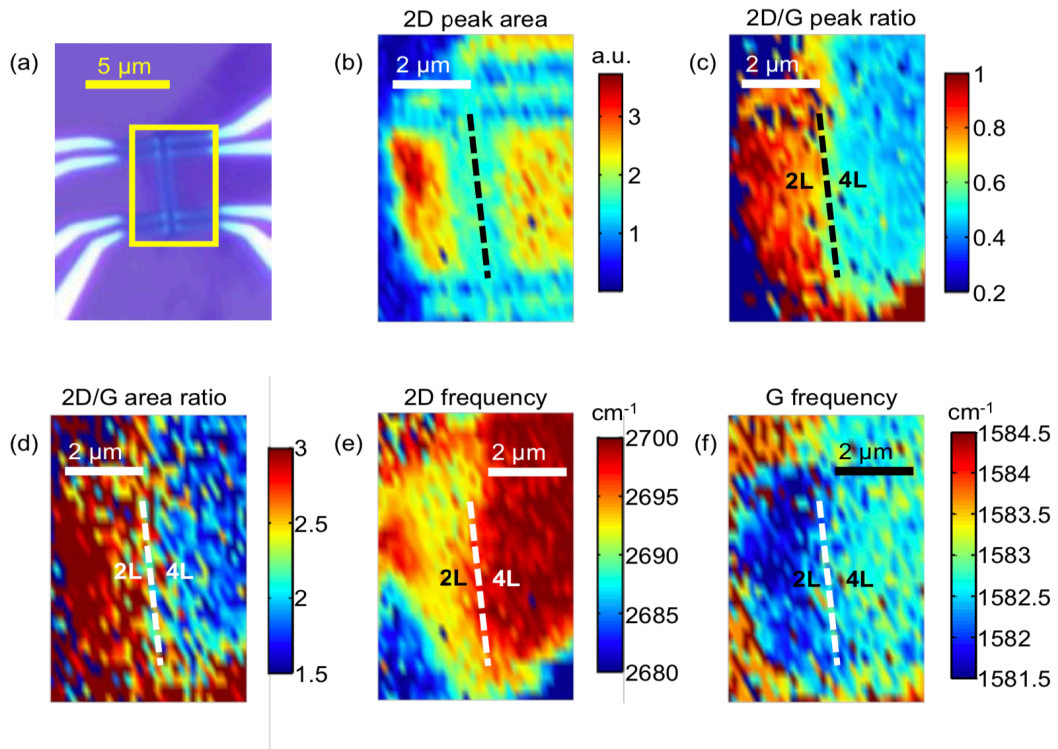
FIGURE A.3. (a) Optical image of the junction. Raman maps of (b) integrated area under the 2D peak, (c) 2D/G area ratio, (d) 2D/G peak intensity ratio, (e) 2D peak position, and (f) G peak position. The dashed line indicates the junction location.
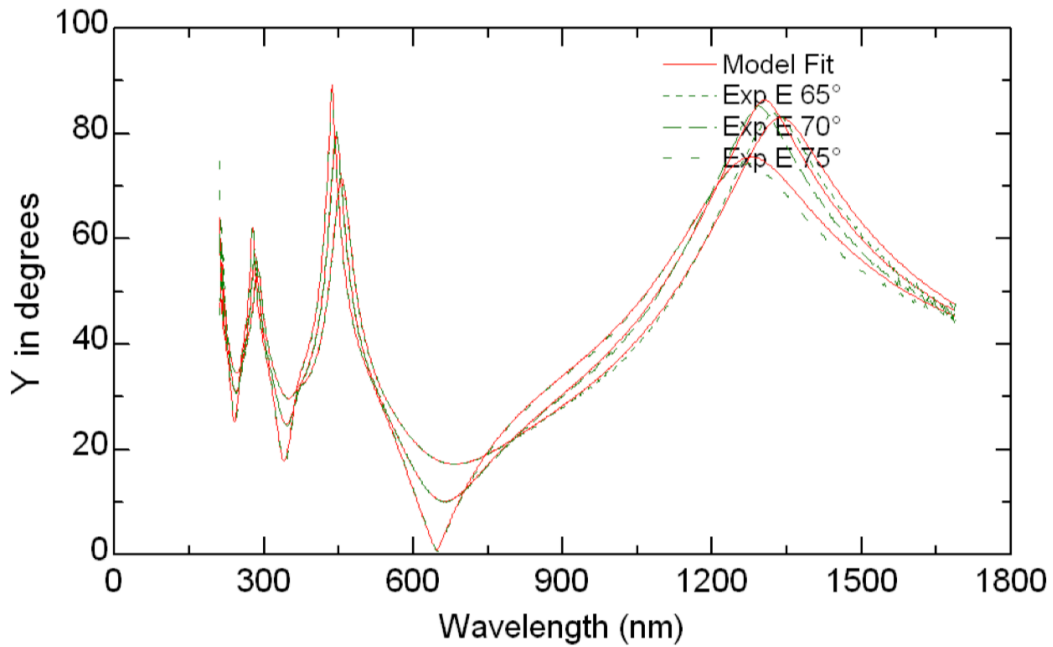
FIGURE A.4. Fit of our model to the polarized light phase change data versus wavelength of incident light for the SiO2 substrates used in our devices.
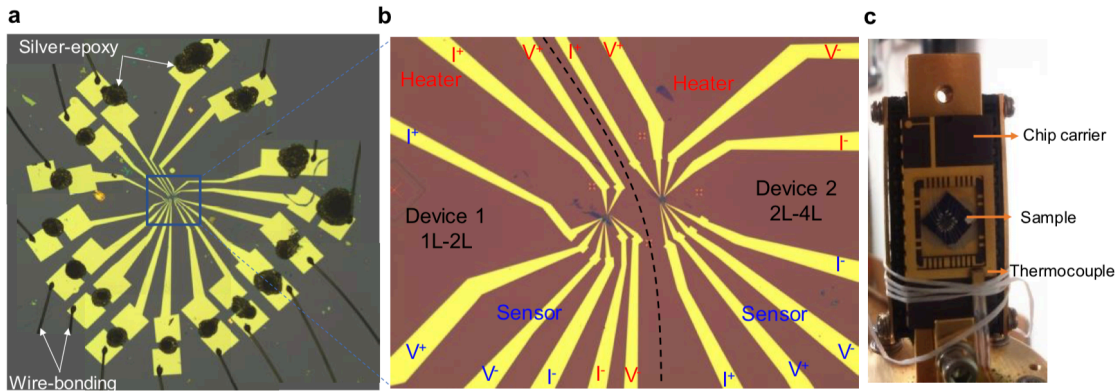
FIGURE A.5. a) Optical image of the full devices. This image shows the external pads that were used for wire bonding and the silver conductive epoxy drops that connects them electrically with the inner pads of the device. b) Optical image zoom in the 1L-2L and 2L-4L devices and a schematic map of the electrical connections of the four-probe electrodes for both the heater and sensor. c) Picture of chip carrier loaded in the arm of the cryostat. The sample is glued onto the chip carrier using silver paint and a thermocouple is attached to the surface of the chip to measure the temperature at the surface.

84
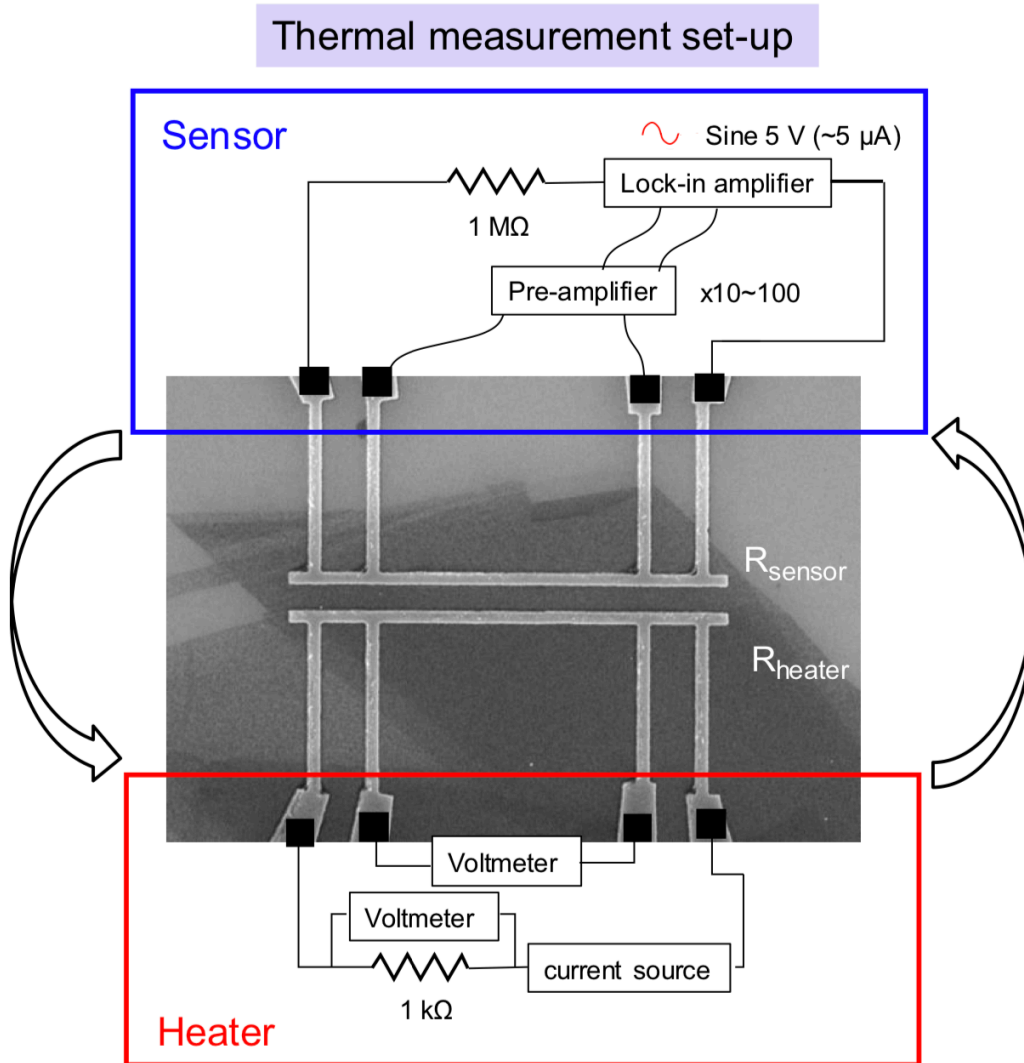
FIGURE A.6. Thermal measurement set-up. A DC current source is used to apply current to the heater line. The current provided by the source was also measured experimentally using a 1 kΩ resistor and a voltmeter. The voltage between the middle probes of the lines was measured using another voltmeter. The sensor line is connected in series with 1 MΩ and a lock-in voltage of 5 V (~5 A) is used to sense. The voltage from the voltage probes of the sensor line is amplified using a low noise pre-amplifier. The heater and sensor lines can be swapped to account for asymmetric heat flow across graphene junction, i.e. thermal recti- fication.
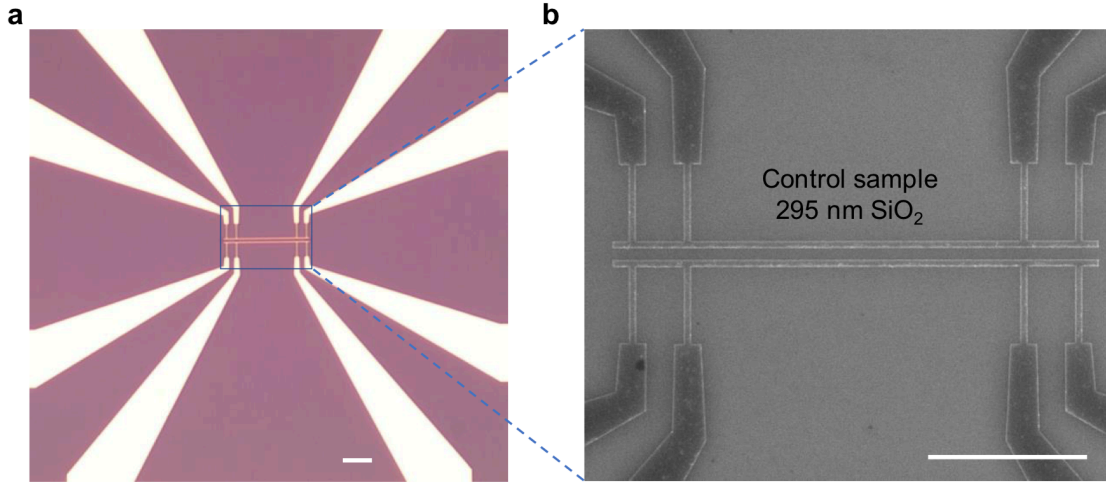
FIGURE A.7. a) Optical image of the control sample on SiO2 (on Si) with four probe electrodes at each metal line. b) Scanning electron microscopy image of the metal lines. Scale bars were set at 5 m size.
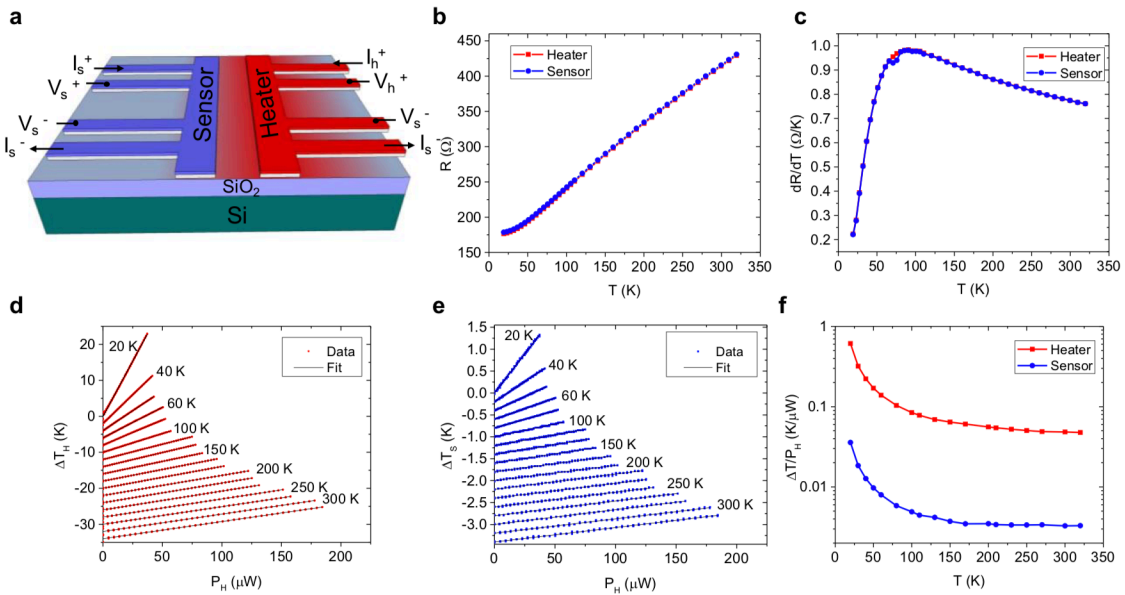
FIGURE A.8. a) Schematic drawing of the heater and sensor line on top of the Si/SiO2 control sample. The current, I, and voltage, V, probes are labeled in the image. b) and c) show the resistance, R, and dR/dT versus temperature for the heater (red symbols) and the sensor (blue symbols), respectively. d) and e) shows the temperature variation of the heater, ΔTH, and sensor, ΔTS, when sweeping the heater power for different temperatures, respectively. f) Temper- ature variations per heater power, ΔT/PH, as a function of temperature for the heater and the sensor.

86

FIGURE A.9. a) and b) show the electrical resistance of the heater and sensor lines as a function of temperature for the two different measuring configurations, i.e. before and after being swapped. c) and d) show dR/dT versus temperature for the heater (red symbols) and the sensor (blue symbols) obtained from a) and b), respectively.

FIGURE A.10. a) Schematic drawing for the first measuring configuration, where the heat flows from 1L to 2L graphene. b) and c) show the temperature var- iation of the heater, ΔT_H, and sensor, ΔT_S, when sweeping the heater power for different tempera- tures, respectively. d) Schematic drawing for the second measuring con- figuration, where the heater and sensor are swapped and the heat flows now from 2L to 1L graphene. e) and f) shows ΔT_H and ΔT_S, vs heater power for different temperatures in this configuration, respectively.
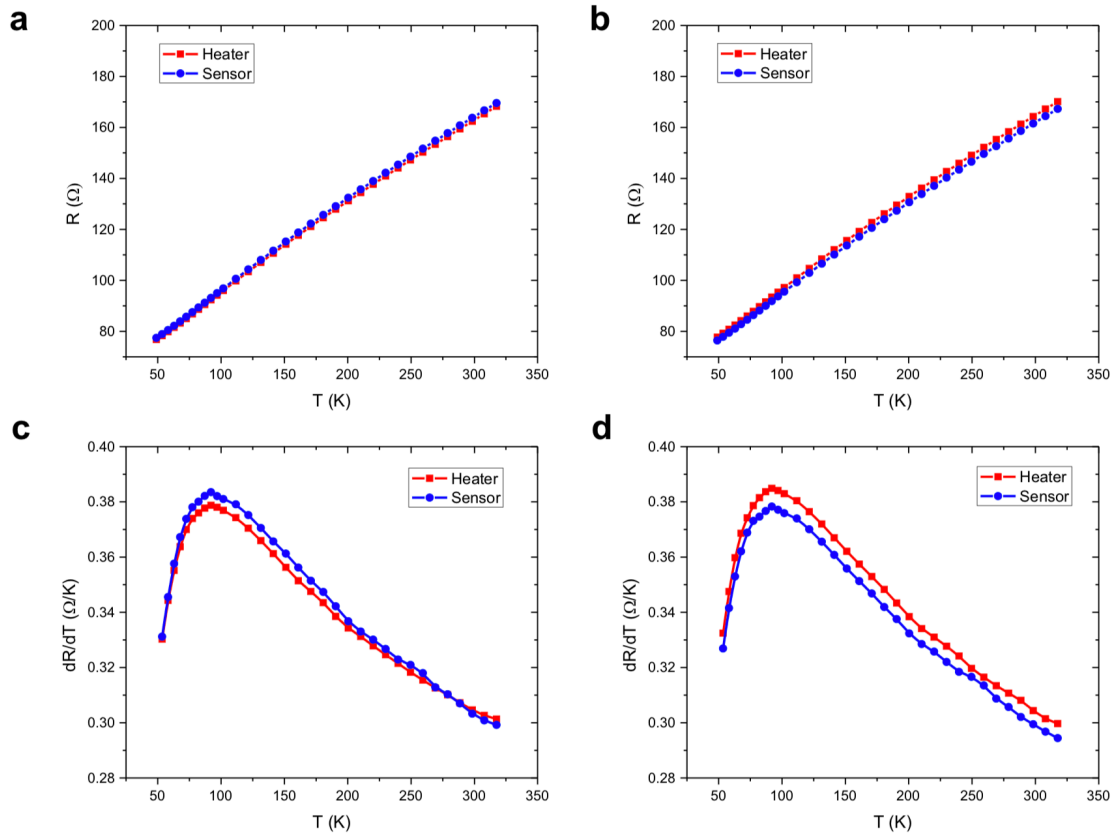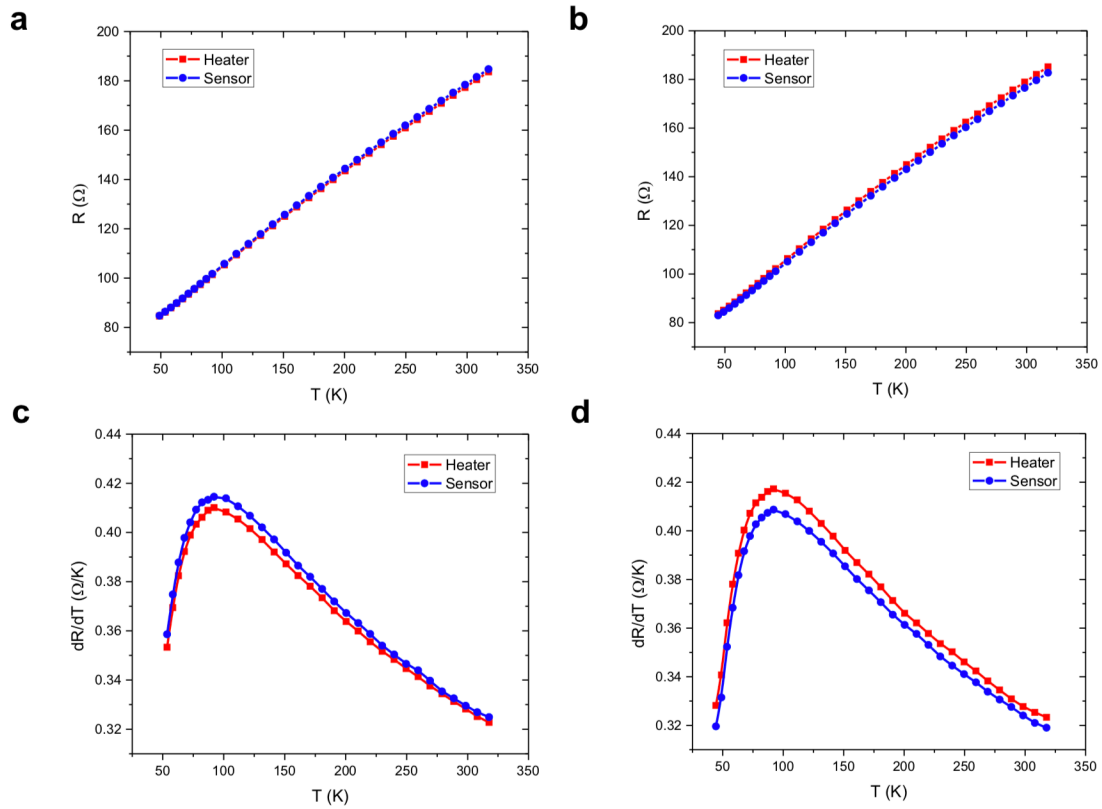
FIGURE A.11. a) and b) show the electrical resistance of the heater and sensor lines as a function of temperature for the two different measuring configura- tions, i.e. before and after being swapped. c) and d) show dR/dT versus temperature for the heater (red symbols) and the sensor (blue symbols) obtained from a) and b), respectively.
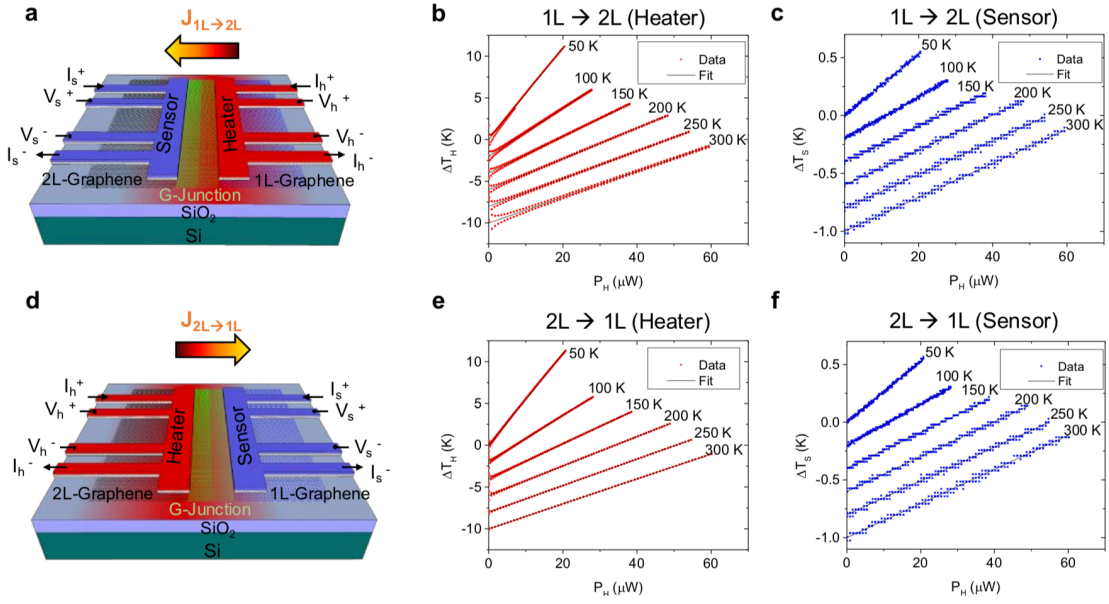
89
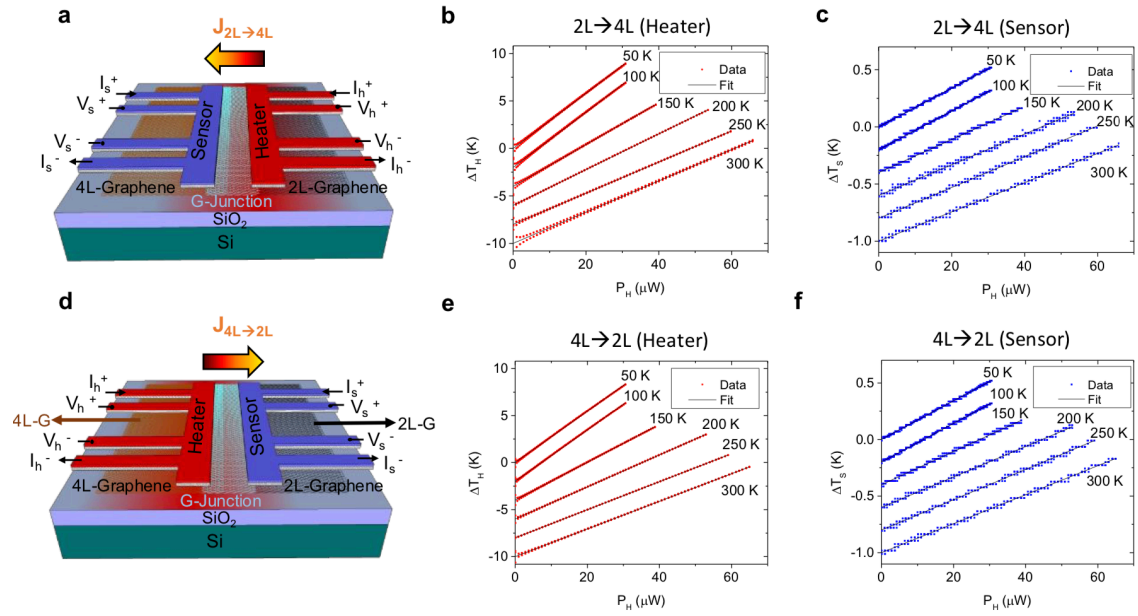
FIGURE A.12. a) Schematic drawing for the first measuring configuration, where the heat flows from 2L to 4L graphene. b) and c) show the temperature var- iation of the heater, ΔT_H, and sensor, ΔT_S, when sweeping the heater power for different tempera- tures, respectively. d) Schematic drawing for the second measuring configuration, where the heater and sensor are swapped and the heat flows now from 4L to 2L graphene. e) and f) shows ΔT_H and ΔT_S, vs heater power for different temperatures in this configuration, respectively.
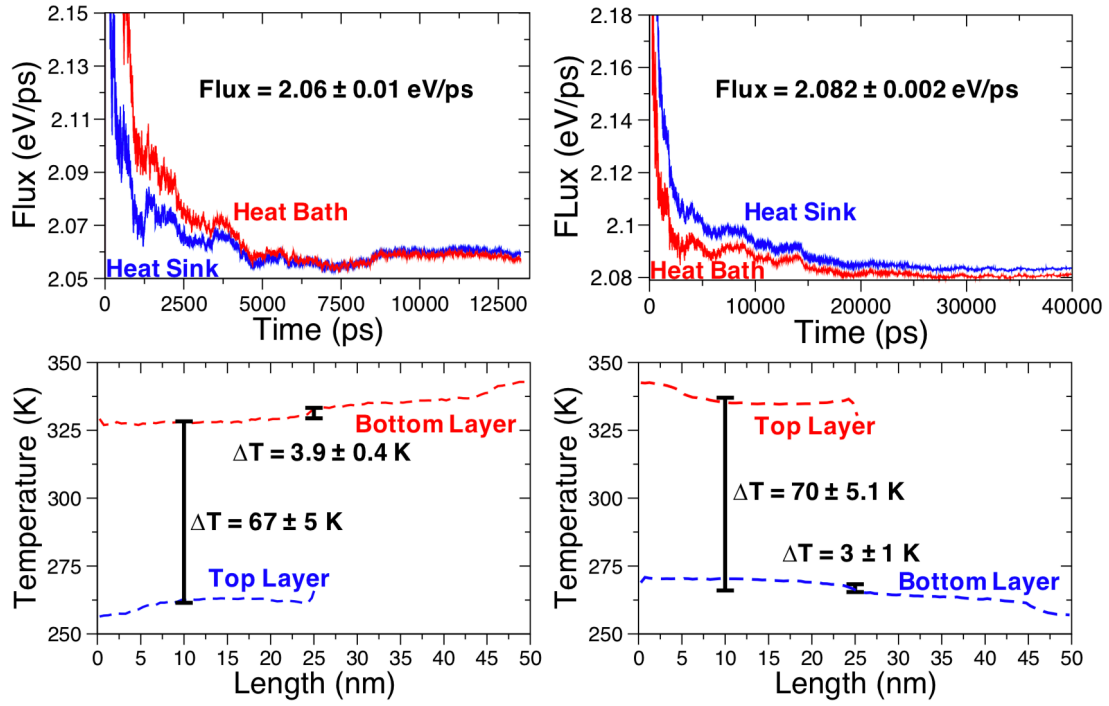
FIGURE A.13. Heat flux in the direction from the bottom layer to top layer (top left plot). Heat flux in the direction from top layer to bottom layer (top right plot). Temperature profile of multilayer graphene junction with heat flux in the direction from bottom layer to top layer (bottom left plot). Temperature profile of multilayer graphene junction with heat flux in the direction from top layer to bottom layer (bottom right). The relaxation time was set to 1 ps for this trial.
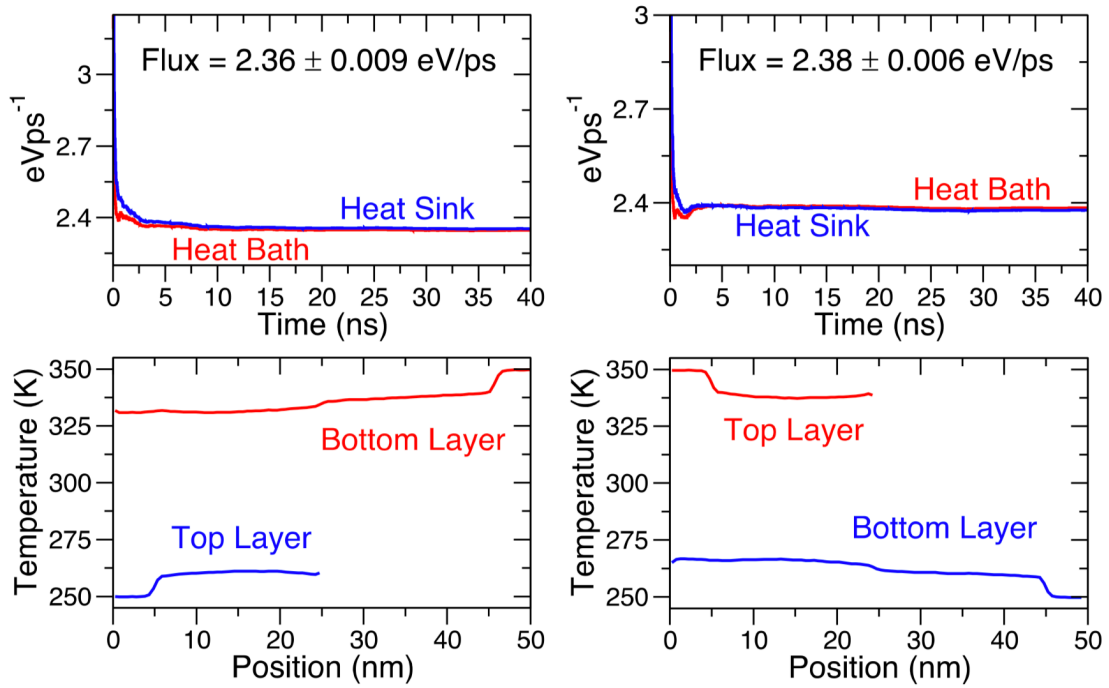
FIGURE A.14. Similar set of plots as in Figure S13 but in this case the thermostat relaxation time is set to 0.05 ps. The change in thermostat relaxation time ensures that the bath temperatures are reached, however artificial thermal resistance builds up at the edges of the thermostatted region. Negligible thermal rectification is observed.
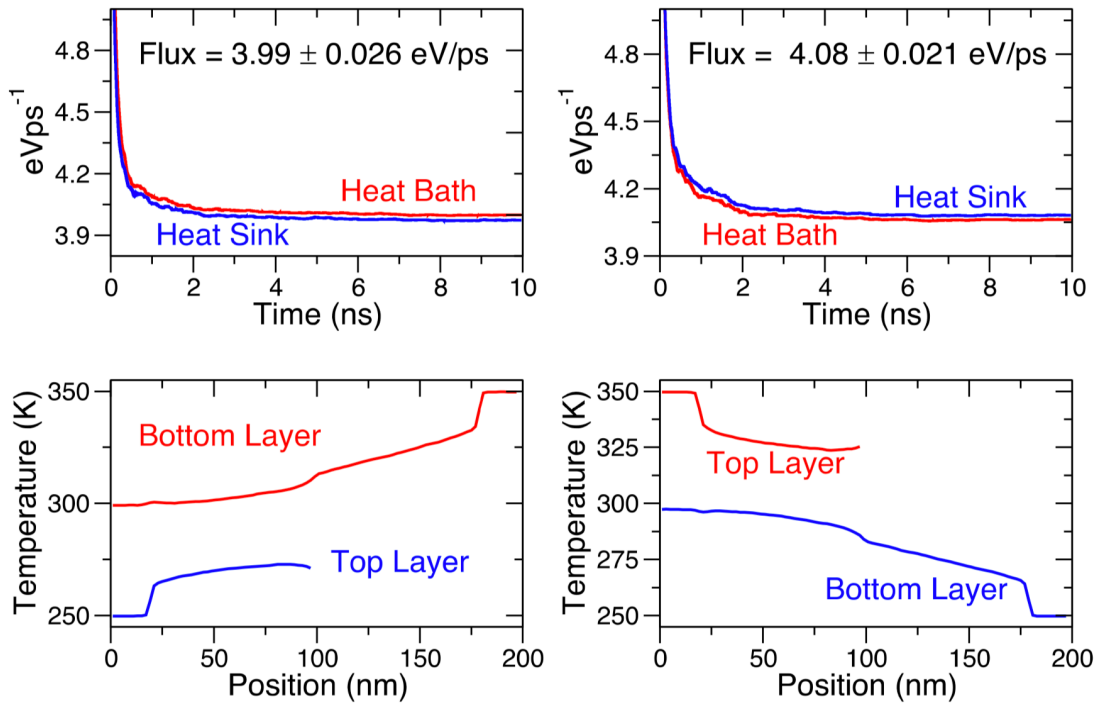
FIGURE A.15. Similar set of plots as in Figure S14 but in this case the device length is 200 nm. The length is on the same size order as the experiment. Negligible thermal rectification is observed.
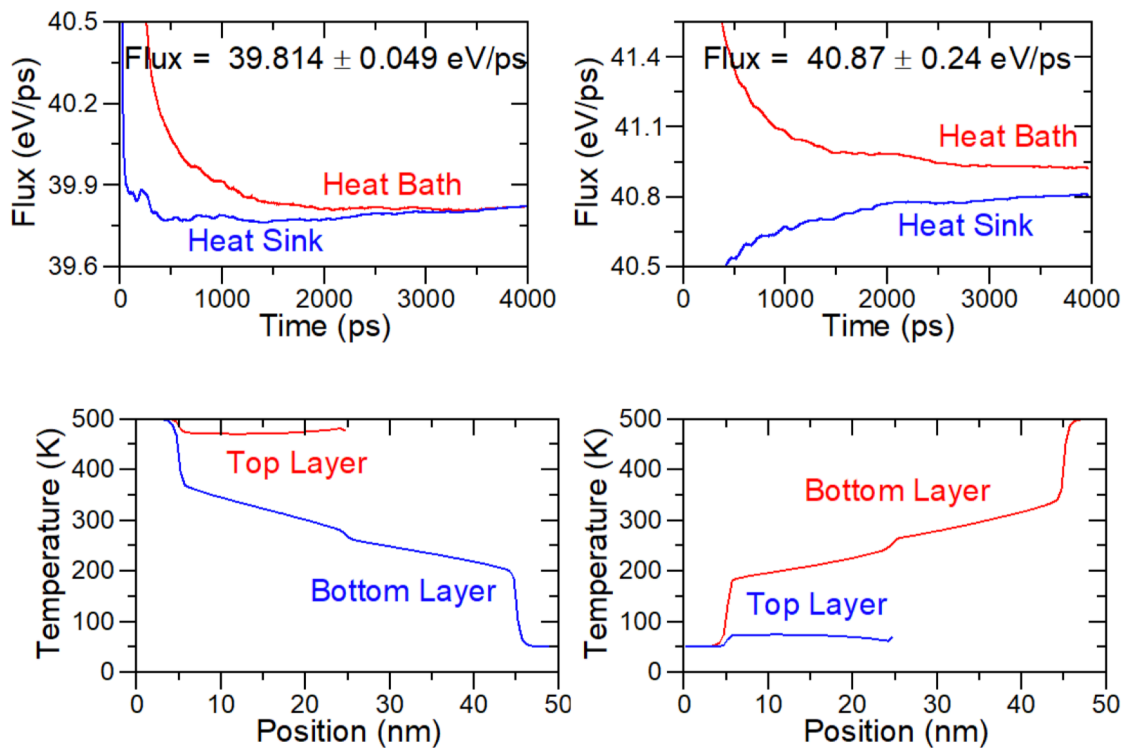
FIGURE A.16. Similar set of plots as in Figure S13 but in this case both layers are thermostated with a temperature gradient that goes from 50K to 500K. In this case, both layers are thermostated in the bilayer portion. Similar NEMD plots where obtained when only the top layer is thermostated in the bilayer region. Negligible thermal rectification is observed.
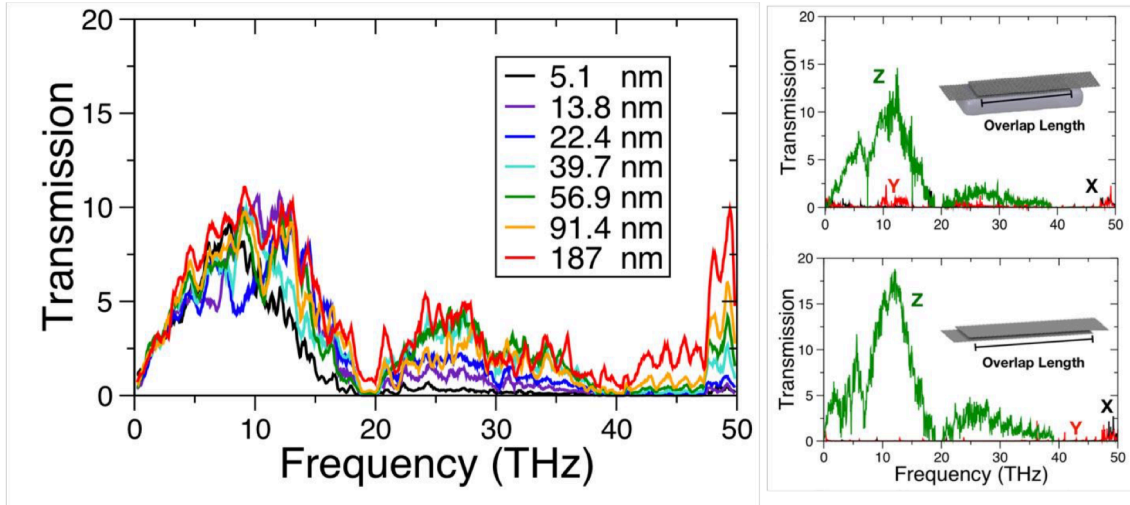
FIGURE A.17. Transmission functions for different overlap lengths overlaid one another (left). Po- larization decomposed transmission function of supported multi-layer graphene junction (top right). Polarization decomposed transmission function of suspended multilayer graphene junction (bot- tom right).

GMGMG Supplemental Figures
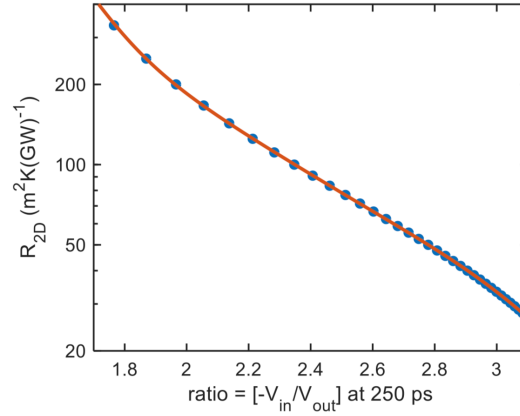
FIGURE B.1. Transfer function relating the TDTR ratio signal $(= -V_{in}/V_{out})$ at $+250$ ps to the cross-plane thermal resistance of the 2D stack at the Al/SiO_2 interface, R_{2D}. Blue points are obtained from a solution to the 3D multilayer thermal model, while the red curve is a fit to a 6th order polynomial. The multilayer stack, from top to bottom, is: Al (80 nm)/2D stack/SiO_2 (90 nm)/Si.
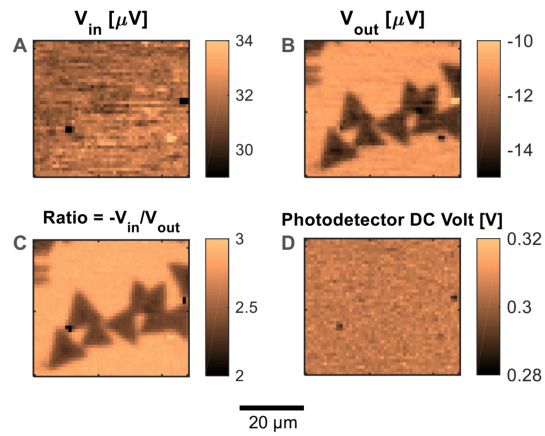
FIGURE B.2. Maps of raw TDTR signals showing the (A) in-phase voltage V_{in}, (B) out-of-phase voltage V_{out}, (C) ratio = -V_{in}/V_{out}, and (D) DC probe reflectivity measured by the photodetector. Signals (A)-(C) are at a probe delay time of +250 ps. Because the sample is coated by an optically-opaque Al transducer layer, the DC probe reflectivity is uniform. Variations in the thermal resistance of the 2D interface between Al and SiO_2 appear largely as variations in the out-of-phase voltage (and thus the ratio). The ratio signal is converted to thermal resistance of the 2D interface using the transfer curve shown in Fig. S1.
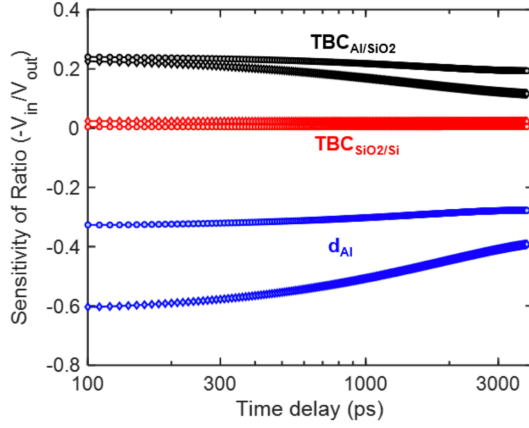
FIGURE B.3. Sensitivity of the TDTR ratio signal to various parameters. TBC is the thermal boundary conductance = $(thermal boundary resistance)^{-1}$. The sensitivity coefficient for a parameter α is calculated as: $S\alpha = \frac{\partial log(Ratio)}{\partial log(\alpha)}$, where Ratio = $-V_{in}/V_{out}$. Here, we examine the sensitivity to three parameters: (1) TBC at the Al/SiO_2 interface, which is equal to (R_{2D})-1, and is the quantity we are interested in measuring (black markers), (2) TBC at the SiO_2/Si interface (red markers), and (3) Al transducer thickness (blue markers). Two sets of curves are plotted for extreme values of R_{2D}: diamonds for $R_{2D} = 50\ m^2K(GW)^{-1}$, circles for $R_{2D} = 200\ m^2K(GW)^{-1}$.

FIGURE B.4. Cross sectional transmission electron micrograph (TEM) of a GMMG region in sample D2. The thickness of the Al transducer is 80 ± 2 nm (error bars based on the root-mean-square variation in thickness). The Ir and Pt layers are deposited during TEM sample preparation.
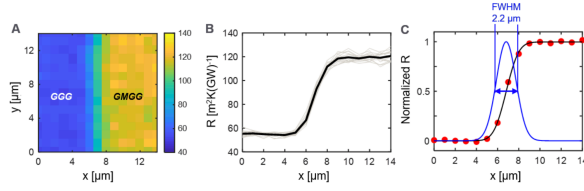
FIGURE B.5. Spatial resolution of TDTR thermal resistance microscopy. (A) Thermal resistance map across a sharp junction between regions of the sample with GGG and GMGG stacking, i.e. the region on the right side has an additional MoS_2 monolayer inserted between the first two graphene layers. (B) Horizontal line cuts taken at 15 locations on the map (light grey) and the average of these line cuts (solid black). (C) Error function fit (black curve) of the average line cut data (red markers). Derivative of the error function curve gives a Gaussian (blue curve) with full-width half-maximum (FWHM) spatial resolution of 2.2 m.
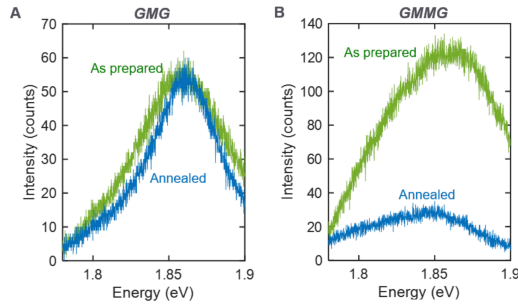
FIGURE B.6. MoS_2 photoluminescence (PL) point spectra of (A) GMG and (B) GMMG regions of sample D2, showing the effect of annealing at 350°C for 3 hours under high vacuum (7 Torr). No PL quenching is observed in GMG suggesting that annealing does not significantly modify the electronic coupling between graphene and MoS_2. In GMMG, the PL intensity is initially twice that in GMG, and is quenched upon annealing, due to the enhanced electronic coupling between the two MoS_2 monolayers.
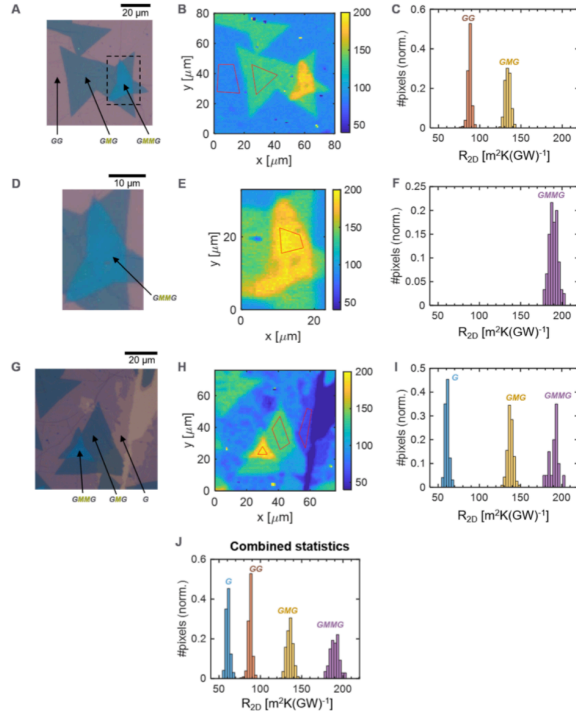
FIGURE B.7. Comprehensive data on sample D1, showing optical micrographs, TDTR thermal resistance maps, and statistics. Regions of interest (ROIs) based on which the histograms are plotted are marked by the red polygons on the TDTR maps. (A)-(C) Region 1, providing data on GG and GMG regions. (D)-(F) Region 2, which zooms into the area enclosed within the dashed lines in (A), providing high-resolution data on GMMG. This TDTR map is measured with a step size of 500 nm. (G)-(I) Region 3, providing data on G, GMG, and GMMG. (J) Combined statistics taken from all 3 regions. In (C), (F), (I), and (J), each distribution is normalized by the number of pixels in the ROI.
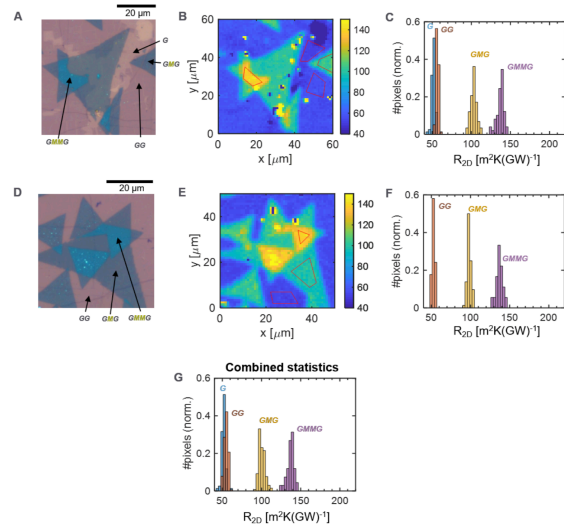
FIGURE B.8. Comprehensive data on sample D2, showing optical micrographs, TDTR thermal resistance maps, and statistics. Regions of interest (ROIs) based on which the histograms are plotted are marked by the red polygons on the TDTR maps. (A)-(C) Region 1, providing data on G, GG, GMG and GMMG regions. (D)-(F) Region 2, providing data on GG, GMG and GMMG regions. (G) Combined statistics taken from both regions. In (C), (F), and (G), each distribution is normalized by the number of pixels in the ROI.
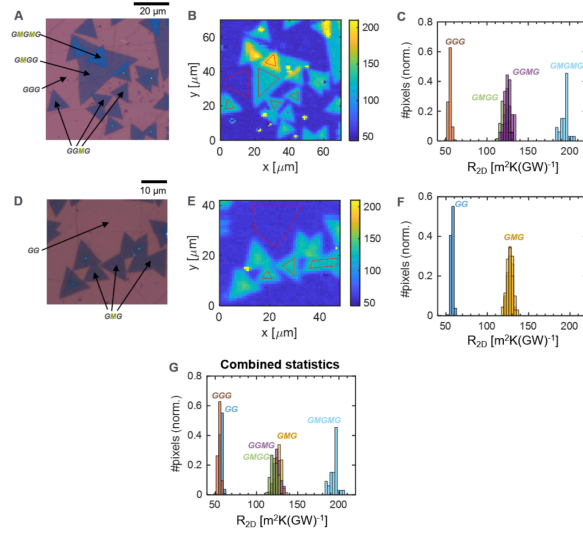
FIGURE B.9. Comprehensive data on sample D3, showing optical micrographs, TDTR thermal resistance maps, and statistics. Regions of interest (ROIs) based on which the histograms are plotted are marked by the red polygons on the TDTR maps. (A)-(C) Region 1, providing data on GGG, GGMG, GMGG, and GMGMG regions. (D)-(F) Region 2, providing data on GG and GMG regions. (G) Combined statistics taken from both regions. In (C), (F), and (G), each distribution is normalized by the number of pixels in the ROI.
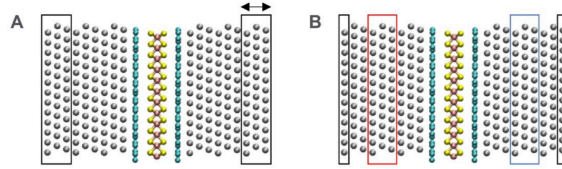
FIGURE B.10. Simulation configurations. Grey atoms are aluminum, cyan atoms are carbon, pink atoms are molybdenum, yellow atoms are sulfur. Black boxes represent fixed atoms during calculations. (A) During QHA FEM the outer three layers of aluminum are fixed. The set of fixed atoms to the right of the device are displaced relative to the rest of the device to relax the cell (indicated by a double-headed arrow). (B) During NEMD, the outermost layer of aluminum on either side is fixed. The atoms in the red box represent the heat source which was set to 350 K and the blue atoms are the heat sink which are thermostatted to 250 K using a Langevin thermostat. The rest of the device was run in the NVE ensemble.
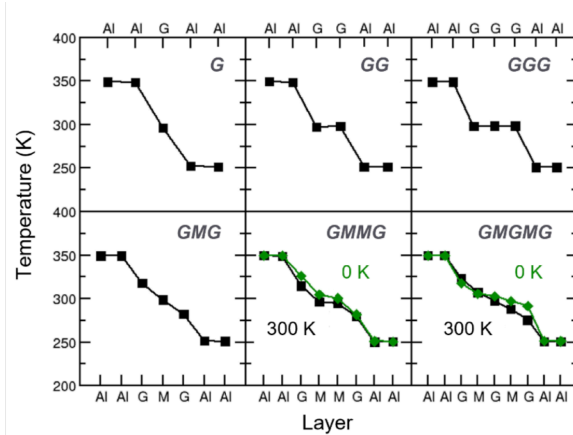
FIGURE B.11. Temperature profiles averaged over the last 500 ps of each NEMD simulation (with 10 fs intervals). Each device shows large jumps in the temperature profile at the Al-G interfaces indicating a larger resistance at these interfaces. The GG and GGG systems exhibit relatively low G-G interfacial resistances compared to the Al-G interfaces, which is to be expected of homo vs. heterojunctions. The GMMG shows that the M-M homojunction exhibits lesser resistance than either the Al-G or G-M heterojunctions. The GMMG and GMGMG devices also have their 0 K optimized structures run at the same NEMD conditions for reference to see the effects of thermal expansion. We see that for GMGMG, as the device expands, the resistances of the G-M interfaces grow relative to the Al-G interfaces, however, for GMMG this is not as clearly the case. As the devices expand, the G and M layers become thermally decoupled from one another, which contributes to an increase in the overall thermal resistance.

Bibliography

[1] *The Analytical Theory of Heat - Scholar's Choice Edition.* Creative Media Partners, LLC, 2015. [Online]. Available: https://books.google.com/books?id=TEE8rgEACAAJ

[2] C. W. Chang, D. Okawa, H. Garcia, A. Majumdar, and A. Zettl, "Breakdown of fourier's law in nanotube thermal conductors," *Phys. Rev. Lett.*, vol. 101, p. 075903, Aug 2008. [Online]. Available: https://link.aps.org/doi/10.1103/PhysRevLett.101.075903

[3] A. Dhar, "Heat transport in low-dimensional systems," *Advances in Physics*, vol. 57, no. 5, pp. 457–537, Sep. 2008. [Online]. Available: http://www.tandfonline.com/doi/abs/10.1080/00018730802538522

[4] E. Pop, "Energy dissipation and transport in nanoscale devices," *Nano Research*, vol. 3, no. 3, pp. 147–169, 2010.

[5] G. Zhu, J. Liu, Q. Zheng, R. Zhang, D. Li, D. Banerjee, and D. G. Cahill, "Tuning thermal conductivity in molybdenum disulfide by electrochemical intercalation," *Nature Communications*, vol. 7, p. 13211, 2016.

[6] X. Qian, X. Gu, M. S. Dresselhaus, and R. Yang, "Anisotropic tuning of graphite thermal conductivity by lithium intercalation," *The Journal of Physical Chemistry Letters*, vol. 7, pp. 4744–4750, 11 2016, doi: 10.1021/acs.jpclett.6b02295. [Online]. Available: https://doi.org/10.1021/acs.jpclett.6b02295

[7] C. Wan, X. Gu, F. Dang, T. Itoh, Y. Wang, H. Sasaki, M. Kondo, K. Koga, K. Yabuki, G. J. Snyder, R. Yang, and K. Koumoto, "Flexible n-type thermoelectric materials by organic intercalation of layered transition metal dichalcogenide tis2," *Nature Materials*, vol. 14, pp. 622–627, 2015. [Online]. Available: https://doi.org/10.1038/nmat4251

[8] K. S. Novoselov, A. K. Geim, S. V. Morozov, D. Jiang, Y. Zhang, S. V. Dubonos, I. V. Grigorieva, and A. A. Firsov, "Electric field effect in atomically thin carbon films," *Science*, vol. 306, no. 5696, pp. 666–669, 2004. [Online]. Available: https://www.science.org/doi/abs/10.1126/science.1102896

[9] A. A. Balandin, S. Ghosh, W. Bao, I. Calizo, D. Teweldebrhan, F. Miao, and C. N. Lau, "Superior thermal conductivity of single-layer graphene," *Nano Letters*, vol. 8, no. 3, pp. 902–907, 2008. [Online]. Available: http://dx.doi.org/10.1021/nl0731872

[10] N. Wang, Y. Liu, L. Ye, and J. Li, "Highly thermal conductive and light-weight graphene-based heatsink," in *2019 22nd European Microelectronics and Packaging Conference Exhibition (EMPC)*, 2019, pp. 1–4.

[11] D. Singh, J. Y. Murthy, and T. S. Fisher, "Mechanism of thermal conductivity reduction in few-layer graphene," *Journal of Applied Physics*, vol. 110, no. 4, p. 044317, 2011. [Online]. Available: https://doi.org/10.1063/1.3622300

[12] S. Ghosh, W. Bao, D. L. Nika, S. Subrina, E. P. Pokatilov, C. N. Lau, and A. A. Balandin, "Dimensional crossover of thermal transport in few-layer graphene," *Nature Materials*, vol. 9, pp. 555–558, 2010. [Online]. Available: https://doi.org/10.1038/nmat2753

[13] K. F. Mak, C. Lee, J. Hone, J. Shan, and T. F. Heinz, "Atomically thin mos2: A new direct-gap semiconductor," *Physical Review Letters*, vol. 105, p. 136805, 2010.

[14] B. Radisavljevic, A. Radenovic, J. Brivio, V. Giacometti, and A. Kis, "Single-layer mos2 transistors," *Nature Nanotechnology*, vol. 6, pp. 147–150, 2011.

[15] E. Pop, V. Varshney, and A. K. Roy, "Thermal properties of graphene: Fundamentals and applications," *MRS Bulletin*, vol. 37, no. 12, pp. 1273–1281, 12 2012.

[16] J. Wang, F. Xie, X.-H. Cao, S.-C. An, W.-X. Zhou, L.-M. Tang, and K.-Q. Chen, "Excellent thermoelectric properties in monolayer wse2 nanoribbons due to ultralow phonon thermal conductivity," *Scientific Reports*, vol. 7, p. 41418, 2017. [Online]. Available: https://doi.org/10.1038/srep41418

[17] A. Sood, F. Xiong, S. Chen, R. Cheaito, F. Lian, M. Asheghi, Y. Cui, D. Donadio, K. E. Goodson, and E. Pop, "Quasi-ballistic thermal transport across mos2 thin films," *Nano Letters*, vol. 19, no. 4, pp. 2434–2442, 2019.

[18] A. Sood, F. Xiong, S. Chen, H. Wang, D. Selli, J. Zhang, C. J. McClellan, J. Sun, D. Donadio, Y. Cui, E. Pop, and K. E. Goodson, "An electrochemical thermal transistor," *Nature Communications*, vol. 9, p. 4510, 2018.

[19] "Thermal conductivity and phonon hydrodynamics in transition metal dichalcogenides from first-principles," vol. 6, p. 35002, 4 2019. [Online]. Available: https://doi.org/10.1088/2053-1583/ab0c31

[20] Y. Zhu, X. Fan, B. Liang, J. Cheng, and Y. Jing, "Ultrathin acoustic metasurface-based schroeder diffuser," *Phys. Rev. X*, vol. 7, p. 021034, Jun 2017. [Online]. Available: https://link.aps.org/doi/10.1103/PhysRevX.7.021034

[21] M. Maldovan, "Sound and heat revolutions in phononics," *Nature*, vol. 503, pp. 209–217, 2013. [Online]. Available: https://doi.org/10.1038/nature12608

[22] S. Volz, J. Ordonez-Miranda, A. Shchepetov, M. Prunnila, J. Ahopelto, T. Pezeril, G. Vaudel, V. Gusev, P. Ruello, E. M. Weig, M. Schubert, M. Hettich, M. Grossman, T. Dekorsy, F. Alzina, B. Graczykowski, E. Chavez-Angel, J. Sebastian Reparaz, M. R. Wagner, C. M. Sotomayor Torres, S. Xiong, S. Neogi, and D. Donadio, "Nanophononics: state of the art and perspectives," *Eur Phys J B*, vol. 89, no. 1, p. 15, Jan. 2016.

[23] N. Li, J. Ren, L. Wang, G. Zhang, P. Hänggi, and B. Li, "Colloquium," *Rev. Mod. Phys.*, vol. 84, pp. 1045–1066, Jul 2012. [Online]. Available: https://link.aps.org/doi/10.1103/RevModPhys.84.1045

[24] B. Li, L. Wang, and G. Casati, "Thermal Diode: Rectification of Heat Flux," *Phys. Rev. Lett.*, vol. 93, no. 18, p. 184301, Oct. 2004. [Online]. Available: https://link.aps.org/doi/10.1103/PhysRevLett.93.184301

[25] M. Terraneo, M. Peyrard, and G. Casati, "Controlling the Energy Flow in Nonlinear Lattices: A Model for a Thermal Rectifier," *Phys. Rev. Lett.*, vol. 88, no. 9, pp. 094 302–4, Feb. 2002. [Online]. Available: https://link.aps.org/doi/10.1103/PhysRevLett.88.094302

[26] S. Chen, E. Pereira, and G. Casati, "Ingredients for an efficient thermal diode," *EPL*, vol. 111, no. 3, p. 30004, Aug. 2015. [Online]. Available: https://doi.org/10.1209%2F0295-5075%2F111%2F30004

[27] S. Chen, D. Donadio, G. Benenti, and G. Casati, "Efficient thermal diode with ballistic spacer," *Phys. Rev. E*, vol. 97, no. 3, p. 030101, Mar. 2018. [Online]. Available: https://link.aps.org/doi/10.1103/PhysRevE.97.030101

[28] G. Benenti, G. Casati, C. Mejía-Monasterio, and M. Peyrard, "From Thermal Rectifiers to Thermoelectric Devices," in *Thermal Transport in Low Dimensions: From Statistical Physics to Nanoscale Heat Transfer*, ser. Lecture Notes in Physics, S. Lepri, Ed. Cham: Springer International Publishing, 2016, pp. 365–407. [Online]. Available: https://doi.org/10.1007/978-3-319-29261-8_10

[29] Z. Li, S. Xiong, C. Sievers, Y. Hu, Z. Fan, N. Wei, H. Bao, S. Chen, D. Donadio, and T. Ala-Nissila, "Influence of thermostatting on nonequilibrium molecular dynamics simulations of heat conduction in solids," *The Journal of Chemical Physics*, vol. 151, no. 23, p. 234105, 2019. [Online]. Available: https://doi.org/10.1063/1.5132543

[30] Y. Cao, V. Fatemi, S. Fang, K. Watanabe, T. Taniguchi, E. Kaxiras, and P. Jarillo-Herrero, "Unconventional superconductivity in magic-angle graphene superlattices," *Nature*, vol. 556, pp. 43–50, 2018. [Online]. Available: https://doi.org/10.1038/nature26160

[31] A. I. Cocemasov, D. L. Nika, and A. A. Balandin, "Phonons in twisted bilayer graphene," *Phys. Rev. B*, vol. 88, p. 035428, Jul 2013. [Online]. Available: https://link.aps.org/doi/10.1103/PhysRevB.88.035428

[32] W. Ouyang, H. Qin, M. Urbakh, and O. Hod, "Controllable thermal conductivity in twisted homogeneous interfaces of graphene and hexagonal boron nitride," *Nano Letters*, vol. 20, pp. 7513–7518, 10 2020, doi: 10.1021/acs.nanolett.0c02983. [Online]. Available: https://doi.org/10.1021/acs.nanolett.0c02983

[33] N. N. T. Nam and M. Koshino, "Lattice relaxation and energy band modulation in twisted bilayer graphene," *Phys. Rev. B*, vol. 96, p. 075311, Aug 2017. [Online]. Available: https://link.aps.org/doi/10.1103/PhysRevB.96.075311

[34] M. Lamparski, B. V. Troeye, and V. Meunier, "Soliton signature in the phonon spectrum of twisted bilayer graphene," vol. 7, p. 25050, 3 2020. [Online]. Available: https://doi.org/10.1088/2053-1583/ab7874

[35] R. Peierls, "Zur kinetischen theorie der wärmeleitung in kristallen," *Annalen der Physik*, vol. 395, no. 8, pp. 1055–1101, 1929. [Online]. Available: https://onlinelibrary.wiley.com/doi/abs/10.1002/andp.19293950803

[36] P. Hohenberg and W. Kohn, "Inhomogeneous electron gas," *Phys. Rev.*, vol. 136, pp. B864–B871, Nov 1964. [Online]. Available: https://link.aps.org/doi/10.1103/PhysRev.136.B864

[37] W. Kohn and L. J. Sham, "Self-consistent equations including exchange and correlation effects," *Phys. Rev.*, vol. 140, pp. A1133–A1138, Nov 1965. [Online]. Available: https://link.aps.org/doi/10.1103/PhysRev.140.A1133

[38] M. Omini and A. Sparavigna, "Beyond the isotropic-model approximation in the theory of thermal conductivity," *Phys. Rev. B*, vol. 53, pp. 9064–9073, Apr 1996. [Online]. Available: https://link.aps.org/doi/10.1103/PhysRevB.53.9064

[39] A. Ward, D. A. Broido, D. A. Stewart, and G. Deinzer, "Ab initio theory of the lattice thermal conductivity in diamond," *Phys. Rev. B*, vol. 80, p. 125203, Sep 2009. [Online]. Available: https://link.aps.org/doi/10.1103/PhysRevB.80.125203

[40] L. Chaput, A. Togo, I. Tanaka, and G. Hug, "Phonon-phonon interactions in transition metals," *Phys. Rev. B*, vol. 84, p. 094302, Sep 2011. [Online]. Available: https://link.aps.org/doi/10.1103/PhysRevB.84.094302

[41] W. Li, J. Carrete, N. A. Katcho, and N. Mingo, "Shengbte: A solver of the boltzmann transport equation for phonons," *Computer Physics Communications*, vol. 185, pp. 1747–1758, 2014.

[42] G. Fugallo, M. Lazzeri, L. Paulatto, and F. Mauri, "Ab initio variational approach for evaluating lattice thermal conductivity," *Phys. Rev. B*, vol. 88, p. 045430, Jul 2013. [Online]. Available: https://link.aps.org/doi/10.1103/PhysRevB.88.045430

[43] A. Cepellotti and N. Marzari, "Thermal transport in crystals as a kinetic theory of relaxons," *Phys. Rev. X*, vol. 6, p. 041013, Oct 2016. [Online]. Available: https://link.aps.org/doi/10.1103/PhysRevX.6.041013

[44] L. Isaeva, G. Barbalinardo, D. Donadio, and S. Baroni, "Modeling heat transport in crystals and glasses from a unified lattice-dynamical approach," *Nature Communications*, vol. 10, p. 3853, 2019. [Online]. Available: https://doi.org/10.1038/s41467-019-11572-4

[45] N. Mingo and L. Yang, "Phonon transport in nanowires coated with an amorphous material: An atomistic green's function approach," *Phys. Rev. B*, vol. 68, p. 245406, Dec 2003. [Online]. Available: https://link.aps.org/doi/10.1103/PhysRevB.68.245406

[46] Y. Imry and R. Landauer, "Conductance viewed as transmission," *Rev. Mod. Phys.*, vol. 71, no. 2, pp. S306–S312, 1999. [Online]. Available: https://link.aps.org/doi/10.1103/RevModPhys.71.S306

[47] D. A. Young and H. J. Maris, "Lattice-dynamical calculation of the Kapitza resistance between fcc lattices," *Phys. Rev. B*, vol. 40, no. 6, pp. 3685–3693, Aug. 1989. [Online]. Available: https://link.aps.org/doi/10.1103/PhysRevB.40.3685

[48] D. G. Cahill *et al.*, "Nanoscale thermal transport. ii. 2003–2012," *Applied Physics Reviews*, vol. 1, no. 1, p. 011305, 2014. [Online]. Available: https://doi.org/10.1063/1.4832615

[49] S. Volz, J. Ordonez-Miranda, A. Shchepetov, M. Prunnila, J. Ahopelto, T. Pezeril, G. Vaudel, V. Gusev, P. Ruello, E. M. Weig, M. Schubert, M. Hettich, M. Grossman, T. Dekorsy, F. Alzina, B. Graczykowski, E. Chavez-Angel, J. Sebastian Reparaz, M. R. Wagner, C. M. Sotomayor-Torres, S. Xiong, S. Neogi, and D. Donadio, "Nanophononics: state of the art and perspectives," *The European Physical Journal B*, vol. 89, p. 15, 2016.

[50] D. Donadio, "Thermal transport: Overview," in *Handbook of Materials Modeling: Applications: Current and Emerging Materials*, S. Yip, Ed.   Springer, 2018, pp. 1–11.

[51] A. Marcolongo, P. Umari, and S. Baroni, "Microscopic theory and quantum simulation of atomic heat transport," *Nature Phys*, vol. 12, no. 1, pp. 80–84, Oct. 2015. [Online]. Available: https://www.nature.com/articles/nphys3509

[52] C. Carbogno, R. Ramprasad, and M. Scheffler, "Ab initio green-kubo approach for the thermal conductivity of solids," *Phys. Rev. Lett.*, vol. 118, p. 175901, Apr 2017. [Online]. Available: https://link.aps.org/doi/10.1103/PhysRevLett.118.175901

[53] J. Kang and L.-W. Wang, "First-principles green-kubo method for thermal conductivity calculations," *Phys. Rev. B*, vol. 96, p. 020302, Jul 2017. [Online]. Available: https://link.aps.org/doi/10.1103/PhysRevB.96.020302

[54] S. Stackhouse, L. Stixrude, and B. B. Karki, "Thermal conductivity of periclase (mgo) from first principles," *Phys. Rev. Lett.*, vol. 104, p. 208501, May 2010. [Online]. Available: https://link.aps.org/doi/10.1103/PhysRevLett.104.208501

[55] M. Puligheddu, F. Gygi, and G. Galli, "First-principles simulations of heat transport," *Phys. Rev. Materials*, vol. 1, p. 060802, Nov 2017. [Online]. Available: https://link.aps.org/doi/10.1103/PhysRevMaterials.1.060802

[56] E. Martin, P. L. Palla, F. Cleri, A. Bouzid, G. Ori, S. L. Roux, M. Boero, and C. Massobrio, "On the occurrence of size effects in the calculation of thermal conductivity by first-principles molecular dynamics: The case of glassy gete4," *Journal of Non-Crystalline Solids*, vol. 498, pp. 190 – 193, 2018. [Online]. Available: http://www.sciencedirect.com/science/article/pii/S0022309318302904

[57] O. N. Bedoya-Martínez, J.-L. Barrat, and D. Rodney, "Computation of the thermal conductivity using methods based on classical and quantum molecular dynamics," *Phys. Rev. B*, vol. 89, p. 014303, Jan 2014. [Online]. Available: https://link.aps.org/doi/10.1103/PhysRevB.89.014303

[58] M. P. Allen and D. J. Tildesley, *Computer Simulation of Liquids,* 2nd Ed.   USA: Clarendon Press, 2017.

[59] R. W. Hockney, "Potential calculation and some applications." *Methods Comput. Phys. 9: 135-211(1970).*, vol. 9, 1 1970. [Online]. Available: https://www.osti.gov/biblio/4079632

[60] W. C. Swope, H. C. Andersen, P. H. Berens, and K. R. Wilson, "A computer simulation method for the calculation of equilibrium constants for the formation of physical clusters of molecules: Application to small water clusters," *The Journal of Chemical Physics*, vol. 76, no. 1, pp. 637–649, 1982. [Online]. Available: http://dx.doi.org/10.1063/1.442716

[61]

[62] J. Tersoff, "New empirical model for the structural properties of silicon," *Phys. Rev. Lett.*, vol. 56, pp. 632–635, Feb 1986. [Online]. Available: https://link.aps.org/doi/10.1103/PhysRevLett.56.632

[63] ——, "Empirical interatomic potential for carbon, with applications to amorphous carbon," *Phys. Rev. Lett.*, vol. 61, pp. 2879–2882, Dec 1988. [Online]. Available: https://link.aps.org/doi/10.1103/PhysRevLett.61.2879

[64] L. Lindsay and D. A. Broido, "Optimized tersoff and brenner empirical potential parameters for lattice dynamics and phonon thermal transport in carbon nanotubes and graphene," *Phys. Rev. B*, vol. 81, p. 205441, May 2010. [Online]. Available: https://link.aps.org/doi/10.1103/PhysRevB.81.205441

[65] M. M. Rojo, Z. Li, C. Sievers, A. C. Bornstein, E. Yalon, S. Deshmukh, S. Vaziri, M.-H. Bae, F. Xiong, D. Donadio, and E. Pop, "Thermal transport across graphene step junctions," *2D Mater.*, vol. 6, no. 1, p. 011005, Jan. 2019. [Online]. Available: https://doi.org/10.1088%2F2053-1583%2Faae7ea

[66] X. Xu, L. F. C. Pereira, Y. Wang, J. Wu, K. Zhang, X. Zhao, S. Bae, C. Tinh Bui, R. Xie, J. T. L. Thong, B. H. Hong, K. P. Loh, D. Donadio, B. Li, and B. Özyilmaz, "Length-dependent thermal conductivity in suspended single-layer graphene," *Nature Commun.*, vol. 5, p. 3689, Apr. 2014. [Online]. Available: https://www.nature.com/articles/ncomms4689

[67] A. N. Kolmogorov and V. H. Crespi, "Smoothest bearings: Interlayer sliding in multiwalled carbon nanotubes," *Phys. Rev. Lett.*, vol. 85, pp. 4727–4730, Nov 2000. [Online]. Available: https://link.aps.org/doi/10.1103/PhysRevLett.85.4727

[68] ——, "Registry-dependent interlayer potential for graphitic systems," *Physical Review B*, vol. 71, p. 235415, 2005.

[69] M. H. Naik, I. Maity, P. K. Maiti, and M. Jain, "Kolmogorov–crespi potential for multilayer transition-metal dichalcogenides: Capturing structural transformations in moiré superlattices," *The Journal of Physical Chemistry C*, vol. 123, pp. 9770–9778, 4 2019, doi: 10.1021/acs.jpcc.8b10392. [Online]. Available: https://doi.org/10.1021/acs.jpcc.8b10392

[70] S. Nosè, "A unified formulation of the constant temperature molecular dynamics methods," *J. Chem. Phys.*, vol. 81, no. 1, pp. 511–519, 1984. [Online]. Available: https://doi.org/10.1063/1.447334

[71] H. C. Andersen, "Molecular dynamics simulations at constant pressure and/or temperature," *The Journal of Chemical Physics*, vol. 72, no. 4, pp. 2384–2393, 1980. [Online]. Available: https://doi.org/10.1063/1.439486

[72] S. Lepri, R. Livi, and A. Politi, "Thermal conduction in classical low-dimensional lattices," *Physics Reports*, vol. 377, no. 1, pp. 1–80, Apr. 2003. [Online]. Available: http://www.sciencedirect.com/science/article/pii/S0370157302005586

[73] S. Stackhouse and L. Stixrude, "Theoretical methods for calculating the lattice thermal conductivity of minerals," *Reviews in Mineralogy and Geochemistry*, vol. 71, p. 253, 2010.

[74] J. Shiomi, "Nonequilirium molecular dynamics methods for lattice heat conduction calculations," *Annual Review of Heat Transfer*, vol. 17, p. 177, 2014.

[75] S. Datta, *Electonic transport in mesoscopic systems*. Cambridge University Press, 1995.

[76] I. Errea, M. Calandra, and F. Mauri, "Anharmonic free energies and phonon dispersions from the stochastic self-consistent harmonic approximation: Application to platinum and palladium hydrides," *Physical Review B*, vol. 89, p. 064302, 2014.

[77] A. Sood, C. Sievers, Y. C. Shin, V. Chen, S. Chen, K. K. H. Smithe, S. Chatterjee, D. Donadio, K. E. Goodson, and E. Pop, "Engineering thermal transport across layered graphene–mos2 superlattices," *ACS Nano*, vol. 0, no. 0, p. null, 0, pMID: 34813267. [Online]. Available: https://doi.org/10.1021/acsnano.1c06299

[78] I. Duchemin and D. Donadio, "Atomistic calculation of the thermal conductance of large scale bulk-nanowire junctions," *Physical Review B*, vol. 84, no. 11, p. 115423, 9 2011.

[79] S. Ghosh, I. Calizo, D. Teweldebrhan, E. P. Pokatilov, D. L. Nika, A. A. Balandin, W. Bao, F. Miao, and C. N. Lau, *Appl. Phys. Lett.*, vol. 92, p. 151911, 2008.

[80] P. B. Allen, "Size effects in thermal conduction by phonons," *Physical Review B*, vol. 90, no. 5, p. 054301, 2014. [Online]. Available: https://link.aps.org/doi/10.1103/PhysRevB.90.054301

[81] A. Cepellotti and N. Marzari, "Boltzmann Transport in Nanostructures as a Friction Effect," *Nano Lett.*, vol. 17, no. 8, pp. 4675–4682, Jul. 2017. [Online]. Available: https://doi.org/10.1021/acs.nanolett.7b01202

[82] K. Sääskilahti, J. Oksanen, J. Tulkki, and S. Volz, "Role of anharmonic phonon scattering in the spectrally decomposed thermal conductance at planar interfaces," *Phys. Rev. B*, vol. 90, p. 134312, Oct 2014. [Online]. Available: https://link.aps.org/doi/10.1103/PhysRevB.90.134312

[83] K. Sääskilahti, J. Oksanen, S. Volz, and J. Tulkki, "Frequency-dependent phonon mean free path in carbon nanotubes from nonequilibrium molecular dynamics," *Phys. Rev. B*, vol. 91, p. 115426, Mar 2015. [Online]. Available: https://link.aps.org/doi/10.1103/PhysRevB.91.115426

[84] Z. Fan, L. F. C. Pereira, P. Hirvonen, M. M. Ervasti, K. R. Elder, D. Donadio, T. Ala-Nissila, and A. Harju, "Thermal conductivity decomposition in two-dimensional materials: Application to graphene," *Phys. Rev. B*, vol. 95, p. 144309, Apr 2017. [Online]. Available: https://link.aps.org/doi/10.1103/PhysRevB.95.144309

[85] J.-S. Wang, J. Wang, and J. T. Lü, "Quantum thermal transport in nanostructures," *The European Physical Journal B*, vol. 62, no. 4, pp. 381–404, Apr 2008.

[86] S. Sadasivam, Y. Che, Z. Huang, L. Chen, S. Kumar, and T. S. Fisher, "The atomistic green's function method for interfacial phonon transport," *Annual Review of Heat Transfer*, vol. 17, p. 89, 2014.

[87] H. Dong, Z. Fan, L. Shi, A. Harju, and T. Ala-Nissila, "Equivalence of the equilibrium and the nonequilibrium molecular dynamics methods for thermal conductivity calculations: From bulk to nanowire silicon," *Physical Review B*, vol. 97, p. 094305, 2018. [Online]. Available: https://journals.aps.org/prb/abstract/10.1103/PhysRevB.97.094305

[88] Z. Fan, H. Dong, A. Harju, and T. Ala-Nissila, "Homogeneous nonequilibrium molecular dynamics method for heat transport and spectral decomposition with many-body potentials," *Phys. Rev. B*, vol. 99, p. 064308, Feb 2019. [Online]. Available: https://link.aps.org/doi/10.1103/PhysRevB.99.064308

[89] K. Xu, Z. Fan, J. Zhang, N. Wei, and T. Ala-Nissila, "Thermal transport properties of single-layer black phosphorus from extensive molecular dynamics simulations," *Modelling and Simulation in Materials Science and Engineering*, vol. 26, no. 8, p. 085001, 2018.

110

[90] H. Dong, P. Hirvonen, Z. Fan, and T. Ala-Nissila, "Heat transport in pristine and polycrystalline single-layer hexagonal boron nitride," *Phys. Chem. Chem. Phys.*, vol. 20, pp. 24 602–24 612, 2018. [Online]. Available: http://dx.doi.org/10.1039/C8CP05159C

[91] K. Xu, A. J. Gabourie, A. Hashemi, Z. Fan, N. Wei, A. B. Farimani, H.-P. Komsa, A. V. Krasheninnikov, E. Pop, and T. Ala-Nissila, "Thermal transport in mos$_2$ from molecular dynamics using different empirical potentials," *Phys. Rev. B*, vol. 99, p. 054303, Feb 2019. [Online]. Available: https://link.aps.org/doi/10.1103/PhysRevB.99.054303

[92] C. Caroli, R. Combescot, P. Nozieres, and D. Saint-James, "Direct calculation of the tunneling current," *Journal of Physics C: Solid State Physics*, vol. 4, no. 8, p. 916, 1971. [Online]. Available: http://stacks.iop.org/0022-3719/4/i=8/a=018

[93] M. P. L. Sancho, J. M. L. Sancho, J. M. L. Sancho, and J. Rubio, "Highly convergent schemes for the calculation of bulk and surface green functions," *Journal of Physics F: Metal Physics*, vol. 15, no. 4, p. 851, 1985. [Online]. Available: http://stacks.iop.org/0305-4608/15/i=4/a=009

[94] T. Ikeshoji and B. Hafskjold, "Non-equilibrium molecular dynamics calculation of heat conduction in liquid and through liquid-gas interface," *Molecular Physics*, vol. 81, no. 2, pp. 251–261, 1994. [Online]. Available: http://dx.doi.org/10.1080/00268979400100171

[95] P. Jund and R. Jullien, "Molecular-dynamics calculation of the thermal conductivity of vitreous silica," *Phys. Rev. B*, vol. 59, pp. 13 707–13 711, Jun 1999. [Online]. Available: https://link.aps.org/doi/10.1103/PhysRevB.59.13707

[96] F. Müller-Plathe, "A simple nonequilibrium molecular dynamics method for calculating the thermal conductivity," *The Journal of Chemical Physics*, vol. 106, no. 14, pp. 6082–6085, 1997. [Online]. Available: https://doi.org/10.1063/1.473271

[97] S. Kuang and J. D. Gezelter, "A gentler approach to RNEMD: Nonisotropic velocity scaling for computing thermal conductivity and shear viscosity," *J. Chem. Phys.*, vol. 133, no. 16, p. 164101, 2010. [Online]. Available: https://aip.scitation.org/doi/10.1063/1.3499947

[98] H. J. C. Berendsen, J. P. M. Postma, W. F. van Gunsteren, A. DiNola, and J. R. Haak, "Molecular dynamics with coupling to an external bath," *The Journal of Chemical Physics*, vol. 81, no. 8, pp. 3684–3690, 1984. [Online]. Available: http://dx.doi.org/10.1063/1.448118

[99] S. Nosé, "A unified formulation of the constant temperature molecular dynamics methods," *The Journal of Chemical Physics*, vol. 81, no. 1, pp. 511–519, 1984. [Online]. Available: http://dx.doi.org/10.1063/1.447334

[100] W. G. Hoover, "Canonical dynamics: Equilibrium phase-space distributions," *Phys. Rev. A*, vol. 31, pp. 1695–1697, Mar 1985. [Online]. Available: https://link.aps.org/doi/10.1103/PhysRevA.31.1695

[101] G. J. Martyna, M. L. Klein, and M. Tuckerman, "Nosé-hoover chains: The canonical ensemble via continuous dynamics," *The Journal of Chemical Physics*, vol. 97, no. 4, pp. 2635–2643, 1992. [Online]. Available: http://dx.doi.org/10.1063/1.463940

[102] G. J. Martyna, M. E. Tuckerman, D. J. Tobias, and M. L. Klein, "Explicit reversible integrators for extended systems dynamics," *Mol. Phys.*, vol. 87, p. 1117, 1996. [Online]. Available: https://doi.org/10.1080/00268979600100761

[103] G. Bussi and M. Parrinello, "Accurate sampling using langevin dynamics," *Phys. Rev. E*, vol. 75, p. 056707, May 2007. [Online]. Available: https://link.aps.org/doi/10.1103/PhysRevE.75.056707

[104] G. Bussi, D. Donadio, and M. Parrinello, "Canonical sampling through velocity rescaling," *J. Chem. Phys.*, vol. 126, no. 1, p. 014101, 2007. [Online]. Available: https://aip.scitation.org/doi/10.1063/1.2408420

[105] Z. Fan, L. F. C. Pereira, H.-Q. Wang, J.-C. Zheng, D. Donadio, and A. Harju, "Force and heat current formulas for many-body potentials in molecular dynamics simulations with applications to thermal conductivity calculations," *Phys. Rev. B*, vol. 92, p. 094301, Sep 2015. [Online]. Available: https://link.aps.org/doi/10.1103/PhysRevB.92.094301

[106] Z. Fan, T. Siro, and A. Harju, "Accelerated molecular dynamics force evaluation on graphics processing units for thermal conductivity calculations," *Computer Physics Communications*, vol. 184, no. 5, pp. 1414 – 1425, 2013. [Online]. Available: http://www.sciencedirect.com/science/article/pii/S0010465513000258

[107] Z. Fan, W. Chen, V. Vierimaa, and A. Harju, "Efficient molecular dynamics simulations with many-body potentials on graphics processing units," *Computer Physics Communications*, vol. 218, pp. 10 – 16, 2017. [Online]. Available: http://www.sciencedirect.com/science/article/pii/S0010465517301339

[108] https://github.com/brucefan1983/GPUMD, 2017.

[109] S. Plimpton, "Fast parallel algorithms for short-range molecular dynamics," *Journal of Computational Physics*, vol. 117, no. 1, pp. 1 – 19, 1995. [Online]. Available: http://www.sciencedirect.com/science/article/pii/S002199918571039X

[110] J. Tersoff, "Modeling solid-state chemistry: Interatomic potentials for multicomponent systems," *Phys. Rev. B*, vol. 39, pp. 5566–5568, Mar 1989. [Online]. Available: https://link.aps.org/doi/10.1103/PhysRevB.39.5566

[111] M. J. Robertson, J. Tirado-Rives, and W. L. Jorgensen, "Improved Peptide and Protein Torsional Energetics with the OPLS-AA Force Field," *J. Chem. Theory Comput.*, vol. 11, no. 7, pp. 3499–3509, Jun. 2015. [Online]. Available: https://doi.org/10.1021/acs.jctc.5b00356

[112] https://github.com/brucefan1983/AGF-phonon-transport, 2019.

[113] A. Y. Serov, Z.-Y. Ong, and E. Pop, "Effect of grain boundaries on thermal transport in graphene," *Applied Physics Letters*, vol. 102, no. 3, p. 033104, 2013. [Online]. Available: http://dx.doi.org/10.1063/1.4776667

[114] J. Chen, G. Zhang, and B. Li, "Molecular dynamics simulations of heat conduction in nanostructures: Effect of heat bath," *Journal of the Physical Society of Japan*, vol. 79, no. 7, p. 074604, 2010. [Online]. Available: https://doi.org/10.1143/JPSJ.79.074604

[115] P. K. Schelling, S. R. Phillpot, and P. Keblinski, "Comparison of atomic-level simulation methods for computing thermal conductivity," *Phys. Rev. B*, vol. 65, p. 144306, Apr 2002. [Online]. Available: https://link.aps.org/doi/10.1103/PhysRevB.65.144306

[116] D. P. Sellan, E. S. Landry, J. E. Turney, A. J. H. McGaughey, and C. H. Amon, "Size effects in molecular dynamics thermal conductivity predictions," *Phys. Rev. B*, vol. 81, p. 214305, Jun 2010. [Online]. Available: https://link.aps.org/doi/10.1103/PhysRevB.81.214305

[117] T. Feng, X. Ruan, Z. Ye, and B. Cao, "Spectral phonon mean free path and thermal conductivity accumulation in defected graphene: The effects of defect type and concentration," *Phys. Rev. B*, vol. 91, p. 224301, Jun 2015. [Online]. Available: https://link.aps.org/doi/10.1103/PhysRevB.91.224301

[118] S. Zahiri, J. Zuo, Y. Shen, and H. Bao, "Numerical investigation of ballistic-diffusive heat transfer through a constriction with the boltzmann transport equation," *Applied Thermal Engineering*, vol. 141, pp. 126–133, 2018. [Online]. Available: http://www.sciencedirect.com/science/article/pii/S1359431117382200

[119] G. Chen, *Nanoscale energy transport and conversion: a parallel treatment of electrons, molecules, phonons, and photons.* Oxford University Press, 2005.

[120] X. Gu, Z. Fan, H. Bao, and C. Y. Zhao, "Revisiting phonon-phonon scattering in single-layer graphene," *Phys. Rev. B*, vol. 100, p. 064306, Aug 2019. [Online]. Available: https://link.aps.org/doi/10.1103/PhysRevB.100.064306

[121] J. Hu, X. Ruan, and Y. P. Chen, "Thermal Conductivity and Thermal Rectification in Graphene Nanoribbons: A Molecular Dynamics Study," *Nano Lett.*, vol. 9, no. 7, pp. 2730–2735, Jul. 2009. [Online]. Available: https://doi.org/10.1021/nl901231s

[122] N. Yang, G. Zhang, and B. Li, "Thermal rectification in asymmetric graphene ribbons," *Appl. Phys. Lett.*, vol. 95, no. 3, p. 033107, Jul. 2009. [Online]. Available: https://aip.scitation.org/doi/10.1063/1.3183587

[123] W.-r. Zhong, W.-h. Huang, X.-r. Deng, and B.-q. Ai, "Thermal rectification in thickness-asymmetric graphene nanoribbons," *Applied Physics Letters*, vol. 99, no. 19, p. 193104, 11 2011.

[124] H. Wang, S. Hu, K. Takahashi, X. Zhang, H. Takamatsu, and J. Chen, "Experimental study of thermal rectification in suspended monolayer graphene," *Nature Commun.*, vol. 8, pp. 1–8, Jun. 2017. [Online]. Available: https://www.nature.com/articles/ncomms15843

[125] M. López-Suárez, I. Neri, and R. Rurali, "Interface driven thermal rectification in a graphene–bilayer graphene junction from nonequilibrium molecular dynamics," *J Appl Phys*, vol. 124, no. 22, pp. 224 301–5, Dec. 2018. [Online]. Available: https://aip.scitation.org/doi/10.1063/1.5041085

[126] C. W. Chang, D. Okawa, A. Majumdar, and A. Zettl, "Solid-State Thermal Rectifier," *Science*, vol. 314, no. 5802, pp. 1121–1124, Nov. 2006. [Online]. Available: https://science.sciencemag.org/content/314/5802/1121

[127] P. K. Patra and B. Bhattacharya, "Nonergodicity of the Nose-Hoover chain thermostat in computationally achievable time," *Phys Rev E*, vol. 90, no. 4, pp. 043 304–7, Oct. 2014. [Online]. Available: https://link.aps.org/doi/10.1103/PhysRevE.90.043304

[128] C. D. Daub, P.-O. Åstrand, and F. Bresme, "Thermo-molecular orientation effects in fluids of dipolar dumbbells," *Phys. Chem. Chem. Phys.*, vol. 16, pp. 22 097–22 106, 2014. [Online]. Available: http://dx.doi.org/10.1039/C4CP03511A

[129] Y. Hu, X. Gu, T. Feng, Z. Fan, and H. Bao, "A unified phonon interpretation for the non-fourier heat conduction by non-equilibrium molecular dynamics simulations," *arXiv:1910.06668 [cond-mat.mes-hall]*, 2019. [Online]. Available: https://arxiv.org/abs/1910.06668

[130] M. Houssa, A. Dimoulas, and A. Molle, *2D Materials for Nanoelectronics*, T. . F. Group, Ed.   Boca Raton: CRC Press, 2016.

[131] M. J. Allen, V. C. Tung, and R. B. Kaner, "Honeycomb carbon : A review of graphene," *Chem. Rev.*, vol. 110, pp. 132–145, 2010.

[132] Y. Xu, Z. Li, and W. Duan, "Thermal and thermoelectric properties of graphene," *Small*, vol. 10, no. 11, pp. 2182–2199, 6 2014.

[133] N. M. R. Peres, "Colloquium : The transport properties of graphene: An introduction," *Reviews of Modern Physics*, vol. 82, no. 3, pp. 2673–2700, 9 2010.

[134] P. Y. Huang, C. S. Ruiz-Vargas, A. M. van der Zande, W. S. Whitney, M. P. Levendorf, J. W. Kevek, S. Garg, J. S. Alden, C. J. Hustedt, Y. Zhu, J. Park, P. L. McEuen, and D. A. Muller, "Grains and grain boundaries in single-layer graphene atomic patchwork quilts," *Nature*, vol. 469, no. 7330, pp. 389–392, 1 2011.

[135] A. W. Tsen, L. Brown, M. P. Levendorf, F. Ghahari, P. Y. Huang, R. W. Havener, C. S. Ruiz-Vargas, D. A. Muller, P. Kim, and J. Park, "Tailoring electrical transport across grain boundaries in polycrystalline graphene," *Science*, vol. 336, no. 6085, pp. 1143–1146, 6 2012.

[136] P. Yasaei, A. Fathizadeh, R. Hantehzadeh, A. K. Majee, A. El-Ghandour, D. Estrada, C. Foster, Z. Aksamija, F. Khalili-Araghi, and A. Salehi-Khojin, "Bimodal phonon scattering in graphene grain boundaries," *Nano Letters*, vol. 15, no. 7, pp. 4532–4540, 7 2015.

[137] Y. Wei, J. Wu, H. Yin, X. Shi, R. Yang, and M. Dresselhaus, "The nature of strength enhancement and weakening by pentagon–heptagon defects in graphene," *Nature Materials*, vol. 11, no. 9, pp. 759–763, 9 2012.

[138] Z. Fan, P. Hirvonen, L. F. C. Pereira, M. M. Ervasti, K. R. Elder, D. Donadio, A. Harju, and T. Ala-Nissila, "Bimodal grain-size scaling of thermal transport in polycrystalline graphene from large-scale molecular dynamics simulations," *Nano Letters*, vol. 17, no. 10, pp. 5919–5924, 2017, pMID: 28877440. [Online]. Available: http://dx.doi.org/10.1021/acs.nanolett.7b01742

[139] F. Giannazzo, I. Deretzis, A. La Magna, F. Roccaforte, and R. Yakimova, "Electronic transport at monolayer-bilayer junctions in epitaxial graphene on sic," *Physical Review B*, vol. 86, no. 23, p. 235422, 12 2012.

[140] X. Xu, N. M. Gabor, J. S. Alden, A. M. van der Zande, and P. L. McEuen, "Photo-thermoelectric effect at a graphene interface junction," *Nano Letters*, vol. 10, no. 2, pp. 562–566, 2 2010.

[141] X. Wang, W. Xie, J. Chen, and J.-b. Xu, "Homo- and hetero- p–n junctions formed on graphene steps," *ACS Applied Materials & Interfaces*, vol. 6, no. 1, pp. 3–8, 1 2014.

[142] A. Rajabpour, Z. Fan, and S. M. Vaez Allaei, "Inter-layer and intra-layer heat transfer in bilayer/monolayer graphene van der waals heterostructure: Is there a kapitza resistance analogous?" *Applied Physics Letters*, vol. 112, no. 23, p. 233104, 6 2018.

[143] T. Ma, Z. Liu, J. Wen, Y. Gao, X. Ren, H. Chen, C. Jin, X.-l. Ma, N. Xu, H.-m. Cheng, and W. Ren, "Tailoring the thermal and electrical transport properties of graphene films by grain size engineering," *Nature Communications*, vol. 8, p. 14486, 2 2017.

[144] S. Islam, Z. Li, V. E. Dorgan, M.-H. Bae, and E. Pop, "Role of joule heating on current saturation and transient behavior of graphene transistors," *IEEE Electron Device Letters*, vol. 34, no. 2, pp. 166–168, 2013.

[145] M.-h. Bae, Z. Li, Z. Aksamija, P. N. Martin, F. Xiong, Z.-y. Ong, I. Knezevic, and E. Pop, "Ballistic to diffusive crossover of heat flow in graphene ribbons," *Nature Communications*, vol. 4, no. 1, p. 1734, 12 2013.

[146] Z. Li, M.-H. Bae, and E. Pop, "Substrate-supported thermometry platform for nanomaterials like graphene, nanotubes, and nanowires," *Applied Physics Letters*, vol. 105, no. 2, p. 023107, 7 2014.

[147] G. Bussi, D. Donadio, and M. Parrinello, "Canonical sampling through velocity rescaling," *The Journal of Chemical Physics*, vol. 126, no. 1, p. 014101, 1 2007.

[148] I. Duchemin and D. Donadio, "Atomistic simulations of heat transport in real-scale silicon nanowire devices," *Applied Physics Letters*, vol. 100, no. 22, p. 223107, 5 2012.

[149] B. W. H. van Beest, G. J. Kramer, and R. A. van Santen, "Force fields for silicas and aluminophosphates based on ab initio calculations," *Physical Review Letters*, vol. 64, no. 16, pp. 1955–1958, 4 1990.

[150] W. Jang, Z. Chen, W. Bao, C. N. Lau, and C. Dames, "Thickness-dependent thermal conductivity of encased graphene and ultrathin graphite," *Nano Letters*, vol. 10, no. 10, pp. 3909–3913, 10 2010.

[151] M. Asheghi, K. Kurabayashi, R. Kasnavi, and K. E. Goodson, "Thermal conduction in doped single-crystal silicon films," *Journal of Applied Physics*, vol. 91, no. 8, pp. 5079–5088, 4 2002.

[152] Z. Chen, W. Jang, W. Bao, C. N. Lau, and C. Dames, "Thermal contact resistance between graphene and silicon dioxide," *Applied Physics Letters*, vol. 95, no. 16, p. 161910, 10 2009.

[153] Y. K. Koh, M.-H. Bae, D. G. Cahill, and E. Pop, "Heat conduction across monolayer and few-layer graphenes," *Nano Letters*, vol. 10, no. 11, pp. 4363–4368, 11 2010.

[154] D. G. Cahill, "Thermal conductivity measurement from 30 to 750 k: the 3 method," *Review of Scientific Instruments*, vol. 61, no. 2, pp. 802–808, 2 1990.

[155] T. Yamane, N. Nagai, S.-i. Katayama, and M. Todoki, "Measurement of thermal conductivity of silicon dioxide thin films using a 3 method," *Journal of Applied Physics*, vol. 91, no. 12, p. 9772, 2002.

[156] J. H. Seol, I. Jo, A. L. Moore, L. Lindsay, Z. H. Aitken, M. T. Pettes, X. Li, Z. Yao, R. Huang, D. Broido, N. Mingo, R. S. Ruoff, and L. Shi, "Two-dimensional phonon transport in supported graphene," *Science*, vol. 328, no. 5975, pp. 213–216, 4 2010.

[157] M. M. Sadeghi, I. Jo, and L. Shi, "Phonon-interface scattering in multilayer graphene on an amorphous support," *Proceedings of the National Academy of Sciences*, vol. 110, no. 41, pp. 16 321–16 326, 10 2013.

[158] K. Saito, J. Nakamura, and A. Natori, "Ballistic thermal conductance of a graphene sheet," *Physical Review B*, vol. 76, no. 11, p. 115409, 9 2007.

[159] Z.-Y. Ong, B. Qiu, S. Xu, X. Ruan, and E. Pop, "Flexural resonance mechanism of thermal transport across graphene-sio2 interfaces," *Journal of Applied Physics*, vol. 123, no. 11, p. 115107, 2018. [Online]. Available: https://doi.org/10.1063/1.5020705

[160] J. Cho, M. D. Losego, H. G. Zhang, H. Kim, J. Zuo, I. Petrov, D. G. Cahill, and V. P. Braun, "Electrochemically tunable thermal conductivity of lithium cobalt oxide." *Nature Communications*, vol. 5, p. 4035, 2014.

[161] D. Li, Y. Wu, P. Kim, L. Shi, P. Yang, and A. Majumdar, "Thermal conductivity of individual silicon nanowires," *Applied Physics Letters*, vol. 83, no. 14, pp. 2934–2936, 2003.

[162] A. K. Geim and V. I. Grigorieva, "Van der waals heterostructures," *Nature*, vol. 499, pp. 419–425, 2013.

[163] R. Guo, Y. D. Jho, and A. J. Minnich, "Coherent control of thermal phonon transport in van der waals superlattices," *Nanoscale*, vol. 10, pp. 14 432–14 440, 2018.

[164] S. Hu, S. Ju, C. Shao, J. Guo, B. Xu, M. Ohnishi, and J. Shiomi, "Ultimate impedance of coherent heat conduction in van der waals graphene-mos2 heterostructures," *Materials Today Physics*, vol. 16, p. 100324, 2020.

[165] H. Sadeghi, S. Sangtarash, and C. J. Lambert, "Cross-plane enhanced thermoelectricity and phonon suppression in graphene/mos2 van der waals heterostructures," *2D Materials*, vol. 4, p. 015012, 2017.

[166] V. S. Suryavanshi, A. J. Gabourie, A. Barati Farimani, and E. Pop, "Thermal boundary conductance of two-dimensional mos$_2$ interfaces," *Journal of Applied Physics*, vol. 126, no. 5, p. 055107, 2019.

[167] Y. Zhao, Y. Cai, L. Zhang, B. Li, G. Zhang, and J. T. L. Thong, "Thermal transport in 2d semiconductors — considerations for device applications," *Advanced Functional Materials*, vol. 30, p. 1903929, 2020.

[168] E. Yalon, C. J. Mcclellan, K. K. H. Smithe, R. L. Xu, M. M. Rojo, V. S. Suryavanshi, A. J. Gabourie, C. M. Neumann, F. Xiong, and E. Pop, "Energy dissipation in monolayer mos2 electronics," *Nano Letters*, vol. 17, no. 6, pp. 3429–3433, 2017.

[169] S. Vaziri, E. Yalon, M. M. Rojo, V. S. Suryavanshi, H. Zhang, C. J. Mcclellan, C. S. Bailey, K. K. H. Smithe, A. J. Gabourie, V. Chen, S. Deshmukh, L. Bendersky, V. A. Davydov, and E. Pop, "Ultrahigh thermal isolation across heterogeneously layered two-dimensional materials," *Science Advances*, vol. 5, p. eaax1325, 2019.

[170] Y. Liu, Z.-y. Ong, J. Wu, Y. Zhao, K. Watanabe, T. Taniguchi, D. Chi, G. Zhang, J. T. Thong, C.-W. Qiu, and K. Hippalgaonkar, "Thermal conductance of the 2d mos2/h-bn and graphene/h-bn interfaces," *Scientific reports*, vol. 7, p. 43886, 2017.

[171] D. B. Brown, W. Shen, X. Li, K. Xiao, D. B. Geohegan, and S. Kumar, "Spatial mapping of thermal boundary conductance at metal-molybdenum diselenide interfaces," *ACS Applied Materials and Interfaces*, vol. 11, no. 15, pp. 14 418–14 426, 2019.

[172] P. Yasaei, C. J. Foss, K. Karis, A. Behranginia, A. I. El-Ghandour, A. Fathizadeh, J. Olivares, A. K. Majee, C. D. Foster, F. Khalili-Araghi, Z. Aksamija, and A. Salehi-Khojin, "Interfacial thermal transport in monolayer mos2- and graphene-based devices," *Advanced Materials Interfaces*, vol. 4, p. 1700334, 2017.

[173] P. E. Hopkins, M. Baraket, V. E. Barnat, T. E. Beechem, S. P. Kearney, J. C. Duda, J. T. Robinson, and S. G. Walton, "Manipulating thermal conductance at metal-graphene contacts via chemical functionalization," *Nano Letters*, vol. 12, no. 2, pp. 590–595, 2012.

[174] C. Nyby, A. Sood, P. Zalden, A. J. Gabourie, P. Muscher, D. Rhodes, E. Mannebach, J. Corbett, A. Mehta, E. Pop, T. F. Heinz, and A. M. Lindenberg, "Visualizing energy transfer at buried interfaces in layered materials using picosecond x-rays," *Advanced Functional Materials*, vol. 30, p. 2002282, 2020.

[175] A. Sood, R. Cheaito, T. Bai, H. Kwon, Y. Wang, C. Li, L. Yates, T. Bougher, S. Graham, M. Asheghi, M. Goorsky, and K. E. Goodson, "Direct visualization of thermal conductivity suppression due to enhanced phonon scattering near individual grain boundaries," *Nano Letters*, vol. 18, no. 6, pp. 3466–3472, 2018.

[176] A. Gurarslan, Y. Yu, L. Su, Y. Yu, F. Suarez, S. Yao, Y. Zhu, M. Ozturk, Y. Zhang, and L. Cao, "Surface-energy-assisted perfect transfer of centimeter-scale monolayer and few-layer mos2 films onto arbitrary substrates," *ACS Nano*, vol. 8, no. 11, pp. 11 522–11 528, 2014.

[177] D. H. Olson, V. A. Avincola, C. G. Parker, J. L. Braun, J. T. Gaskins, J. A. Tomko, E. J. Opila, and P. E. Hopkins, "Anisotropic thermal conductivity tensor of -y2si2o7 for orientational control of heat flow on micrometer scales," *Acta Materialia*, vol. 189, pp. 299–305, 2020. [Online]. Available: https://www.sciencedirect.com/science/article/pii/S1359645420301531

[178] S. Huxtable, D. G. Cahill, V. Fauconnier, J. O. White, and J. C. Zhao, "Thermal conductivity imaging at micrometre-scale resolution for combinatorial studies of materials," *Nature Materials*, vol. 3, pp. 298–301, 2004.

[179] J. Yang, E. Ziade, C. Maragliano, R. Crowder, X. Wang, M. Stefancich, M. Chiesa, A. K. Swan, and A. J. Schmidt, "Thermal conductance imaging of graphene contacts," *Journal of Applied Physics*, vol. 116, p. 023515, 2014.

[180] J.-W. Jiang and H. S. Park, "Mechanical properties of mos2/graphene heterostructures," *Applied Physics Letters*, vol. 105, p. 033108, 2014.

[181] T. Liang, S. R. Phillpot, and S. B. Sinnott, "Parametrization of a reactive many-body potential for mo – s systems," *Physical Review B*, vol. 79, p. 245110, 2009.

[182] V. V. Reshetniak and V. A. Aborkin, "Aluminum–carbon interaction at the aluminum–graphene and aluminum–graphite interfaces," *Journal of Experimental and Theoretical Physics*, vol. 130, no. 2, pp. 214–227, 2020.

[183] Y. Mishin, D. Farkas, M. J. Mehl, and D. A. Papaconstantopoulos, "Interatomic potentials for monoatomic metals from experimental data and ab initio calculations," *Physical Review B*, vol. 59, no. 5, pp. 3393–3407, 1999.

[184] A. Ebnonnasir, B. Narayanan, S. Kodambaka, and C. Ciobanu, "Tunable mos2 bandgap in mos2-graphene heterostructures," *Applied Physics Letters*, vol. 105, p. 031603, 2014.

[185] G. Leibfried and W. Ludwig, "Theory of anharmonic effects in crystals," New York, pp. 276–444, 1961.

[186] P. Nath, J. J. Plata, D. Usanmaz, R. Al Rahal Al Orabi, M. Fornari, M. B. Nardelli, C. Toher, and S. Curtarolo, "High-throughput prediction of finite-temperature properties using the quasi-harmonic approximation," *Computational Materials Science*, vol. 125, pp. 82–91, 2016.

[187] Y. Baskin and L. Meyer, "Lattice constants of graphite at low temperatures," *Physical Review*, vol. 100, no. 2, p. 544, 1955.

[188] K. K. Smithe, C. D. English, V. S. Suryavanshi, and E. Pop, "Intrinsic electrical transport and performance projections of synthetic monolayer mos2 devices," *2D Materials*, vol. 4, p. 011009, 2017.

[189] N. C. Wang, E. A. Carrion, M. C. Tung, and E. Pop, "Reducing graphene device variability with yttrium sacrificial layers," *Applied Physics Letters*, vol. 110, p. 223106, 2017.

[190] K. Liu, L. Zhang, T. Cao, C. Jin, D. Qiu, Q. Zhou, A. Zettl, P. Yang, S. G. Louie, and F. Wang, "Evolution of interlayer coupling in twisted molybdenum disulfide bilayers," *Nature Communications*, vol. 5, p. 4966, 2014.

[191] Z. Hemmat, P. Yasaei, J. F. Schultz, L. Hong, L. Majidi, A. Behranginia, L. Verger, N. Jiang, M. W. Barsoum, R. F. Klie, and A. Salehi-Khojin, "Tuning thermal transport through atomically thin ti3c2tz mxene by current annealing in vacuum," *Advanced Functional Materials*, vol. 29, p. 1805693, 2019.

[192] K. Jin, D. Liu, and Y. Tian, "Enhancing the interlayer adhesive force in twisted multilayer mos2 by thermal annealing treatment," *Nanotechnology*, vol. 26, no. 40, p. 405708, 2015.

[193] A. Das, B. Chakraborty, S. Piscanec, S. Pisana, A. K. Sood, and A. C. Ferrari, "Phonon renormalization in doped bilayer graphene," *Physical Review B*, vol. 79, p. 155417, 2009.

[194] Z. Li, Y. Liu, L. Lindsay, Y. Xu, W. Duan, and E. Pop, "Size dependence and ballistic limits of thermal transport in anisotropic layered two-dimensional materials," *arXiv:1711.02772*, 2017.

[195] Z. Ding, Q. X. Pei, J. W. Jiang, W. Huang, and Y. W. Zhang, "Interfacial thermal conductance in graphene/mos2 heterostructures," *Carbon*, vol. 96, pp. 888–896, 2016.

[196] J. Zhang, Y. Hong, and Y. Yue, "Thermal transport across graphene and single layer hexagonal boron nitride," *Journal of Applied Physics*, vol. 117, no. 13, p. 134307, 2015.

[197] B. Li, L. Wang, and G. Casati, "Thermal diode: Rectification of heat flux," *Physical Review Letters*, vol. 93, no. 18, p. 184301, 2004.

[198] C. Chiritescu, D. G. Cahill, N. Nguyen, D. Johnson, A. Bodapati, P. Keblinski, and P. Zschack, "Ultralow thermal conductivity in disordered, layered wse$_2$ crystals," *Science*, vol. 315, no. 5810, pp. 351–353, 2007.

[199] K. Kadoya, N. Matsunaga, and A. Nagashima, "Viscosity and thermal conductivity of dry air in the gaseous phase," *Journal of Physical and Chemical Reference Data*, vol. 14, no. 4, pp. 947–970, 1985.

[200] Z. Ding, J.-W. Jiang, Q.-X. Pei, and Y.-W. Zhang, "In-plane and cross-plane thermal conductivities of molybdenum disulfide," *Nanotechnology*, vol. 26, no. 6, p. 65703, 2015.

[201] S. Chen, A. Sood, E. Pop, K. E. Goodson, and D. Donadio, "Strongly tunable anisotropic thermal transport in mos2 by strain and lithium intercalation: first-principles calculations," *2D Materials*, vol. 6, no. 2, p. 025033, 3 2019.